
ADAPTIVE NEURO-FUZZY INFERENCE SYSTEM MODELLING
OF SURFACE TOPOLOGY IN ULTRA-HIGH PRECISION
DIAMOND TURNING OF RAPIDLY SOLIDIFIED ALUMINIUM
GRADE (RSA 443)

By

ZVIKOMBORERO HWEJU
(Student Number: S219146578)

APRIL 2020

**ADAPTIVE NEURO-FUZZY INFERENCE SYSTEM MODELLING
OF SURFACE TOPOLOGY IN ULTRA-HIGH PRECISION
DIAMOND TURNING OF RAPIDLY SOLIDIFIED ALUMINIUM
GRADE (RSA 443)**

HWEJU ZVIKOMBORERO

SUPERVISOR: PROF. KHALED ABOU EL-HOSSEIN

Submitted in fulfilment of the requirements for the Degree: Master of
Engineering (Mechatronics)

**NELSON MANDELA UNIVERSITY
DEPARTMENT OF MECHATRONICS ENGINEERING
FACULTY OF ENGINEERING AND THE BUILT ENVIRONMENT**

APRIL 2020

COPYRIGHT STATEMENT

This thesis copy has been furnished on the condition that anyone who refers to it understands that copyright rests with Nelson Mandela University. No part of it, either in hard or soft copy form should be published without the author's prior approval unless acknowledged and properly cited.

DECLARATION

I, **Hweju Zvikomborero**, in accordance with Rule G5.6.3, hereby declare that this thesis, is my own work and that it has not previously been submitted for assessment to another University or for another qualification. Acknowledgement has been made in cases where the presented content has been taken from other sources. Care has been taken to ensure originality of work, and, to the best knowledge of the author, does not breach any copyright law.



Author's Signature

Date: 22 July 2019

DEDICATION

To my beloved wife and children.

ACKNOWLEDGEMENTS

First and foremost, my sincere appreciation goes to the almighty God, whose providence has made this research journey a success. He has sufficiently provided the financial, physical and spiritual resources that were needed to complete this research. Through the most difficult times, he has given me the comfort and strength; and I never lacked anything.

I sincerely appreciate the valuable assistance offered by my supervisor Prof. Khaled Abou-El-Hossein during the entire course of the project. His constructive criticism has kept me out of the comfort zone and made sure that my research work is as original as it could be. Because of him, I experienced true research and am no longer the same. Thank you so much Prof.

Utmost thanks go to my wife (Mrs.) Tsitsi Laiza Hweju who was always a source of inspiration and moral support during the challenging journey. She has sacrificed numerous luxuries just to make sure that I achieve this feat. Words fail me in expressing how I feel about your support my wife. I also from the depth of my heart appreciate my children; Nokutenda and Tinotenda, who even at such tender ages have had to endure so much stress and discomfort just for me. God bless you.

Lastly, I cannot forget my fellow study group mates, Mr. Odedeyi Peter Babatunde, Mr. Oyekunle Funsho Adekunle, Mr. Victor Ejiofor, Gregoire Tambwe Mbangu and Mr. Liman Muhammad; who in times of challenges gave me the assurance that I was not alone, and it was achievable. Thank you so much for your moral support gentlemen. Without you by my side, my stay at Nelson Mandela University would have been unbearable. You exhibited the true sense of 'esprit de corps'. I wish you all the best in your respective endeavors.

LIST OF PUBLICATIONS FROM THIS WORK:

Accepted and Presented Conference Papers:

Zvikomborero Hweju and Khaled Abou-El-Hossein, “*Effect of coolant Type on Surface Roughness and RSM Modelling in Single Point Diamond Turning of RSA443 Optical Aluminium*”, 10th International Conference on Manufacturing Science and Technology (ICMST), Sabah, Malaysia, 9th-11th August 2019.

Zvikomborero Hweju and Khaled Abou-El-Hossein, “*Surface Roughness Prediction Based on Acoustic Emission Signals in High-Precision Diamond Turning of Rapidly Solidified Optical Aluminum Grade (RSA443)*”, 4th International Conference on Material Engineering and Application (ICMEA), Kuala Lumpur, Malaysia, 23rd-25th August 2019.

Zvikomborero Hweju and Khaled Abou-El-Hossein, “*Efficiency Assessment of ANFIS in Surface Topology Prediction of RSA 443 Optical Aluminium Using Small Datasets*”, 3rd International Conference on Intelligent Manufacturing and Automation Engineering (ICIMA), Tokyo, Japan, 27th-30th September 2019.

ABSTRACT

*ADAPTIVE NEURO-FUZZY INFERENCE SYSTEM MODELLING OF SURFACE TOPOLOGY
IN ULTRA-HIGH PRECISION DIAMOND TURNING OF RAPIDLY SOLIDIFIED
ALUMINIUM GRADE (RSA 443)*

Hweju Z.

M.Eng., Mechatronics Engineering

Supervisor: Prof Khaled Abou-El-Hossein

Faculty of Engineering, the Built Environment and Information Technology

P.O. Box 77000, Nelson Mandela University,

Port Elizabeth, South Africa

August 2019

Surface roughness prediction is a crucial stage during product manufacturing since it acts as a quality indicator. This investigative research thesis presents an online surface roughness prediction, based on the Adaptive Neuro-Fuzzy Inference System (ANFIS) model during Ultra-High Precision Diamond Turning (UHPDT) of Rapidly Solidified Aluminium (RSA-443) using water and kerosene as coolants. Based on the Taguchi L9 orthogonal array, the cutting parameters (spindle speed, depth of cut and feed rate) are varied at three levels. Acoustic Emission (AE) signals are detected during the UHPDT process using a piezoelectric sensor. Spindle speed, depth of cut, feed rate, AE root mean square, prominent frequency and peak rate are considered as model inputs in this thesis. The experimental results reveal that a better surface finish is obtained using water coolant in comparison to kerosene coolant. Mean Absolute Percentage Error (MAPE) based comparison between ANFIS and Response Surface Method (RSM) is carried out. In this study, the ANFIS model has a prediction accuracy of 79.42% and 69.40% on water-based and kerosene-based results respectively. The RSM model yields higher prediction accuracies of 98.59% and 95.55% on water-based and kerosene-based results respectively.

Keywords: Adaptive Neuro-Fuzzy Inference System, Ultra-High Precision Diamond Turning, Surface Roughness, Acoustic Emission Signal, Mean Absolute Percentage Error, RSA-443.

LIST OF ABBREVIATIONS

AE	Acoustic Emission
AES	Acoustic Emission Sensing
AI	Artificial Intelligence
ANFIS	Adaptive Neuro-Fuzzy Inference System
ANN	Artificial Neural Network
ANOVA	Analysis of Variance
CNC	Computer Numerical Control
CVD	Chemical Vapor Deposited
DFT	Discrete Fourier Transform
DOE	Design of Experiment
DWT	Discrete Wavelet Transform
FFT	Fast Fourier Transform
FIS	Fuzzy Inference System
GA	Genetic Algorithm
GDM	Gradient Descent Method
HSS	High Speed Steel
LSM	Least Squares Method
MAPE	Mean Absolute Percentage Error
MARSE	Measured Area Under Rectified Signal Envelop
MF	Membership Function
NDT	Non-Destructive Testing
PCD	Polycrystalline Diamond
PCBN	Polycrystalline Cubic Boron Nitride
RMS	Root Mean Square
RSA	Rapidly Solidified Aluminium
RSM	Response Surface Methodology

SCD	Single Crystal Diamond
SPDT	Single Point Diamond Turning
STFT	Short Time Fourier Transform
UHPDT	Ultra-High Precision Diamond Turning

NOMENCLATURE

R_a	Surface Roughness
C	Spindle Speed
F	Feed
D	Depth of Cut
A_e	Acoustic emission signal root mean square
P_f	Peak Frequency
R^2	Coefficient of determination
Z	Normalized value

TABLE OF CONTENTS

COPYRIGHT STATEMENT	iii
DECLARATION	iv
DEDICATION	v
ACKNOWLEDGEMENTS	vi
LIST OF PUBLICATIONS FROM THIS WORK:.....	vii
ABSTRACT.....	viii
LIST OF ABBREVIATIONS.....	ix
NOMENCLATURE	xi
TABLE OF CONTENTS.....	xii
LIST OF FIGURES	xvi
LIST OF TABLES.....	xix
CHAPTER ONE	1
1.0 INTRODUCTION	1
1.1 Background.....	1
1.2 Problem Statement.....	2
1.3 Hypothesis.....	3
1.4 Aim	3
1.5 Objectives	3
1.6 Project Scopes.....	4
1.7 Motivation.....	4
1.8 Chapter Layout.....	5
CHAPTER TWO	7
2.0 LITERATURE SURVEY.....	7
2.1 Introduction.....	7
2.2 Determinants of RSA Alloy Properties.....	7
2.2.1 Improved Microstructure Homogeneity Effects on RSA Properties	8
2.2.2 Small Grain Size Effects on RSA Properties	9
2.2.3 Alloying Percentage Effects on RSA Properties.....	10
2.3 Production Methods of Rapidly Solidified Aluminium Alloys	11
2.3.1 Spray Forming Method.....	11
2.3.2 Laser Surface Melting Methods.....	12
2.3.3 Chill Methods.....	14

2.4 Surface Roughness in Ultra-High Precision Diamond Turning.....	15
2.4.1 Surface Roughness Parameters	15
2.4.2 Effect of Material Characteristics on Surface Roughness.....	17
2.4.3 Temperature Effect on Surface Roughness.....	17
2.4.4 Tool Vibration Effect on Surface Roughness	19
2.4.5 Cutting Parameter Effects on Surface Roughness	19
2.4.6 Tool Geometry Effect on Surface Roughness.....	20
2.4.7 Surface Roughness Effects on Fatigue Life	21
2.5 Cutting Tool Materials.....	22
2.5.1 Single Point Diamond	22
2.5.2 Carbon and Medium Alloy Steels.....	24
2.5.3 High Speed Steels	25
2.5.4 Carbides	26
2.5.5 Polycrystalline Diamond.....	27
2.6 Review of Acoustic Emission and Signal Processing.....	27
2.6.1 Acoustic Emission Sensors	27
2.6.2 Acoustic Emission Sensor Piezoelectricity.....	28
2.6.3 Piezoelectric Material Size Effects	29
2.6.4 Piezoelectric Sensor Couplants.....	30
2.6.5 Piezotron Coupler	31
2.6.6 Temperature Dependency of Piezoelectricity	32
2.6.7 Sensor Sensitivity.....	33
2.6.7.1 Effect of Cables.....	33
2.6.7.2 Effect of Preamplifier Noise	34
2.6.8 Sensor Calibration.....	35
2.6.9 Acoustic Emission Signal Parameters.....	36
2.6.10 Acoustic Emission Wave Propagation Effects.....	37
2.6.11 A comparison of the AE technique and other NDT Methods	38
2.6.12 Acoustic Emission Signal Correction and Pre-processing	39
2.7 Computational/Artificial Intelligence	41
2.7.1 Previous Applications of ANFIS and ANN in Surface Roughness Prediction.....	42
2.7.2 Fuzzy Modeling & Fuzzy Inference System.....	43
2.7.2.1 Boolean Logic vs Fuzzy Logic	43

2.7.2.2 Fuzzy Set Theory	44
2.7.2.3 Fuzzy Inference Systems	45
2.7.2.4 Fuzzification	46
2.7.2.5 Rule Evaluation.....	47
2.7.2.6 Defuzzification.....	48
2.7.2.7 Mamdani-Type FIS VS. Sugeno-Type FIS.....	49
2.7.3 Artificial Neural Networks.....	50
2.7.3.2 Learning in Artificial Neural Networks	56
2.7.3.3 Artificial Neural Networks Learning Rules	57
2.7.4 Adaptive Neuro-Fuzzy Inference Systems.....	60
2.7.4.1 Overview of Adaptive Neuro-Fuzzy Inference System	60
2.7.4.2 ANFIS Architecture	60
2.7.4.3 ANFIS Learning Algorithm	63
2.7.4 Regression Model	64
2.8 Conclusion	65
CHAPTER THREE	66
3.0 MATERIALS AND METHODOLOGY	66
3.1 Introduction.....	66
3.2 Workpiece Material Selection.....	66
3.3 Design of Experiment	68
3.3.1 Selection of Process Variables and Limits.....	68
3.3.2 Selection of Orthogonal Arrays (Taguchi Design)	69
3.3.3 Assigning the independent variables to each column	70
3.3.4 Tool Centering and Spindle Balancing	71
3.3.4 Ultra-High Precision Diamond Turning Setup	73
3.3.4.1 Experimental Procedure	75
3.3.5 Surface Roughness Measurement Setup	76
3.3.6 Acoustic Emission Signal Acquisition Experiment Process Flow.....	77
3.3.7 Acoustic Emission Signal Feature Extraction.....	79
3.3.5.1 Acoustic Emission Peak Rate Determination	79
3.3.5.2 Acoustic Emission Root Mean Square Determination.....	80
3.3.5.3 Peak Frequency Determination.....	80
3.3.6 Adaptive Neuro-Fuzzy Inference System Modelling	81

3.4 Conclusion	83
CHAPTER FOUR.....	84
4.0 RESULTS AND DISCUSSION	84
4.1 Introduction.....	84
4.2 Surface Roughness Experimental Results.....	84
4.3 Determination of Acoustic Emission Signal Parameters	89
4.4 Regression Model Prediction of Surface Roughness	93
4.4.1 Water-Based Results Surface Roughness Prediction using Regression Model	94
4.4.1.1 Validation of Surface Roughness Prediction Model for Water Coolant Based Results	96
4.4.2 Surface Roughness Prediction Regression Model for Kerosene Coolant Based Results.....	96
4.4.2.1 Validation of Surface Roughness Prediction Model for Kerosene Coolant Based Results	99
4.5 ANFIS Prediction of Surface Roughness.....	100
4.5.1 ANFIS Modelling of Water Coolant Based Results	101
4.5.2 ANFIS Modelling of Kerosene Coolant Based Results	112
4.6 Comparison of Regression and ANFIS Models for Water and Kerosene Surface Roughness Results	122
4.7 Impact of Acoustic Emission Signal Parameters on Prediction Accuracy.....	123
4.8 Summary of results	124
CHAPTER FIVE	126
5.0 CONCLUSION AND RECOMMENDATIONS.....	126
5.1 Introduction.....	126
5.2 Conclusions.....	126
5.3 Recommendations.....	127
APPENDIX A: KISTLER 8152B DATA.....	135
APPENDIX B: ASM HANDBOOK, VOLUME 16: MACHINING, p761-804.....	136
APPENDIX C: PEAK RATE ALGORITHM	137
APPENDIX D: INPUTS MEMBERSHIP FUNCTIONS.....	138
APPENDIX E: TURNITIN EPHORUS RESULTS FOR THESIS	141

LIST OF FIGURES

Figure 1. 1: Chapter Layout	6
Figure 2. 1: Effects of Rapid Solidification on Microstructure [8].....	8
Figure 2. 2: Spray Forming process schematic [23]	12
Figure 2. 3: Principle of rapid solidification at the surface showing rapid local melting with a traversing heat source [25].....	13
Figure 2. 4: Temperature variation along the beam path [26]	14
Figure 2. 5: The melt spinning process [29]	15
Figure 2. 6: Roughness Average Perimeter and Peak Surface Roughness Spacing [30]	16
Figure 2. 7: Heat generation zones [44].....	18
Figure 2. 8: Tool Geometry of Single Point Cutting Tool [60]	21
Figure 2. 9: Surface Roughness versus Fatigue Limit [64]	22
Figure 2. 10: Geometry of a typical single point diamond cutting tool [65]	23
Figure 2. 11: Typical Acoustic Emission Sensor [81]	29
Figure 2. 12: Kistler Piezotron Coupler [88]	32
Figure 2. 13: AE Signal Features [97]	36
Figure 2. 14: Artificial Intelligence Disciplines [104].....	41
Figure 2. 15: Differences between Boolean Logic and Fuzzy Logic [104].....	44
Figure 2. 16: (a) Crisp Set and (b) Fuzzy Set [114].....	45
Figure 2. 17: Fuzzy Inferencing Unit [116].....	46
Figure 2. 18: Membership function shapes [119].....	47
Figure 2. 19: Biological Neuron Structure [127].....	51
Figure 2. 20: Mathematical Model of a Neuron [127].....	52
Figure 2. 21: Feed-forward Artificial Neural Network [130].....	53
Figure 2. 22: Feedback Artificial Neural Network Architecture [131]	55
Figure 2. 23: Mapping Block Diagram [130]	55
Figure 2. 24: Excitation effect of first node [132]	58
Figure 2. 25: First order Sugeno model [137].....	61
Figure 2. 26: ANFIS Architecture [137].....	61

Figure 3. 1: RSA 443 Workpiece Mounted on Aluminum Adapter Disk	67
Figure 3. 2: Design of Experiment Steps	68
Figure 3. 3: Diamond Cutting Tool Centering.....	72
Figure 3. 4: Spindle balancing platform DIFFSYS	73
Figure 3. 5: Ultra-High Precision Diamond Turning Setup.....	74
Figure 3. 6: LabVIEW Software (front panel) showing AE signal during RSA 443 Machining. 75	
Figure 3. 7: Taylor Hobson Profilometer.....	76
Figure 3. 8: Acoustic Emission Signal Acquisition Experiment Process Flow	77
Figure 3. 9: Acoustic Emission Peak Rate Determination Flow Chart.....	79
Figure 3. 10: Peak Frequency Determination Flow Chart	80
Figure 3. 11: ANFIS Model Process Flow.....	81
Figure 3. 12: ANFIS Editor Display	83
Figure 4. 1: Series Plots of Experimental Surface Roughness.....	86
Figure 4. 2: a) Surface Profile Chart for Worst Water Ra value (29 nm) and b) Surface Profile Chart for Worst Kerosene Ra value (38 nm)	88
Figure 4. 3: a) Surface Profile Chart for Best Water R _a value (11 nm) and b) Surface Profile Chart for Best Kerosene R _a value (12 nm)	89
Figure 4. 4: a) Time domain signal for R _a =38nm (kerosene) and b) Frequency domain signal for R _a = 38nm (kerosene)	90
Figure 4. 5: a) Time domain signal for R _a =12nm (kerosene) and b) Frequency domain signal for R _a = 12nm (kerosene)	91
Figure 4. 6: Series Plots of Absolute Error Values	99
Figure 4. 7: ANFIS Model Training Data Loading Stage	103
Figure 4. 8: Fuzzy Inference System (FIS) Generating Stage	104
Figure 4. 9: Fuzzy Inference System Training Stage.....	105
Figure 4. 10: Training Set Stage Results (Water Coolant)	106
Figure 4. 11: Testing Set Sample Results (Water Coolant).....	107
Figure 4. 12: ANFIS Surface Viewer	108
Figure 4. 13: ANFIS Rule Viewer	109

Figure 4. 14: ANFIS Model Data Loading Stage 114

Figure 4. 15: FIS Generation Stage..... 115

Figure 4. 16: ANFIS Training Stage..... 116

Figure 4. 17: Training Set Stage Results (Kerosene Coolant) 117

Figure 4. 18: Testing Set Stage Results (Water Coolant) 118

Figure 4. 19: ANFIS Rule Viewer 119

Figure 4. 20: ANFIS Surface Viewer 120

Figure 4. 21: Comparison of Regression and ANFIS Models in Predicting Surface Roughness
(Water Coolant) 122

LIST OF TABLES

Table 2. 1: Effects of Increasing Silicon in Al-Si Alloys [8].....	10
Table 2. 2: SPDT and carbide comparison data [69]	24
Table 2. 3: Carbon Steel Categories [71].....	25
Table 2. 4: High Speed Steel Chemical Composition [73].....	26
Table 2. 5: Carbide Grades and Applications	27
Table 2. 6: Acoustic Emission Couplants [85]	30
Table 2. 7: Comparison of AE characteristics with other NDT methods [101]	39
Table 2. 8: Differences in approach between conventional computing and Soft Computing [104]	42
Table 2. 9: The two passes in the hybrid learning algorithm [119]	64
Table 3. 1: Mechanical Properties of RSA 443 Alloy [140]	67
Table 3. 2: Process Parameters with associated levels	69
Table 3. 3: Levels of process parameters used in Taguchi (L9) Orthogonal Array.....	70
Table 3. 4: Experimental design using L9 Taguchi orthogonal array.....	71
Table 3. 5: RSA 443 Cutting conditions.....	74
Table 3. 6: Taylor Hobson Profilometer Description	77
Table 3. 7: Acoustic Emission Signal Circuit Components Specifications.....	78
Table 4. 1: Surface Roughness Experimental Results	85
Table 4. 2: Percentage Difference Between Water and Kerosene Surface Roughness Values	87
Table 4. 3: Acoustic Emission Signal Analysis Results (Kerosene Coolant).....	92
Table 4. 4: Acoustic Emission Signal Analysis Results (Water Coolant)	93
Table 4. 5: Regression Model Computation Results	94
Table 4. 6: Regression Model Prediction Results.....	95
Table 4. 7: Validation Results for Water Coolant-based Model.....	96
Table 4. 8: Regression Model Computation Results	97
Table 4. 9: Regression Model Prediction Results.....	98
Table 4. 10: Validation Results for Kerosene Coolant-based Model	100
Table 4. 11: Extra Data Sets for ANFIS Training (Water Coolant Based Results).....	101
Table 4. 12: Normalized ANFIS Data (Water Coolant Based Results).....	102
Table 4. 13: ANFIS Learning Information	110
Table 4. 14: Comparison of ANFIS results with experimental findings (Water Coolant)	111
Table 4. 15: Extra Data Sets for ANFIS Training (Kerosene Coolant Based Results)	112
Table 4. 16: Normalized Data (Kerosene Coolant Based Results).....	113
Table 4. 17: Comparison of ANFIS results with experimental findings (Kerosene Coolant)....	121
Table 4. 18: Surface Roughness Values Based on Critical Machining Parameters.....	123

Table 4. 19: Surface Roughness Values Based on Both AE Signal Parameters and Critical Machining Parameters 124

CHAPTER ONE

1.0 INTRODUCTION

1.1 Background

Due to its influence on functionality, durability and aesthetics, product surface finish or topology of metallic and alloy components has become a valuable quality during the manufacturing stage. Its importance necessitates the incorporation of an efficient surface finish pre-determination model into the broad manufacturing process to ensure that the specified surface quality is attained. The conventional method of determining surface finish is an instrument called a profilometer. This method involves removing the machined component from the production line, a process that is time-consuming and the contact between the workpiece and the measuring instrument results in damaged product surfaces. Adaptive Neuro-Fuzzy Inference System (ANFIS) is an online and non-contact surface roughness predicting tool that has recently received attention due to its accuracy in single point diamond turning, albeit on materials other than rapidly solidified aluminium (RSA 443) [1, 2]. The accuracy of the ANFIS model is enhanced by using modelling data that is almost the same as training data used [3]. ANFIS eliminates the highlighted problems associated with the manual prediction of surface roughness.

The demand for materials with better thermomechanical properties compared to those of conventional aluminium alloys, has been the driving force behind the emergence of Rapidly Solidified Aluminium (RSA) alloys. The rapid solidification process's high cooling rates yield alloys with a fine microstructure, enhanced strength and better microhardness [4]. These properties ultimately lead to protracted service life and high service performance, making RSAs a material of significant interest. No research has been carried out to investigate the suitability of ANFIS in predicting the surface finish of Rapidly Solidified Aluminium (RSA 443) with small data sets and this investigative research attempts to fill this gap in literature.

During product machining using single point diamond turning process, cutting parameters and process parameters have a great contribution to final surface topology. The interaction between

these parameters during the turning process is complex and non-linear, hence making linear predicting methods unsuitable for use. The other advantage of ANFIS is that it can model complex parameter interactions with higher accuracy than linear mathematical models [5]. An analysis of Acoustic Emission (AE) signals produced during the turning process provides a glimpse on the nature of the interaction between cutting tool and workpiece. This analysis is aided by the availability of modelling methods to transform time domain signals into frequency domain signals. Acoustic Emission (AE) signal count rate, root mean square (AE_{rms}) and prominent frequency of the Fast Fourier Transformed (FFT) signal together with cutting parameters (spindle speed, depth of cut and feed) act as inputs to the ANFIS model in this research. The model output is the profile roughness parameter (R_a) which is a measure of the surface finish integrity. The ANFIS model results are compared to Regression model results using the Mean Absolute Percentage Error (MAPE) method.

This investigative research seeks to address the gap in literature of the unavailability of researches on the suitability of on-line and non-contact surface roughness prediction method in the form of ANFIS on small data sets during single point diamond turning of RSA 443. The research outcome is expected to make commercial optical components surface quality prediction easier, as roughness level can be predetermined.

1.2 Problem Statement

Modern manufacturing processes are striving for continuous release of defect-free machined components from the turning production line. The conventional off-line contact type surface roughness measurement method has the following disadvantages: time-consuming in removing workpiece from Computer Numerical Control (CNC) machine, results in damaged workpiece surfaces due to contact with the measuring instrument, measuring tip wear and accuracy limited by the radius of the tip. Furthermore, the profilometer cannot measure grooves narrower than the tip radius. While a lot of researches have been carried out in optimizing cutting and process parameters during turning of diverse materials, no research has been carried out on ANFIS modelling of RSA 443 surface roughness using small data sets. The use of an on-line surface roughness prediction model in the form of ANFIS will eliminate the problems associated with off-

line measurement methods. The result will be the mass production of high-quality machined components. The accuracy of the Adaptive Neuro-Fuzzy Inference System in modelling RSA 443 surface roughness using small data sets is investigated in this research.

1.3 Hypothesis

Null Hypothesis:

- The Adaptive Neuro-Fuzzy Inference System cannot accurately predict the surface quality of diamond turned aluminium grade (RSA 443) using small data sets.

Alternative Hypothesis:

- The Adaptive Neuro-Fuzzy Inference System can accurately predict the surface quality of diamond turned aluminium grade (RSA 443) using small data sets.

1.4 Aim

To investigate the accuracy of the Adaptive Neuro-Fuzzy Inference System in predicting RSA 443 surface roughness using small data sets.

1.5 Objectives

- i. To measure surface roughness off-line and simultaneously acquire the Acoustic Emission signal.
- ii. To extract prominent parameters from the acquired Acoustic Emission signal (peak rate, root mean square and peak frequency).
- iii. To predict the surface roughness using ANFIS model under different cutting conditions.

- iv. To determine the accuracy of ANFIS model results by comparison to Regression model outputs using Mean Absolute Percentage Error (MAPE).

1.6 Project Scopes

The experiments are designed and conducted based on Taguchi's orthogonal array in this research. The Taguchi experimental design allows numerous parameters to be analyzed without an excessive amount of experimentation. At least nine (9) experimental runs are carried out in this research. Three levels for spindle speed, feed rate and depth of cut are used, with the manufacturer's specified value as the middle value. The three levels chosen will cater for all levels of values (Low (1), Medium (2) and High (3)). Adaptive Neuro-Fuzzy Inference System is used as the modelling tool to achieve the research objectives. The parameters used as inputs to the ANFIS model in this study are cutting speed, feed rate, depth of cut and Acoustic Emission signal components, namely, peak rate, peak frequency and root mean square (AE_{rms}). Focus is on single point diamond turning of rapidly solidified aluminium grade (RSA 443) using a Nanoform 250 ultra-grind Precision CNC machine. The machined components surface roughness is measured off-line by a Taylor Hobson Profilometer while Acoustic Emission Piezotron Sensor is used to acquire the AE signal. The Simulation of results is done in the MATLAB environment. Results from the ANFIS model are compared to Regression model results using the Mean Absolute Percentage Error (MAPE).

1.7 Motivation

This research is motivated by the need for an effective surface quality prediction method for small data sets during the machining of rapidly solidified aluminium (RSA 443) alloys. For this research, an effective method is one that has the following attributes: accuracy, ability to monitor surface roughness online, non-contact and can be integrated into the automated machining system. This method will eliminate the contact-type offline method with its associated limitations.

Companies that use the ANFIS model will enjoy high sales and profits through production of high-quality products that meet both application specifications and consumer taste. The absence of

process pauses in ANFIS surface roughness prediction shortens the total production time while increasing production volume. Because of mass production of machined products, the cost of producing a unit component is lowered. Since the model can be integrated into the automation system, labor costs and human errors will be greatly reduced. Companies that utilize the ANFIS model will have a competitive advantage over those using traditional methods.

1.8 Chapter Layout

This thesis report is partitioned into five chapters:

- Chapter I Introduction/Background: The problem background, objectives and research scopes are presented in this chapter.
- Chapter II Literature Survey: Relevant literature to the study is outlined.
- Chapter III Materials and Methodology: The study material composition, cutting parameters and design of experiment are incorporated.
- Chapter IV Results and Discussion: Analysis of collected results is presented.
- Chapter V Conclusion and Recommendations: The consequence of analysis and recommendation are given in this chapter.

The sequence of the five chapters described are schematically represented by Fig. 1.1.

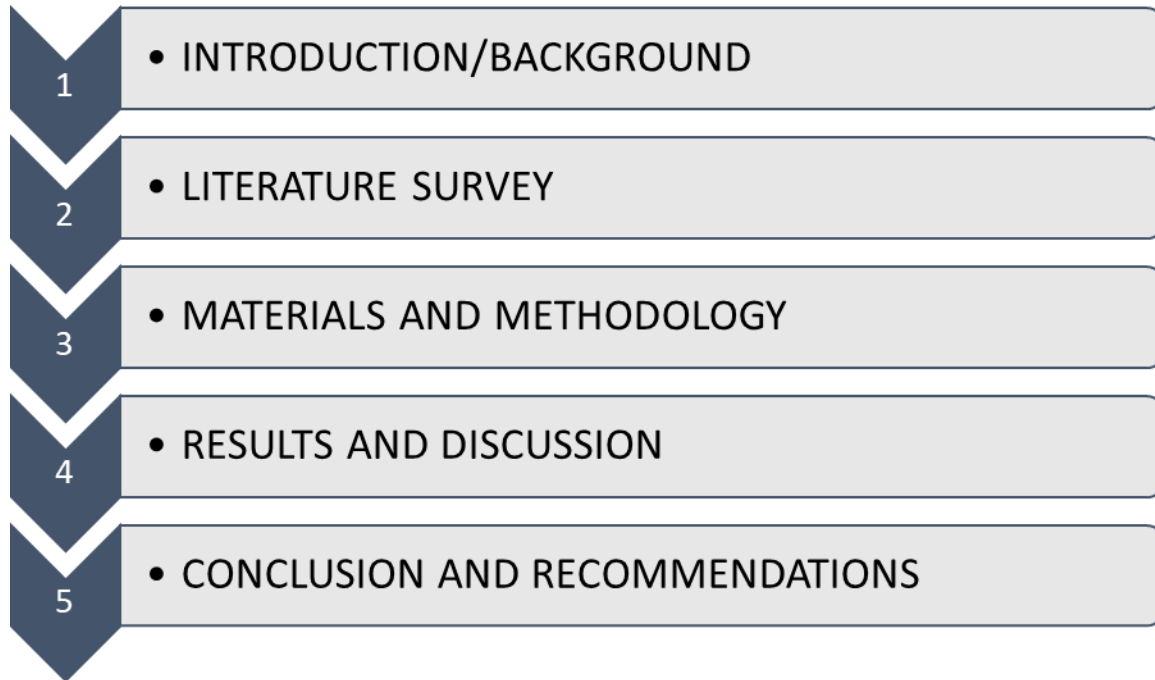


Figure 1. 1: Chapter Layout

CHAPTER TWO

2.0 LITERATURE SURVEY

2.1 Introduction

The literature survey for this investigative research thesis is divided into 5 sections: rapidly solidified aluminium (RSA) alloys, surface roughness in ultra-high precision diamond turning, cutting tool materials, review of acoustic emission and signal processing and computational intelligence. The first section presents the rapid solidification process and properties of rapidly solidified aluminium alloys. The second section presents the surface roughness average parameter (Ra) and the factors that affect it during ultra-high precision diamond turning of RSA 443. The third section presents the diverse cutting tool materials used in turning processes. Emphasis is given to the single point diamond cutting tool that is used in this research. In the fourth section, acoustic emission signal acquisition is presented together with the Piezotron sensor used in this research. The acoustic emission signal parameters are also reviewed in this section. In the last part, a review of Adaptive Neuro-Fuzzy Inference System (ANFIS), Artificial Neural Network (ANN) and Regression model is made.

2.2 Determinants of RSA Alloy Properties

The demand for aluminium alloys with thermo-mechanical properties superior to those of conventional aluminium alloys is the drive behind the emergence of a new generation of alloys called rapidly solidified aluminium (RSA) alloys. Among the most significant property determinants of RSAs are improved microstructure homogeneity, smaller grain size and alloying percentage.

2.2.1 Improved Microstructure Homogeneity Effects on RSA Properties

The rapid solidification process yields aluminium alloys with fine microstructures and are relatively easy to polish to the desired surface finish for applications in the visual spectral range [6]. The relationship between cooling rates and microstructure of rapidly solidified aluminium alloys is represented diagrammatically in Figure 2.1. The diagram shows that increasing the cooling rate reduces the alloy crystal size while improving the homogeneity of the microstructure. Additionally, RSAs have enhanced mechanical strength, relatively high wear resistance, high temperature strength and good thermal expansion [7].

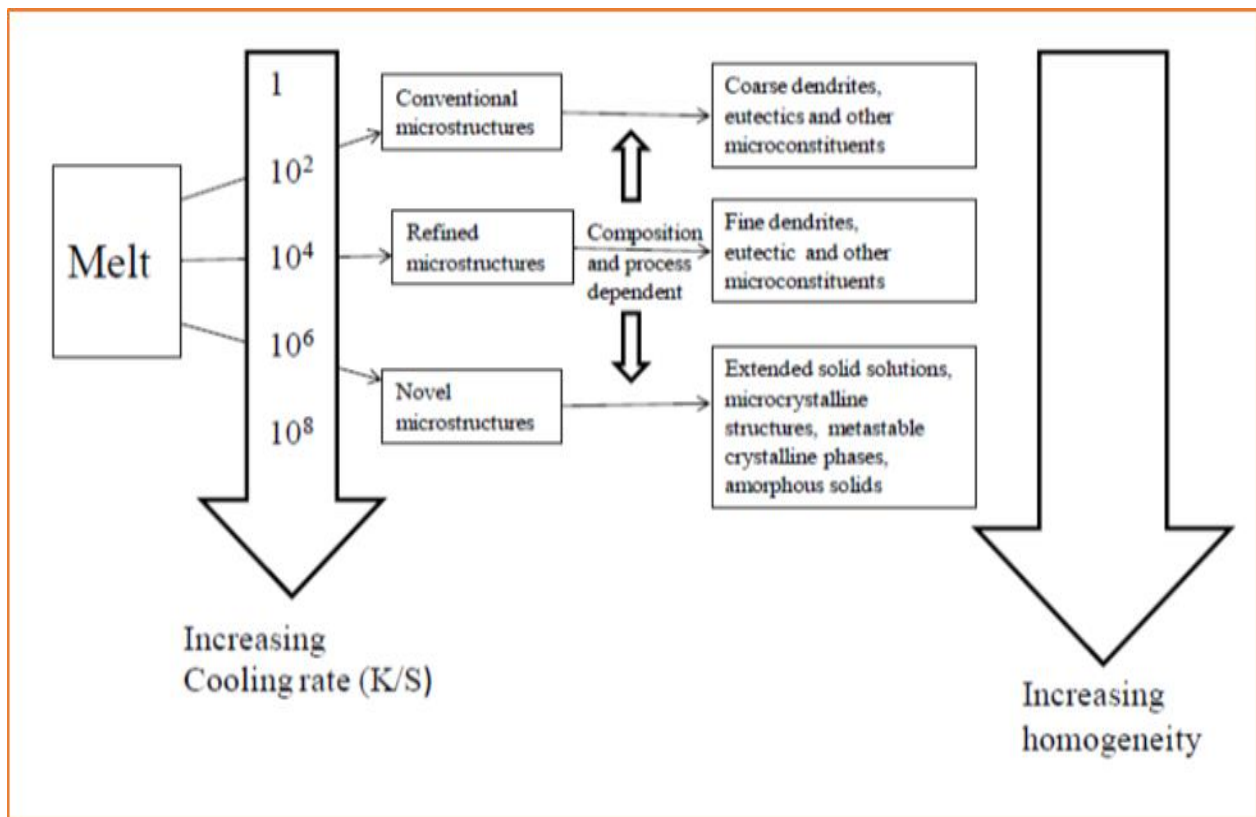


Figure 2. 1: Effects of Rapid Solidification on Microstructure [8]

Abubakre et al. [9] discovered that the final product particle size is improved by raising quenching media temperature and use of a quenching medium with relatively higher heat extraction rate. Selection of the proper quenching media is therefore, a task that must be undertaken judiciously as it influences final product quality.

2.2.2 Small Grain Size Effects on RSA Properties

Aluminium's use as a lightweight structural material is limited by its lack of strength both at room temperature and high temperature when compared to steel [10]. This deficiency is fixed by the addition of alloying elements during the rapid solidification process to produce aluminium alloys with enhanced strength. According to Katgerman [7], "the higher the cooling rate, the finer the microstructure and the better the properties". By reason of having finer and well distributed granules, rapidly solidified aluminium alloys enjoy relatively better mechanical properties in comparison to conventional aluminium alloys. Subsequently, rapidly solidified aluminium alloys have relatively high tensile strength and impact toughness [11]. The increase in mechanical strength with reduction in grain size is in accordance with the Hall-Petch relationship shown by equation (2.1). Smaller grain sizes lead to grain boundaries that act as barriers to dislocation [12, 13]. From the equation, the smaller the grain size diameter, the higher the yield stress.

$$\sigma_y = \sigma_0 + \frac{K_y}{\sqrt{d}} \quad (2.1)$$

Where σ_y = yield stress.

σ_0 = materials constant for the starting stress for dislocation movement

K_y = strengthening coefficient

d = grain diameter

2.2.3 Alloying Percentage Effects on RSA Properties

A composite of two or more elements, with at least one of the elements being a metal is called an alloy [14]. Alloys are a result of the need to enhance the mechanical and chemical properties of the original element to fit target application. The percentage of silicon in RSA 443 plays an integral role in the determination of strength. Silicon, which constitutes 40% by weight, is a valuable constituent element in rapidly solidified aluminium alloy (RSA 443) and is responsible for high hardness, abrasive resistance, tensile and yield strength of the aluminium alloys [15, 16]. Table 2.1 shows the effects of increasing silicon in Al-Si alloys. There is a general increase in Mean Ultimate Tensile Strength of the Al-Si alloy with an increase in silicon content.

Table 2. 1: Effects of Increasing Silicon in Al-Si Alloys [8]

Material	Specimen	Ultimate Tensile Strength (N/mm²)	Mean Ultimate Tensile Strength (N/mm²)
Al-Alloy (1.5 % Si)	1	119.21	120.87
	2	122.54	
Al-Alloy (3.0 % Si)	1	129.12	130.88
	2	132.65	
Al-Alloy (4.5 % Si)	1	138.24	139.74
	2	141.25	
Al-Alloy (6.0 % Si)	1	148.74	148.99
	2	149.25	

The high silicon content in the aluminium alloys is responsible for the decrease in machining cutting forces, ultimately increasing the machinability of rapidly solidified aluminium alloys. The cutting forces increase with a reduction in cutting speed. There is an inverse relationship between surface roughness and silicon content, that is, an increase in silicon content yields finer surfaces [17]. The frictional properties of Al-Si alloys are strongly influenced by the distribution and shape of silicon particles embedded in the alloy. It is these desirable frictional properties that have led

Al-Si alloys to find applications in the manufacture of bearings, engine pistons and cylinder linings.

2.3 Production Methods of Rapidly Solidified Aluminium Alloys

The three production methods of rapidly solidified aluminium alloys are as follows: spray forming methods, laser surface melting methods and chill methods. The most familiar among these are spray forming and chilling methods. Greater concern has been on the chilling methods, principally the melt spinning process due to its capability to mass produce and its relatively high cooling rate in the range 10^4 - 10^7 K/s [18].

2.3.1 Spray Forming Method

The alternative name for the spray forming method is the Osprey process, a name derived from the Osprey Metals of Neath, a company that commercialized it in the 1970s [19]. The advantages of rapid solidification and powder metallurgy are fused together in the Spray forming method to produce aluminium alloy matrices of marvelous qualities. The desirable attributes of the Osprey process products comprise fine microstructure, near zero segregation, high density of Al-Si alloy, short production path and improved mechanical properties. As described by Singer [20], it is feasible to add second or third phase by superposing the added phase current into the vaporized phase prior to deposition

A schematic representation of the spray forming method is given in Figure 2.2. The melt stream is sprayed through a nozzle by means of an inert gas such as Argon or Nitrogen. The vaporized gas is accelerated towards a suitable substrate, forming a billet in the process. Segregation challenges related to conventional casting techniques are appropriately eradicated by the spray forming method [21]. There is significant reduction in process steps from melt to final product and capability of manufacturing difficult-to-manufacture components by spray forming.

Owing to minimal process steps in spray forming, production rates are higher and manufacturing costs are subsequently lower. The lower handling time in spray forming methods translates to

reduced chances of oxide contamination and hence improved fracture resistance and fatigue life. Because of the fine microstructure, spray formed alloys can be easily machined to the required smoothness and have high wear resistance [22].

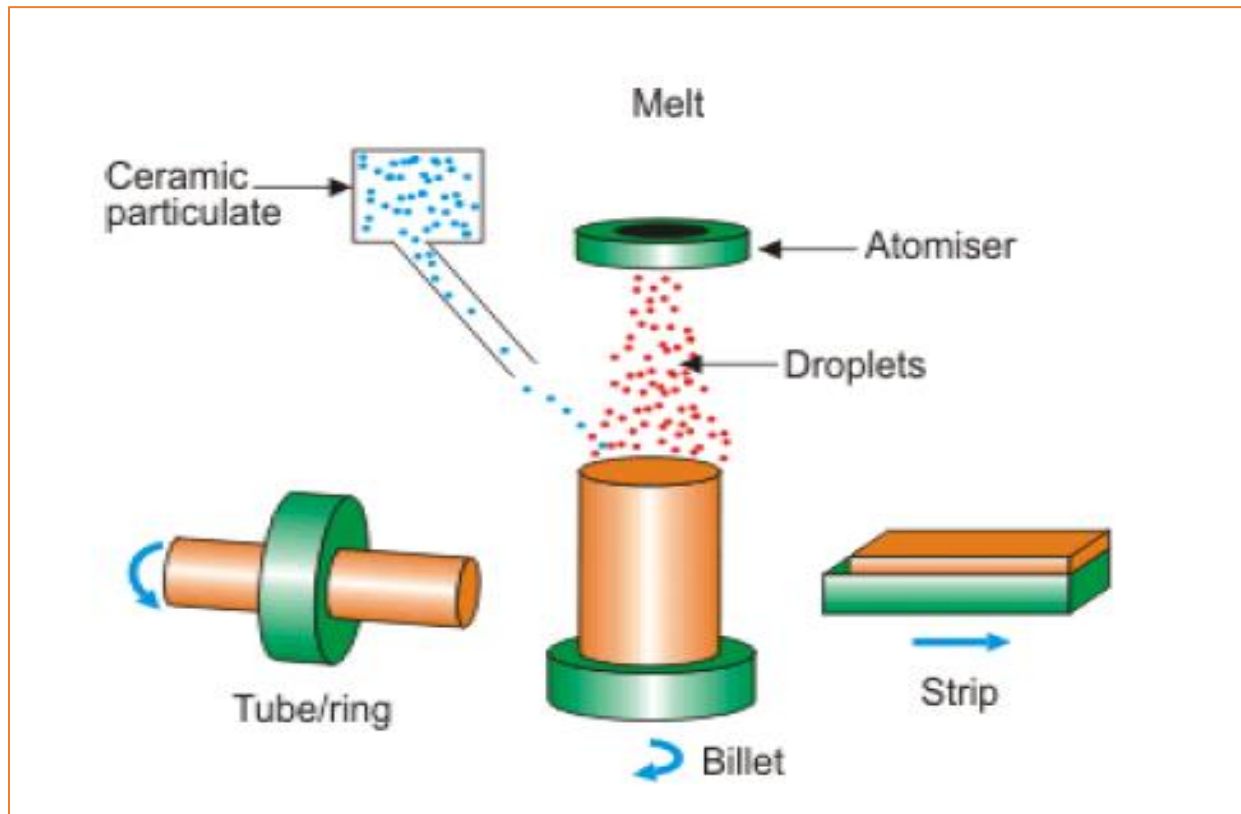


Figure 2. 2: Spray Forming process schematic [23]

2.3.2 Laser Surface Melting Methods

Laser Surface Melting method has the flexibility to achieve a wide spectrum of cooling rates through variation of parameters such as scan-speed and laser power. In the Laser Surface Melting method of rapid solidification of aluminium alloys, melting and solidification take place at the workpiece surface. A traversing laser source in either single pulse form or continuous beam form melts the workpiece surface that simultaneously acts as a heat sink during the solidification phase [24]. The flux formed because of the traversing laser beam is subjected to rapid solidification

through heat transfer to the heat sink. It is this rapid solidification that determines the microstructure of the formed component. Figure 2.3 shows the principle of rapid solidification using the laser surface melting method.

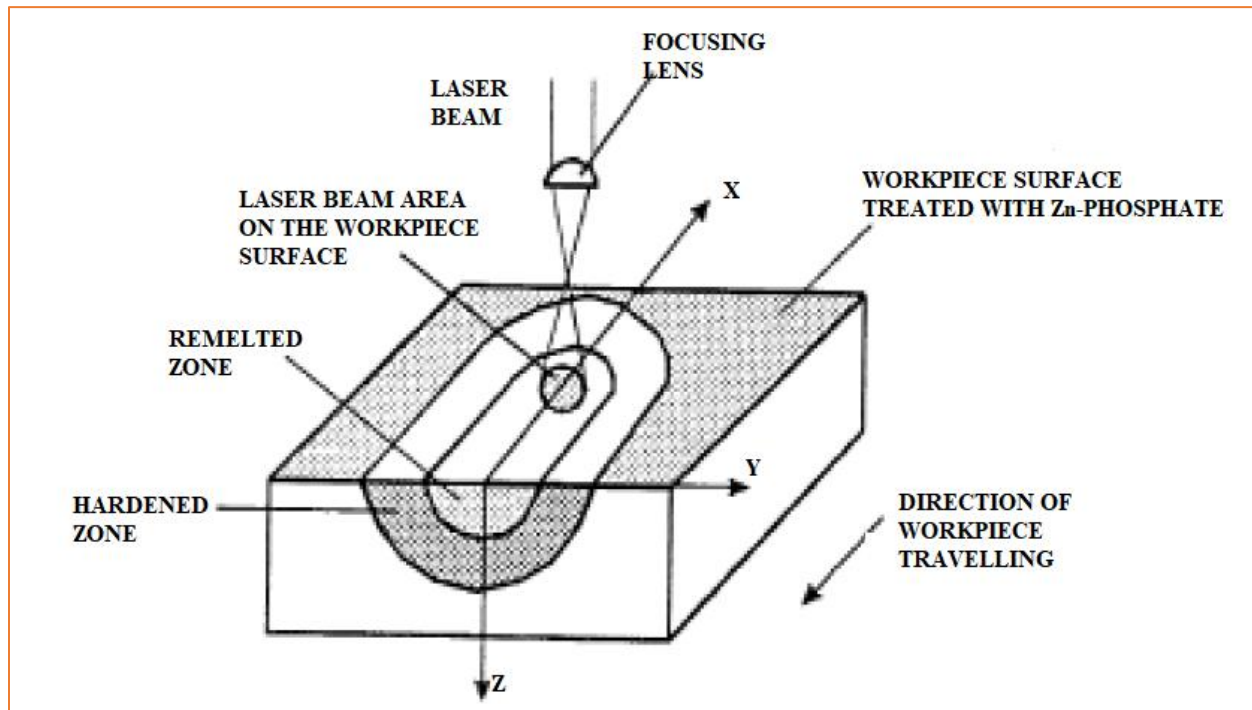


Figure 2. 3: Principle of rapid solidification at the surface showing rapid local melting with a traversing heat source [25]

The three solidification parameters, namely, temperature, thermal gradient and cooling rate have a bearing on the final product quality, hence the need to accurately control them. Figure 2.4 represents the temperature profile along the Laser movement direction. It shows that the melt-pool temperature at the laser point of contact is higher than that of the neighboring regions. The temperature gradient, defined as the ratio of the temperature difference between two points to the distance between the points is represented by the steep slopes on either side of the laser melt pool. The cooling and heating temperature gradients are represented by left-side and right-side gradients

respectively. The temperature peak due to superheat prior to melting is represented by a local maximum ahead of the flux [26].

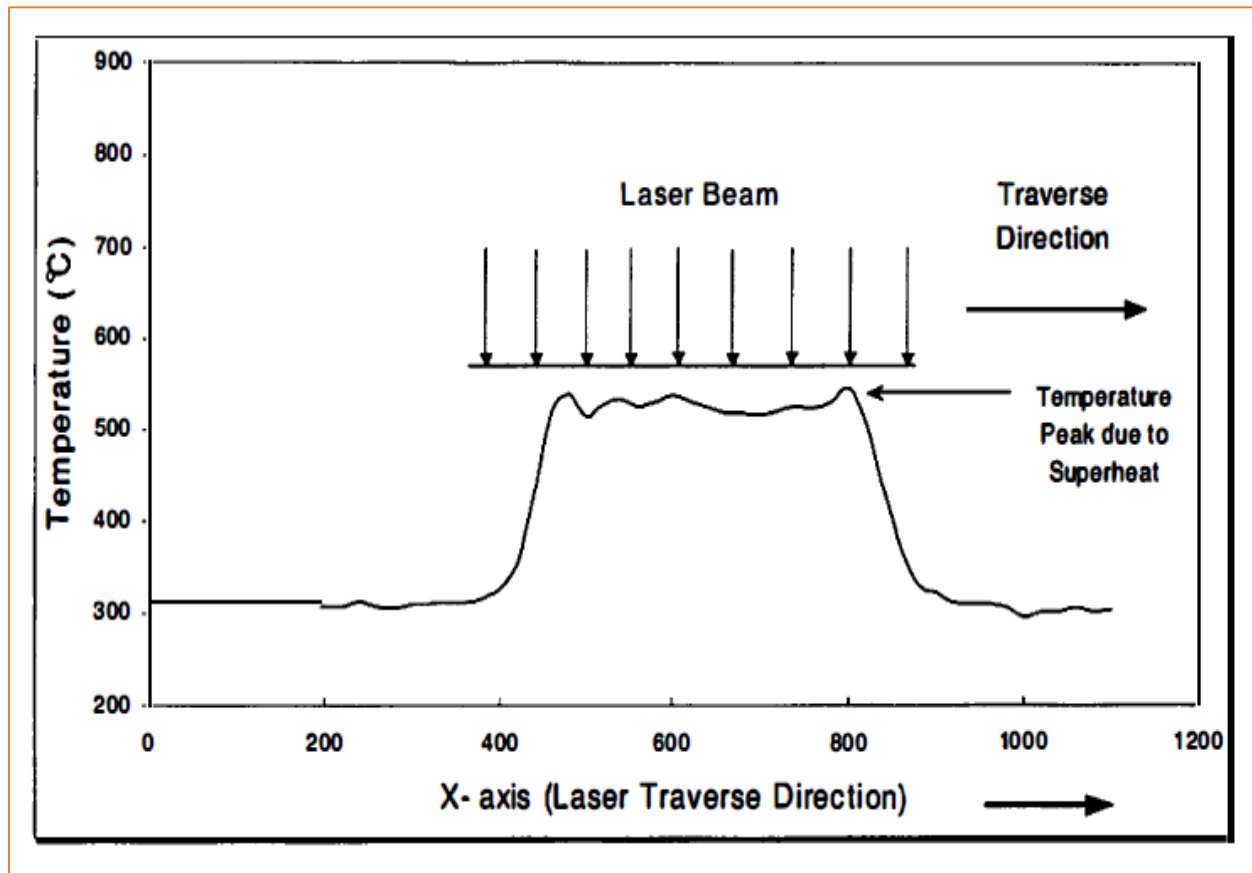


Figure 2. 4: Temperature variation along the beam path [26]

2.3.3 Chill Methods

The melt spinning method of rapid solidification was developed in 1960 by Duwez and his co-workers [27]. Of the three methods of rapid solidification of aluminium, melt spinning is the most widely used industrially due to its high cooling rate and the ability to process large volumes of materials. Thin metal strips of alloys are produced on a refrigerated rotating disc drum surface in an inert environment. The freezing of silicon in the melt spinning process results in high silicon content, that is 40% in RSA-443 [28]. Molten material is forced under pressure through a crucible

hole on to a rotating drum surface that is refrigerated inside to enhance the cooling process. The process schematic is shown in Figure 2.5.

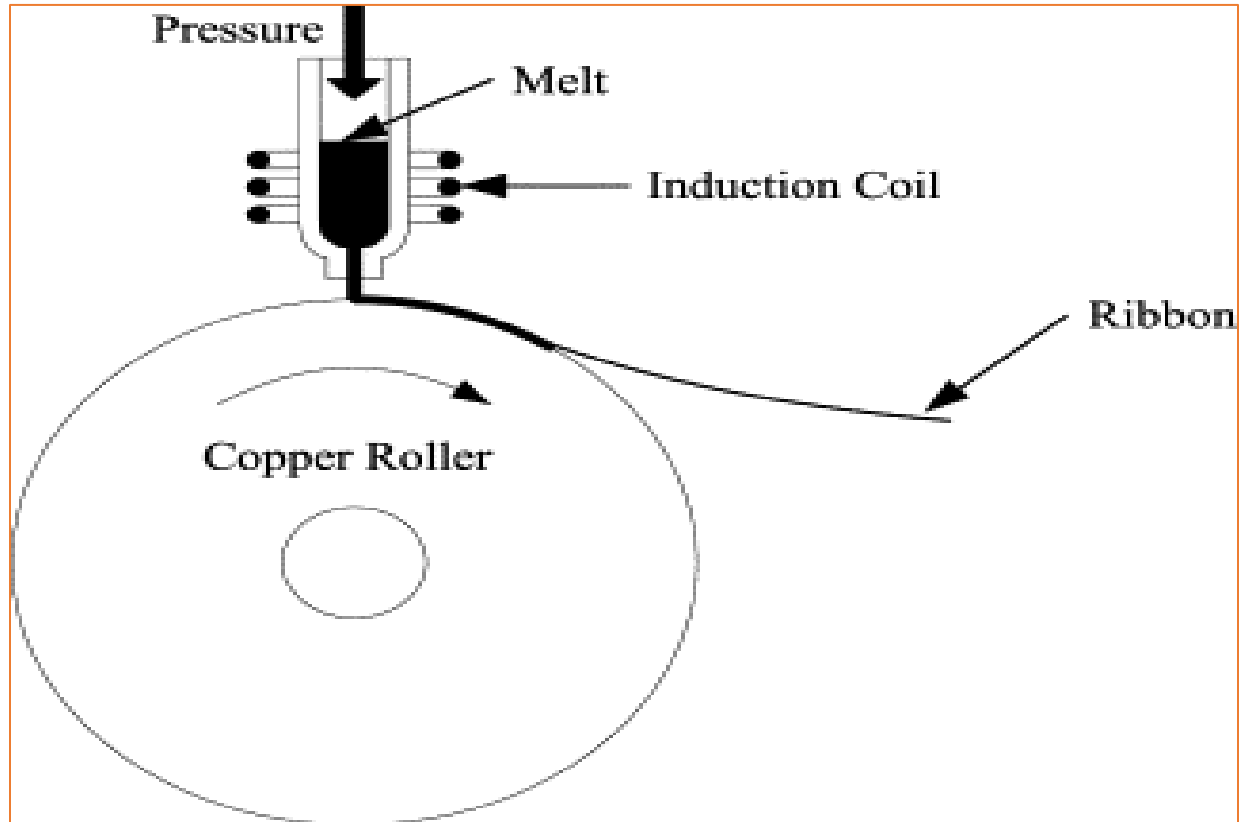


Figure 2. 5: The melt spinning process [29]

2.4 Surface Roughness in Ultra-High Precision Diamond Turning

2.4.1 Surface Roughness Parameters

A sharpened single point diamond cutting tool is employed in Ultra-High Precision Diamond Turning (UHPDT) of aluminium alloys to produce optical surfaces that fit application specifications. Surface roughness parameters are used to quantify the surface deviation from its ideal form. Vorbuger and Raja [30] highlighted that roughness average perimeter (R_a) and peak surface roughness spacing (D) are critical parameters in surface roughness evaluation as they

determine functionality and performance of machined surfaces. Figure 2.6 is a schematic representation of the two parameters. Roughness average perimeter (R_a), represents vertical deviation from the horizontal line of a machined surface. Large deviations signify a rough surface; while small deviations signify a smooth surface [31].

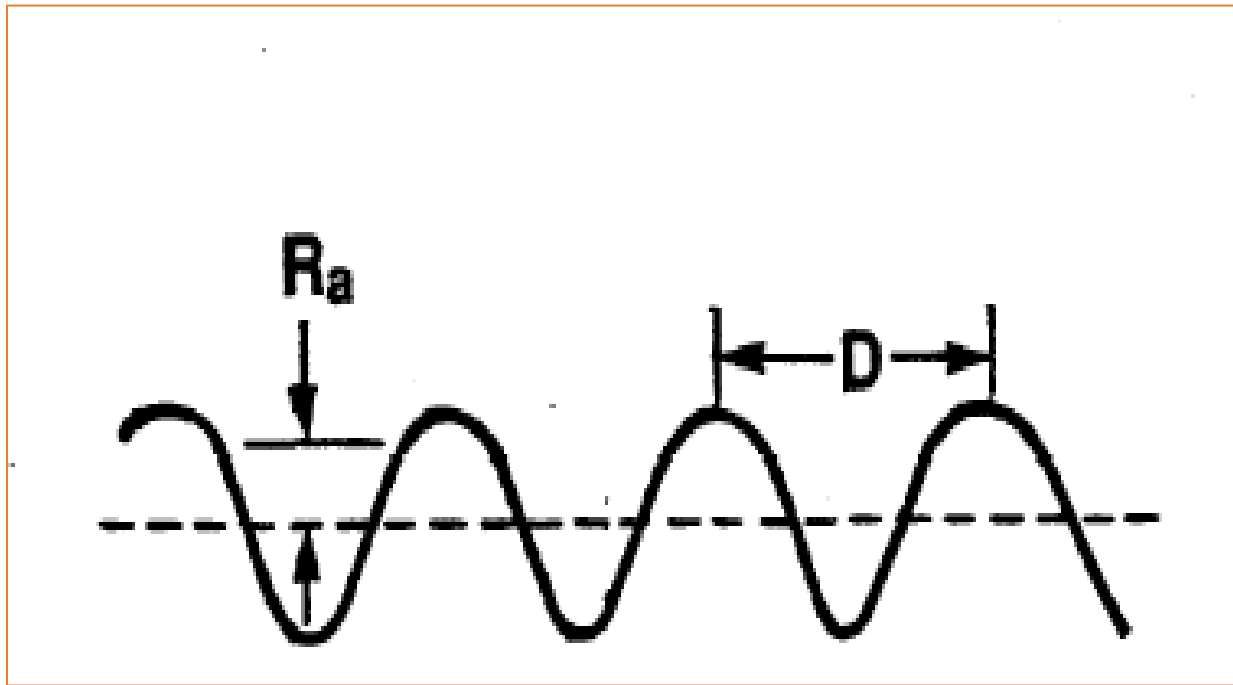


Figure 2. 6: Roughness Average Perimeter and Peak Surface Roughness Spacing [30]

Between the two parameters, only R_a is considered in this investigative research thesis. The lowest achievable value of roughness average perimeter for any turning process is theoretically given by equation (2.2). Grzesik [32] found out that at low feed, the theoretical roughness is less than the actual roughness. There is an extension of plastic deformation to the work piece surface from the cutting region which is later recovered after the turning process [33].

$$R_a = 0.0321 \times \frac{f^2}{r} \quad (2.2)$$

Where f =feed in mm/rev

And r =tool tip radius in mm

The other factors with significant contribution to the actual roughness are cutting conditions, machined material mechanical properties, tool vibrations and chip formation mechanism [34].

2.4.2 Effect of Material Characteristics on Surface Roughness

The material characteristics that affect surface topology during ultra-high precision diamond turning are crystal orientation, swelling and material anisotropy. Crystal orientation to the cutting tool determines the cutting force as some directions are more favorable for shear plane formation than others [35]. The effect of crystal direction becomes more significant as the uncut chip thickness approaches the material grain size. In ultra-high precision diamond turning, the uncut chip size is smaller than the average grain size of the material. At this level however, the tool will be cutting through ideal crystals of the material, the surface topology is affected by their orientation and properties [36, 37].

A complex combination of processes that include material swelling, plastic deformation and elastic recovery determines the nano-scale surface topology formation during ultra-high precision diamond turning. Kong [38] defined materials swelling as, “the elastic-plastic response of the work piece when the cutting tool is removed”. Tool mark deviation from the prescribed profile on the workpiece surface is a result of material swelling. Therefore, surface topology cannot solely be reduced by optimization of process parameters [39]. Many researches have been carried out to investigate material swelling effect on surface topology and the results indicate that surface topology is distorted by material swelling [40, 41].

2.4.3 Temperature Effect on Surface Roughness

The conventional way of maintaining temperature to avoid adverse thermal effects during Ultra-High Precision Diamond Turning (UHPDT) involves the use of coolants. Despite the use of coolants, the transfer of heat from the cutting point to the workpiece is inevitable. The temperature induces thermal errors on the machined component surface finish. During UHPDT, the heat is

transmitted from one layer to the adjacent layer resulting in component swelling. When the heat is lost, the component does not recover its original shape uniformly, resulting in non-uniform surface roughness [42].

The temperature generated at the cutting point induces cutting tool dimensional changes that shift the tool cutting point, leading to dimensional errors. Besides its direct effect on surface roughness through induction of dimensional errors, temperature also indirectly affects surface roughness through tool geometry modification due to tool wear. There is a direct relationship between the generated temperature and tool wear. The temperature is a function of workpiece material and cutting parameters. It is therefore important that the cutting parameters be carefully selected before any cutting operation as the machining cost is affected as well [43]. The three zones of heat generation during the cutting process are: plastic deformation by shearing in the primary shear zone; friction on the cutting face and friction between the chips; tool on the tool flank [44]. The heat generation zones are indicated in Figure 2.7.

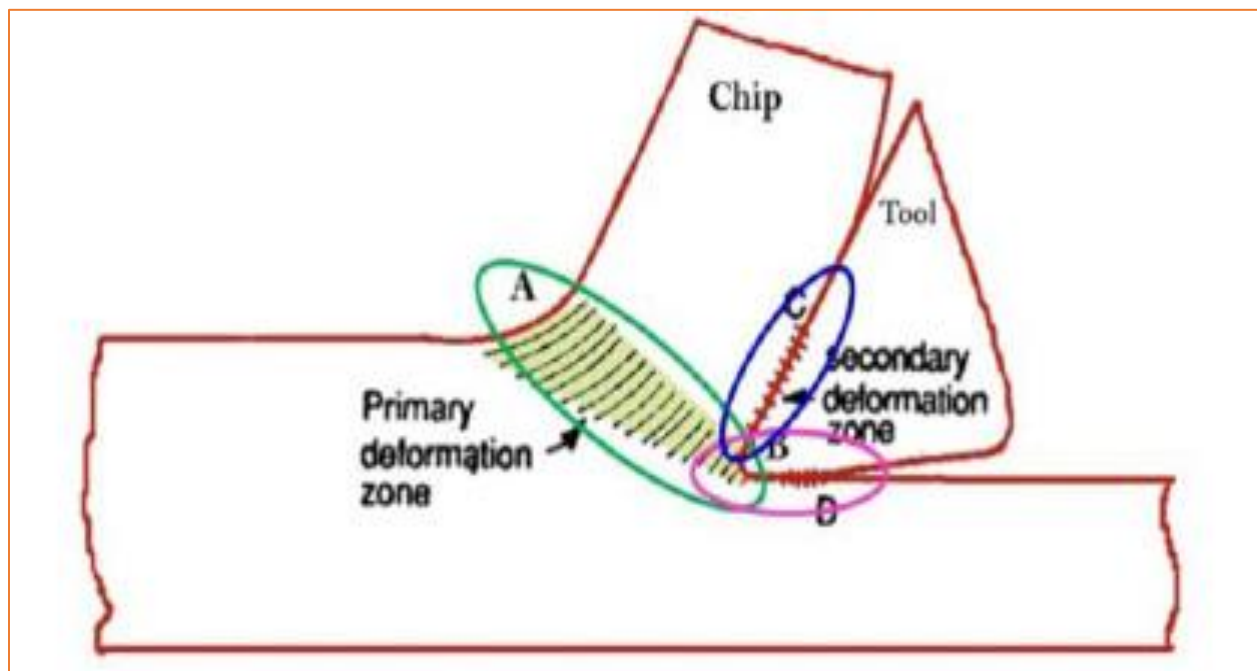


Figure 2. 7: Heat generation zones [44]

2.4.4 Tool Vibration Effect on Surface Roughness

The relative vibration among cutting tool, workpiece and measuring instrument has adverse effects on surface topology of a machined component [45]. Principally, the relative vibration between the cutting tool. The defective surface topology, induced dimensional errors and enhanced tool wear negatively influence the cost of production and productivity [46]. Numerous researches have been conducted to investigate the effects of tool vibrations on surface topology of machined components [47-49]. From these researches, it was discovered that vibrations play a significant role in defining surface topology during machining, hence the need to control them.

The three primary categories of machine vibration are free vibrations, forced vibrations and self-excited vibrations. Free vibrations are a consequence of internal forces in the system and they ultimately die out over time [50]. Forced vibrations are a consequence of external force agitation while self-excited vibrations are spontaneous and lead to amplitude boost up to a maximum point. The dynamic interaction between the cutter and the workpiece during a turning process causes self-excited vibration [51]. According to Amin et al. [52], “tool chatter is an undesirable vibration aspect that leads to an increase in vibration amplitudes because of excitation frequency being the same as the natural frequency of the cutting tool”. The net result is the adverse effect on surface quality. Additionally, chatter also negatively impacts on tool wear, material removal rate, production time and energy consumption [53].

2.4.5 Cutting Parameter Effects on Surface Roughness

The most popular cutting parameters that have been researched on are cutting speed, feed rate, depth of cut and tool nose radius; and a combination of these cutting parameters is an integral determinant of product surface finish. It is crucial for the cutting parameters to achieve the required surface finish during the turning process. Due to the uniqueness of every material, different cutting parameter combinations are used to achieve that. Numerous studies have been conducted to investigate the effects of every cutting parameter in the machining of various materials.

Imhade and Ugochukwu [54] investigated the order of influence of cutting parameters during the end milling of aluminium and concluded that spindle speed has the greatest influence, followed by

feed rate and finally depth of cut. Abdullah et al. [55] investigated the effect of feed rate and cutting speed on surface topology of aluminium. The conclusion was that feed rate plays the most significant role followed by cutting speed. The results indicate that besides material properties, the machining process influences the significance of cutting parameters.

Surface roughness and cutting speed are inversely related, that is, increasing the cutting speed reduces the surface roughness. There is a direct variation of feed rate and surface roughness, that is increasing the feed rate increases the surface roughness, and vice versa. There is a direct proportion between depth of cut and surface roughness. It has also been concluded that there is an inverse relationship between tool nose radius and surface roughness, that is, increasing tool nose radius reduces the surface roughness [56].

2.4.6 Tool Geometry Effect on Surface Roughness

Tool geometry refers to the outline and angles of the cutting segment of the cutting tool (see Figure 2.8). Taha et al. [57] found out that during the turning process, the tool geometry has a significant effect on surface integrity, tool life and cutting efficiency, hence the urgency for appropriate tool selection prior to machining. According to Gökkaya and Nalbant [58], “the least possible average surface roughness has been obtained using the cutting tools of maximum insert radius (1.2 mm)”. This signifies that broad edged tools produce greater axial and radial forces than narrow edged tools and the cutting tool chamfer angle is directly proportional to the cutting force. Tool life is enhanced by use of a cutting tool with a greater chamfer angle as the wedge strength is increased, though this is only up to a certain level, after which the tool life begins to diminish. At higher cutting speeds, there is an inverse relation between chamfer angle and surface roughness. Additionally, a higher chamfer angle produces low surface roughness at higher cutting speed [59]. The geometry of a single point cutting tool is shown in Figure 2.8.

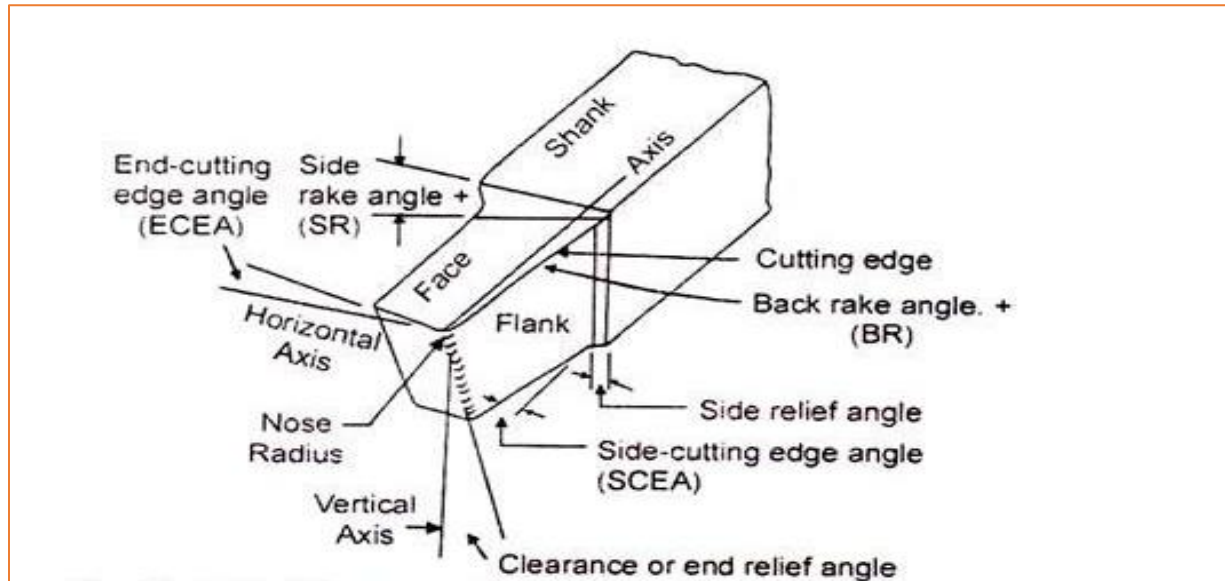


Figure 2. 8: Tool Geometry of Single Point Cutting Tool [60]

2.4.7 Surface Roughness Effects on Fatigue Life

For applications where components are subjected to cyclic loading such as in aeroengine parts, fatigue is of predominant concern since it affects safety, product life and operating costs. It was discovered that the fatigue strength is affected by the severity and the machining process used to produce the component [61]. Fatigue crack development starts on component surface and since a high surface roughness promotes crack formation, the material fatigue strength is therefore dependent on surface roughness. There is a direct relationship between the fatigue life of a machined component and surface finish, that is, the better the surface finish, the higher the fatigue life (see Figure 2.9). Further, cutting speed and feed rate have a greater influence on fatigue life than depth of cut [62]. Maiya and Busch [63] investigated the effect of surface roughness on fatigue life of stainless steel (grade 304) and discovered the relationship represented by equation (2.3).

$$N_0 = 1012 \times R_q^{-0.21} \quad (2.3)$$

Where N_0 = initiation component of total fatigue life

And R_q = root-mean-square roughness (μm).

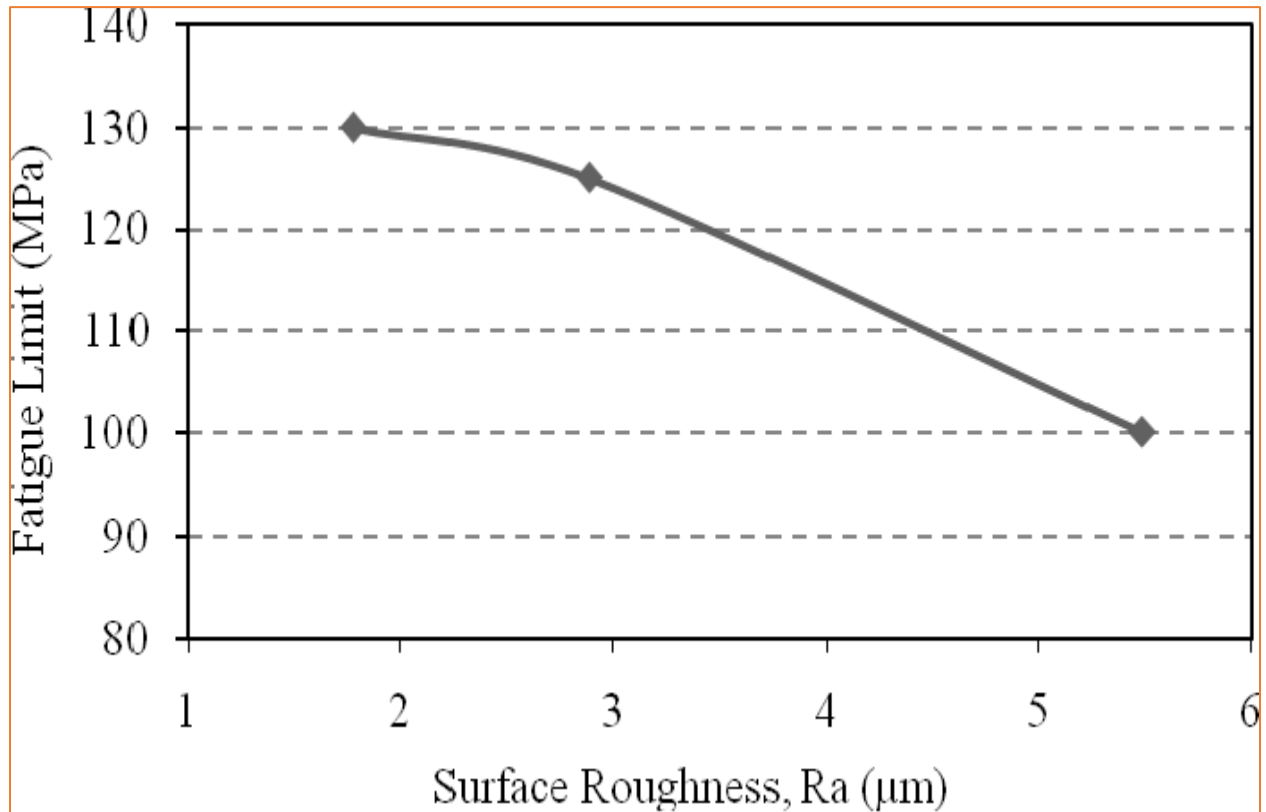


Figure 2. 9: Surface Roughness versus Fatigue Limit [64]

2.5 Cutting Tool Materials

2.5.1 Single Point Diamond

A Single Point Diamond (SPD) cutting tool derives its name from the single diamond crystal that is either natural or synthetic, which is fixed on the cutting tool tip and finally smoothed by grinding and polishing processes. The single diamond crystal is fixed by high pressure onto a layer of tungsten carbide substrate (see Figure 2.10).

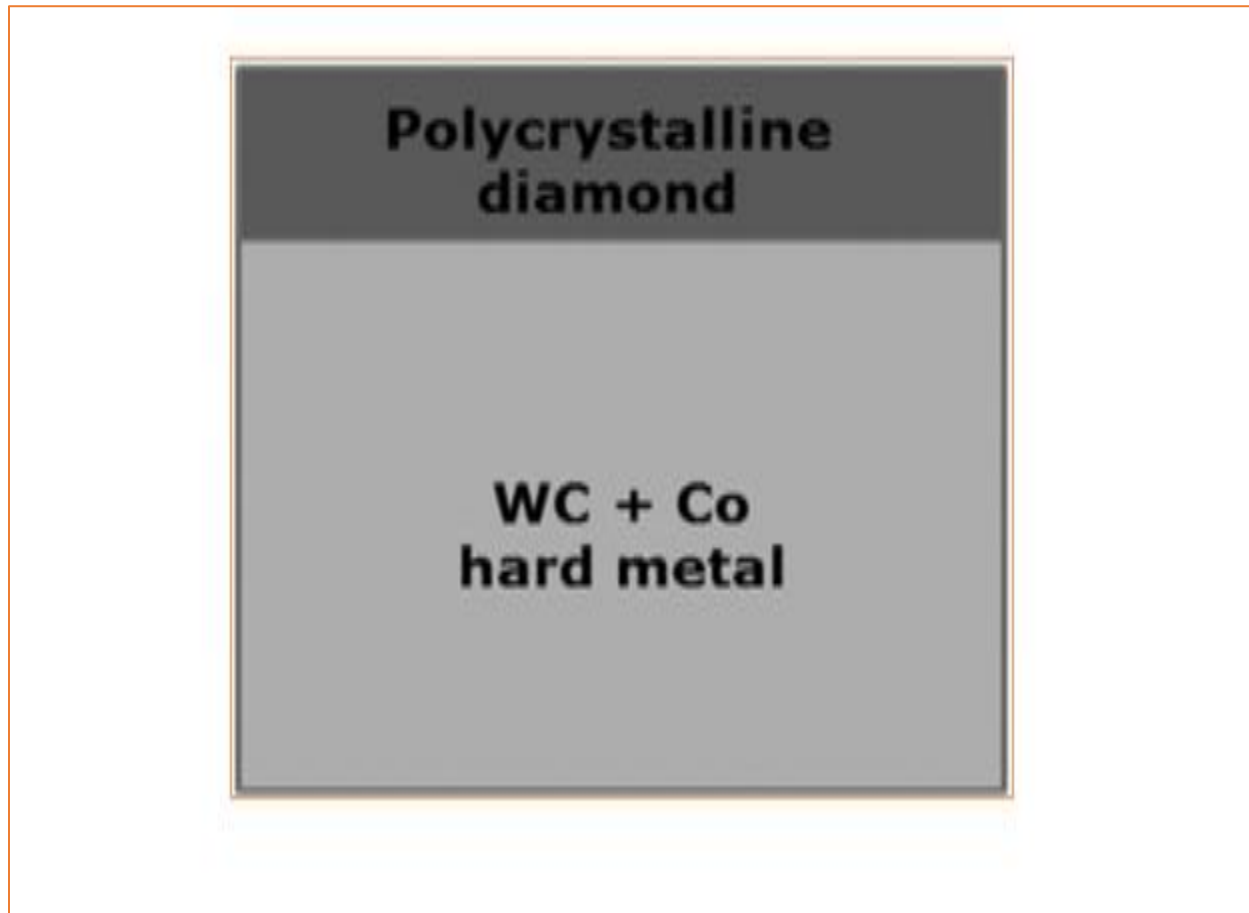


Figure 2. 10: Geometry of a typical single point diamond cutting tool [65]

Nakasuji et al. [66] observed that single point diamond tools can attain surface finish accuracies of micro/nanometer levels. Diamond is the toughest material in existence and it is the best tool to machine non-ferrous, non-metallic and abrasive materials [65]. Single point diamond tools have high hardness, high abrasion resistance, high strength and great shock resistance [67]. The numerous applications of SPD include the machining of reinforced plastics, marble, granite, copper and aluminium alloys [68]. For the same machining operation, SPD tools enjoy longer tool life than carbides, hence greater cutting speeds are used. A comparison between single point diamond (SPD) tools and carbide tools is given by Table 2.2.

Table 2. 2: SPDT and carbide comparison data [69]

Parameter	Carbide Tool	Diamond Tool
Initial Cost	\$149-00	\$1 451-00
Sharpening Cost	\$14-00	\$250-00
Machine Cost (per minute)	\$0-85	\$0-85
Setup Time	15 min.	15 min.
Possible Resharpenings	14 times	6 times
Tool Life	2 500 linear feet	150 000 linear feet

The presented results indicate that single point diamond cutting tools are generally superior to carbide cutting tools. This is attributed to the high elastic modulus of diamond (1000GPa) which signifies high specific stiffness. The cutting tool withstands high machining forces without undergoing any major deformation. Despite the numerous advantages, a single point diamond cutting tool has its own share of disadvantages, among which are its transformation to graphite at high temperatures and the relatively initial cost of the cutting tool [70].

2.5.2 Carbon and Medium Alloy Steels

Carbon steels are clustered according to carbon percentage as follows: low carbon steel, medium carbon steel and high carbon steel as indicated in Table 2.3.

Table 2. 3: Carbon Steel Categories [71]

Carbon Steel Category	Carbon Percentage
Low carbon steel	0-0.30%
Medium carbon steel	0.31-0.60%
High carbon steel	0.61-1.00%
Ultra-High carbon steel	1.25-2.00%

Due to their lower cost, low carbon steels are the most common among the three groups [71]. High carbon steel is alternatively called carbon tool steel, a name derived from its use as a cutting tool material because of its hardness. While steel hardness increases with an increase in carbon content, brittleness is negatively affected. The difference between carbon steels and alloy steels lies in the inclusion of other elements in addition to carbon. Prominent elements are manganese, silicon, nickel, titanium, copper, chromium and aluminium. The choice, proportion and combination of the alloying element is determined by the required application specific properties.

2.5.3 High Speed Steels

High Speed Steel (HSS) is an alloy of iron, vanadium, chromium, carbon, molybdenum and tungsten. The name was derived from the ability to machine at relatively higher speeds than carbon and medium alloy steels. High Speed Steel can efficiently cut in extreme temperatures (1000F) without losing its hardness [72]. The desired cutting tool properties such as wear resistance, heat resistance, high toughness and high hardness response are attained by combining the respective elements in well-designed proportions. High speed steels are clustered into three broad categories based on the proportion of major constituent elements, namely tungsten, molybdenum and cobalt. Table 2.4 shows the nominal chemical compositions of the common high-speed and intermediate high-speed tool steels in use. From the table:

- T1- titanium steel
- M1, M2, M7, M50- Molybdenum steels
- M35, M42- Cobalt steels

Table 2. 4: High Speed Steel Chemical Composition [73]

Grade	Cr	Mo	V	Co
T1	4.00	-	1.00	-
M1	4.00	8.00	1.00	-
M2	4.00	5.00	2.00	-
M7	4.00	8.75	2.00	-
M35	4.30	5.00	1.80	5.00
M42	3.75	9.50	1.15	8.00
M50	4.00	4.25	1.00	-

2.5.4 Carbides

The need for heat resistant cutting tools in modern manufacturing processes is being necessitated by the ever-increasing need for high metal removal rate. This has led to a transition from the use of high-speed steels to carbides, whose cutting speeds are 3-5 times faster. The carbide cutting tool is composed of powdered carbide particles bound together by a cobalt matrix binder and exists in the following categories: tungsten carbide, titanium carbide, tantalum carbide and niobium carbide [74]. The proportion of each constituent element in the cutting tool significantly affects the properties of the cutting tool. It is recommended that the manufacturer's specified grade be used to enhance tool life and cutting speed. Table 2.5 shows the different grades and the best conditions for their applications.

Table 2. 5: Carbide Grades and Applications

Carbide Grade	Condition of Application
Shock-Resistant Carbide	Interrupted Cutting
Harder, Chemically Stable Carbide	High Speed Finishing
Heat-Resistant Carbide	Super Alloy Machining

2.5.5 Polycrystalline Diamond

Polycrystalline Diamond (PCD) was introduced as a means to improve Ti6Al4V used in the aerospace industry [75]. PCD tools are formed by high pressure and temperature combination of minute synthetic diamond particles using a carbide substrate binder and cobalt catalyst. The presence of cobalt results in an electrically conductive composite that demands the use of electrical discharge machining method in conjunction with PCD. PCD is an isotropic material that exhibits a unique and desirable property for a cutting tool in its qualification to be brazed [76]. In the formation of a composite material based cutting tool like PCD, it is crucial to balance between toughness and wear resistance as both are desirable qualities. Abdul-Rani et al. [77] found out that PCD cutter wear resistance is enhanced by reduction of diamond grain size.

2.6 Review of Acoustic Emission and Signal Processing

2.6.1 Acoustic Emission Sensors

An acoustic emission sensor is defined as a device which detects an acoustic wave and converts it into an electrical signal. It utilizes multiple physical detection principles that include electromagnetic, capacitive, magnetostrictive, piezoelectric and interferometers. Selection of an appropriate sensor is governed by the correlation between input and output signals. A perfect sensor choice is one that would give an output voltage-time curve equivalent to the input

amplitude-time curve [78]. Due to the wide frequency spectrum and diverse acoustic signal modes, almost any sensor can detect some AE. For the purposes of this research, piezoelectric sensors will be discussed.

Non-destructive sensing techniques are categorized into two broad groups, namely, passive and active techniques. Active sensing techniques require an input to detect a parameter while passive techniques do not require any input. Piezoelectric acoustic emission sensors are classified under non-destructive sensing techniques since they do not require any input but only the detection of energy released from the workpiece under investigation [79]. Owing to the numerous advantages of non-destructive testing methods, much ground has been gained in terms of their implementation in industrial test applications. The state of in-service components can be assessed without physical property alteration. Valuable information such as crack growth and plastic deformation can be acquired from acoustic emission signals to ascertain the service state of structures such as metal pressure vessels, piping systems and reactors [80]. During the turning process, the acquired acoustic signal is processed and analyzed for use in tool condition monitoring and surface roughness prediction.

2.6.2 Acoustic Emission Sensor Piezoelectricity

Component loading is correlated with stress energy discharge. The resultant transient elastic waves propagate inside the material before detection by an acoustic emission sensor. Acoustic emission sensors employ the piezoelectric effect in their operation. Piezoelectricity is a pairing phenomenon between strain and electric polarization that results in generation of electric charge in materials subjected to applied stress. The generated charge is directly proportional to the strain. Examples of piezoelectric materials are quartz, Rochelle salt, ammonium dihydrogen phosphate and ferroelectrics [81]. Advances in research have made it possible to produce ferroelectric ceramics with superior properties to piezoelectric single crystals. These are common in most acoustic emission sensors today.

Piezoelectric material diameter and thickness are crucial dimensions that define sensor sensitivity. The Boston Piezo-Optics Inc. defined sensitivity as the smallest change in input signal that a

transducer can detect [82]. Resonance frequency of the sensor is determined by the element's piezoelectric and elastic constants. The structure of the Piezotron sensor is shown in Figure 2.11. The sensor case acts as a shield against electromagnetic interference.

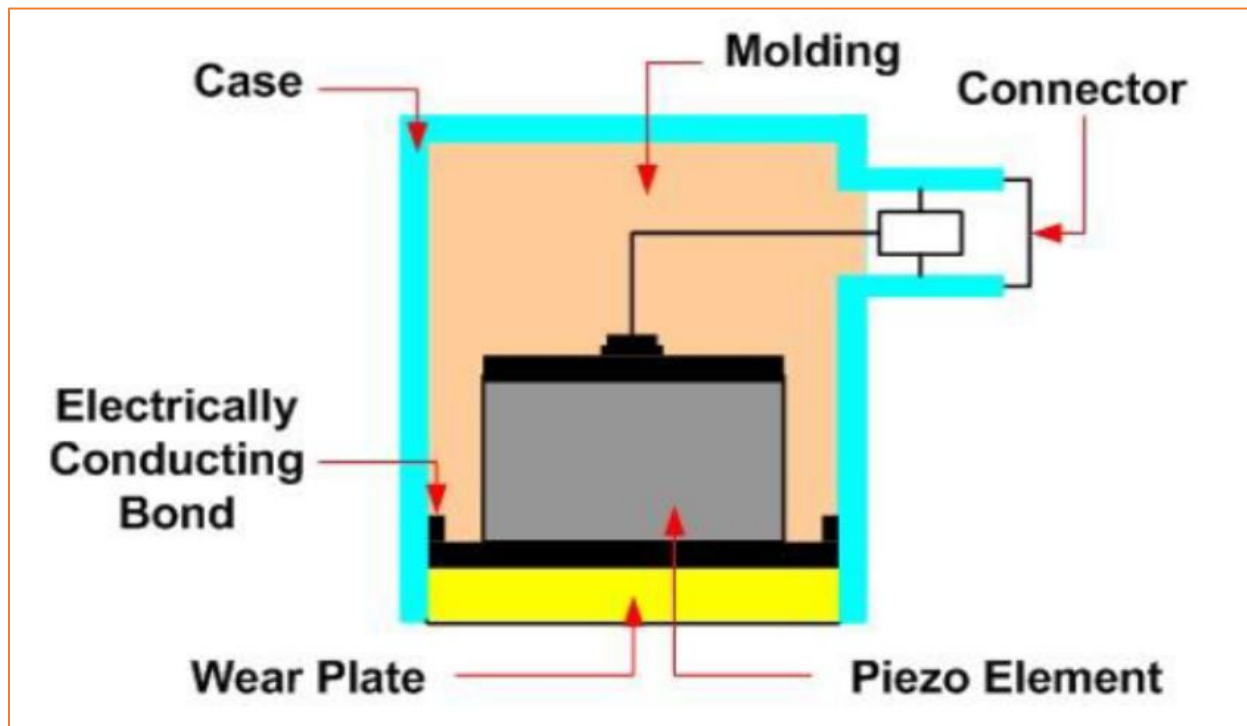


Figure 2. 11: Typical Acoustic Emission Sensor [80]

2.6.3 Piezoelectric Material Size Effects

An ideal sensor is closely typified by a nanoscale piezoelectric material with numerous electrode sets planted in a sample. Scaling up the piezoelectric material to a convenient size brings about some deviation from ideality. The enhanced performance of piezoelectric materials with reduction in size is attributed to the increased surface to volume ratio of the material. The increased surface to volume ratio subsequently leads to lateral direction relaxation of the surface atoms [83]. Resonance and strain averaging are critical consequences of the piezoelectric dimensions.

Resonance frequency is the frequency at which the piezoelectric material efficiently converts mechanical energy into electrical energy. At this frequency, the sensor gives maximum output. The resonant frequency for piezoelectric sensors takes place when piezoelectric material thickness is one-half wavelength [78]. The resonant frequency as a function of material thickness is expressed by equation (2.4).

$$d = (2n - 1)\lambda/2 \quad (2.4)$$

Where d = thickness of piezoelectric material

n = odd or even number

And λ = signal wavelength

The acoustic emission signal will give no output when

$$d = n\lambda \quad (2.5)$$

2.6.4 Piezoelectric Sensor Couplants

At atomic level, the contact surfaces between the acoustic sensor and the workpiece are imperfect, making contact only on distinct points. Placing a piezoelectric sensor directly on specimen surface produces a weak signal which can be enhanced by application of a thin fluid couplant that provides better contact between the sensor and material surface. The absence of a couplant makes the force transmitting area small; and a couplant fills the small gaps to ensure uniform pressure transmission between surfaces [84]. Numerous couplants have been in use and the choice is determined by the conditions of application as shown in Table 2.7.

Table 2. 6: Acoustic Emission Couplants [85]

Couplant	Approximate Temperature Range
Dow Corning V-9 Resin	~ -40° C to 100° C
High Vacuum Stop Cock Grease	~ -40° C to 200° C

Ultrasonic Couplants	Room Temperature
Petroleum Grease	Room Temperature
Dow Corning 200 Fluid	-273° C to -70° C and -30° C to 200° C
Dental Cement	~ 0° C to ~50° C
50 % Indium – 50 % Gallium mixture	~20° C to 700° C
GE Silicone II	5° C to 200° C

2.6.5 Piezotron Coupler

The two purposes of the Piezotron coupler are the provision of power to the sensor and signal conditioning of the high frequency sound signal from the Piezotron sensor. It contains a built-in RMS converter with plug-in modules for signal filtration, gain applications and integration time constant. The gain module amplifies the signal by a predefined factor and is connected to a series connection of two high-pass or low-pass filters. The two filters can be combined to form a band pass filter [86].

The bandpass filtered signal frequency is amplified and combined with the integration time constant to form a high frequency envelop. The optocoupler monitors that the level of the RMS frequency does not exceed a predefined value. Once the predefined value is exceeded, the optocoupler triggers the limit switch to shut. That ensures the removal of baseline noise and transmission of high frequency peaks. The optocoupler schematic diagram is shown in Figure 2.12.

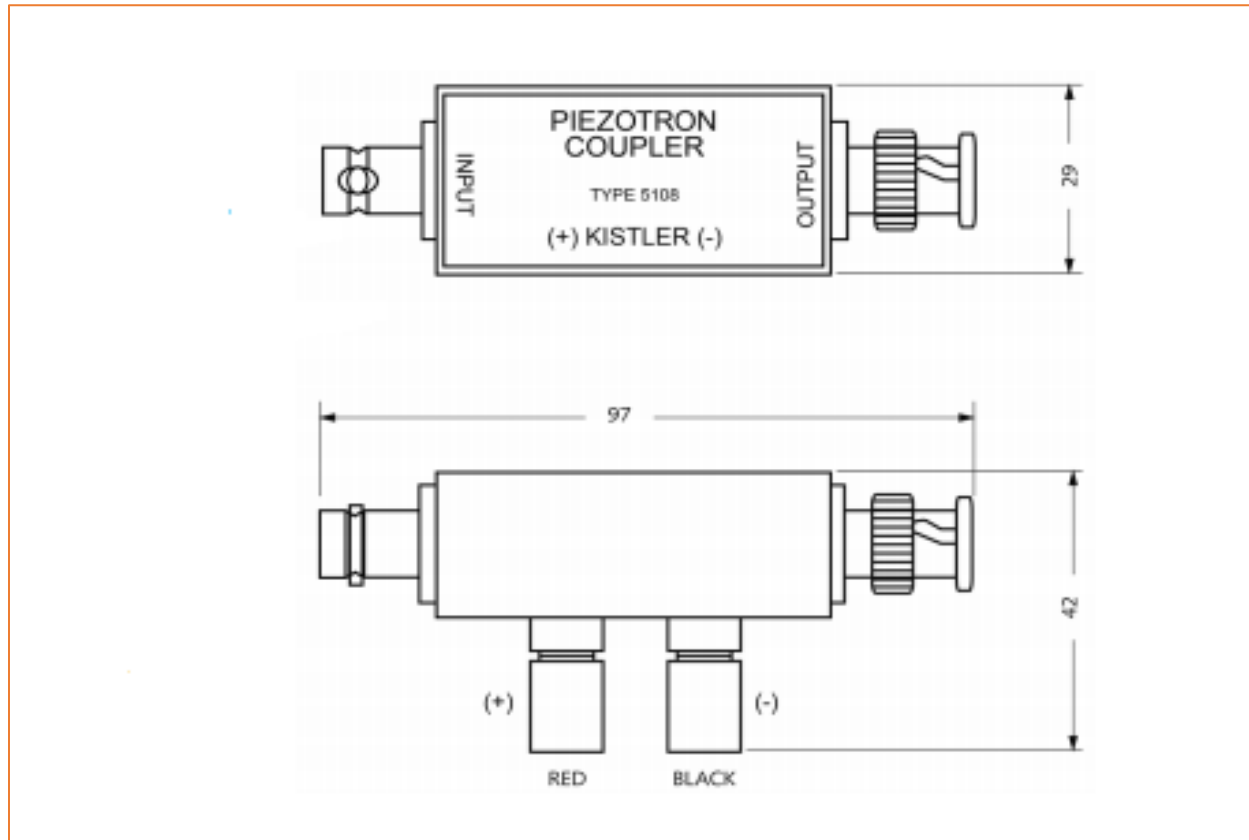


Figure 2. 12: Kistler Piezotron Coupler [87]

2.6.6 Temperature Dependency of Piezoelectricity

When ferroelectric materials are subjected to temperatures above the Curie temperature, they transform into another material form with reduced performance and devoid of piezoelectric properties. It is thus a requirement that piezoelectric materials be used at temperatures lower than the Curie temperature to preserve their poling stability. Sensor selection must be based on temperature restriction provided by the manufacturer; ensuring that the Curie temperature is not exceeded. Even after proper sensor selection, temperature monitoring is vital for dynamic heat generating applications. On the other extreme, using a piezoelectric sensor at cryogenic temperatures reduces the mechanical and electrical properties of piezoelectric sensors. The following are consequences of using the sensor in cryogenic temperatures: reduced electrical

capacitance, reduced loss factor, reduced strain coefficient and magnified coercive field [88]. Temperature changes result in acoustic piezoelectric sensor noise, which alters the actual signal. It is essential that the sensor attains thermal equilibrium before use at different temperatures.

2.6.7 Sensor Sensitivity

2.6.7.1 Effect of Cables

Sensor sensitivity is a composite of piezoelectric material and auxiliary components properties. Components such as electrical cables used in conjunction with the sensor play an integral role in sensor sensitivity determination. Signals are transmitted in the form of high frequency AC signals. Circuit capacitive reactance caused by cable capacitance distorts AE signals. It was discovered that a cable less than 30 meters in length between power supply and piezoelectric sensor has negligible capacitance effects on data signals [89]. The effect of cable length on sensitivity is best illustrated by equation (2.6).

$$V_o(S) = Q(S)/C_o \quad (2.6)$$

where V_o = sensor open circuit voltage;

Q = charge produced by a strain S ,

and C_o = capacitance of the sensor.

Connecting the sensor to the amplifier through cable will only increase the total circuit capacitance as illustrated by equation (2.7). It is evident that the supply voltage is inversely proportional to the total capacitance, mainly due to cable length. As such it is recommended that the minimum cable length possible be used to minimize output signal distortions due to additional cable capacitance.

$$V(S) = Q(S)/(C_o + C_c + C_I) \quad (2.7)$$

where C_c = cable capacitance

and C_I = input capacitance of the preamplifier.

Another factor to consider in using cables in conjunction with sensors is the routing of the cables. Electromagnetic interference is a consequence of running cables along AC power lines and through electrostatic discharge areas [90]. Extra protection to the cable is achieved through provision of a separate grounded conduit to eliminate undesirable noise. Sensor manufacturer's recommended cable type and length must be used always to obtain best results.

2.6.7.2 Effect of Preamplifier Noise

Sensor spectral response to an acoustic signal relies upon the preamplifier input characteristics, hence, use must be made of preamplifiers that are meant for acoustic emission. Current variations in the leading amplification device cause noise in shorted preamplifier. For unshorted inputs, the noise is attributed to current variations in the input resistor [91]. The root mean square noise voltage for the resistor is expressed as:

$$V_n^2 = 4KTR\Delta\nu \quad (2.8)$$

where K = Boltzmann's constant,

T = temperature,

R = resistance

And $\Delta\nu$ = preamplifier bandwidth.

In the case of an open input stage preamplifier without a connected sensor, R represents the stage input resistance, otherwise R is an equivalent resistance. Higher noise frequencies are suppressed by cable and sensor capacitances. The manufacturer specifies the amplifier noise level as the ratio of root mean square voltage to gain as indicated in the following equation.

$$V_s = V_o/G \quad (2.9)$$

The range for most acoustic emission sensors impedance is 50-1000 Ω and is expressed as:

$$V_n^2 = 0.004\sqrt{Z_o}\Delta\nu \quad (2.10)$$

where Z_o = sensor impedance (K Ω)

$\Delta\nu$ = preamplifier bandwidth (Hz)

The exact preamplifier-sensor-cable combination noise voltage is expressed as:

$$V_{noise} = \sqrt{V_s^2 + V_n^2} \quad (2.11)$$

A root mean square voltmeter can be used to measure the noise voltage.

2.6.8 Sensor Calibration

Sensor accuracy and system integrity are guaranteed by a periodic sensitivity audit within the operating spectrum of frequencies and amplitudes [92]. Accessibility of the sensor is a factor to be considered in immovable sensor installation to ensure that calibration can be performed easily. The recommended general sensor calibration interval, the associated calibration sensitivity curves and all calibration guidelines are provided by the manufacturer. The good news about Kistler piezoelectric sensors is that they are factory calibrated and come with a calibration certificate traceable to national standards. Calibration is also offered at customer request for immovable sensors.

The Kistler sensor sensitivity units are $\text{dB}_{\text{ref}} \text{ 1V}/(\text{m/s})$. This research utilizes a Kistler piezoelectric acoustic sensor which can detect surface (Rayleigh) and longitudinal waves within the frequency range 50kHz-900kHz [93]. Either of the two waves can be used to calibrate the piezoelectric sensor. Technical Data on the Kistler acoustic emission sensor is provided in Appendix A. During the piezoelectric sensor calibration process, comparison is made between the output spectrum of the sensor of interest and that of a standard reference sensor. In the event of a deviation from the standard, adjustments must be made on the sensor of interest. The custodian of international physical measurement standards is the International Bureau of Weights and Measures. The headquarters are in Sèvres, France [94].

2.6.9 Acoustic Emission Signal Parameters

Since an acoustic emission signal is a composite of numerous parameters, as much information as possible must be captured during the data acquisition stage. Among the sea of parameters contained in the AE pre-processed signal are amplitude, counts, Measured Area Under Rectified Signal Envelop (MARSE), duration and rise time [95]. Figure 2.13 is a diagrammatic representation of these features.

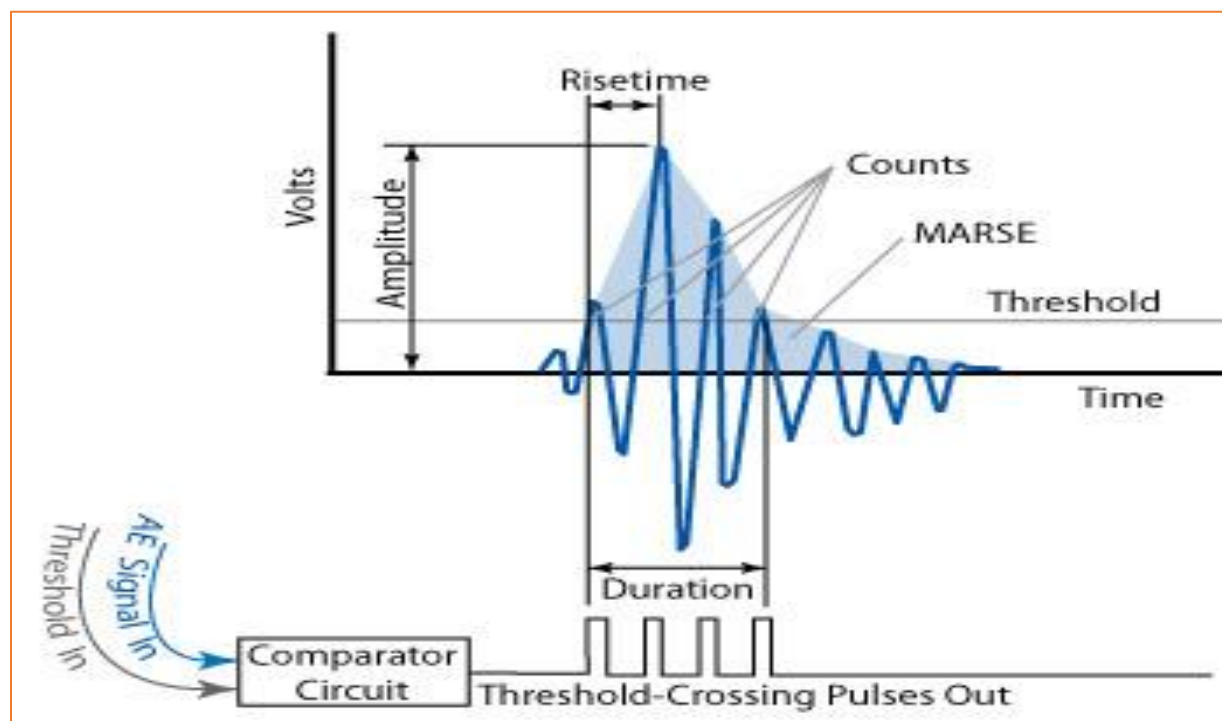


Figure 2. 13: AE Signal Features [96]

Amplitude is an important parameter as it determines whether a signal will be detected or not. It is defined as the peak voltage in a waveform. The unit of expression of amplitude is the decibel (dB). Detectability of a signal below the operator defined threshold value is unattainable. The unit for Rise time is the second (s). It is defined as the time gap between the first threshold crossing

and signal amplitude. Rise time provides valuable information about the signal propagation from the source to the sensor, hence it can aid during signal filtering stage. The Duration of an AE signal is expressed in seconds (s). It is the interval between the first and last threshold crossings of a signal. This parameter is fundamental in the identification of different source types and can be instrumental in signal filtering. Duration is dependent on signal strength and type of material.

The alternative name for MARSE is energy counts. It is defined as a measure of the area under blanket of the rectified linear voltage time signal from the sensor. The MARSE allows the calculation of the energy emitted by the source, provided the signal is above the user defined threshold. Counts refers to the number of pulses discharged by the measurement circuitry. Usually, the parameter is coupled with other parameters such as amplitude and duration for meaningful information to be deducted from the signal form. Acoustic emission RMS is defined as the square root of the mean of the squares of AE hits amplitude [97]. Acoustic Emission root mean square (AE_{rms}) is represented by equation (2.12):

$$AE_{rms} = \sqrt{\frac{1}{\Delta T} \int_0^{\Delta T} AE^2(t) dt} = \sqrt{\frac{1}{N} \sum_{i=1}^N AE^2(i)} \quad (2.12)$$

Where ΔT = integration time constant

N = number of discrete AE data within ΔT

2.6.10 Acoustic Emission Wave Propagation Effects

The acoustic emission wave suffers many effects during its propagation from the source to the sensor. The effects on the AE waveform include attenuation, dispersion, diffraction and scattering. The AE waveform detected by a sensor is much more complex in form compared to the AE at source. It is shaped by the propagation effects between the source and sensor. The important factors of wave propagation for AE are wave modes and wave velocity, wave reflection, mode conversion and attenuation.

The popular modes of wave propagation are dilatational, shear, surface, plate, interfacial, Love and creeping. The primary basis for classification of wave modes is the direction of oscillation of media particles. On that basis, a longitudinal wave is one in which media particles vibrate in the direction of the wave propagation while a transverse wave has media particles vibrating perpendicular to wave propagation. The media particles in a surface wave vibrate in an elliptic fashion while plate wave particles vibrate vertical to the plate surface. The speed of each wave mode is dependent on the material properties of the media.

Because of attenuation, there is a gradual decrease in AE wave intensity from the source to the detection point. The three causes of attenuation are geometric spreading, material damping and wave scattering. As a wave traverses in a medium, there is conversion of kinetic energy into heat energy. Some of the energy is reflected by structural boundaries within the medium. An instrument called a Hsu-Nielson Source is used to measure the effects of attenuation on an AE signal [96].

2.6.11 A comparison of the AE technique and other NDT Methods

Like any other method of surface roughness monitoring, AE monitoring method has both advantages and disadvantages. Iwata and Morivalci [98] pointed out that due to the large difference in frequency ranges between signal and noise, it is easy to filter the signal to obtain a better signal to noise ratio. Acoustic emission monitoring method does not require modification of existing system. The emission of signal during the machining process occurs in real time, thereby allowing monitoring to be carried out in real time as well [99]. Unlike in other non-destructive monitoring techniques such as ultrasonic sensing where signal are externally sourced, AE signal is internally sourced [100].

Due to the randomness of the acoustic emission signal process, the analysis and interpretation of the emitted signal is complex. The complexity is worsened by the non-periodicity and numerous signals associated with the signal, rendering mathematical relationships unsuitable in describing them. Some of the differences between AE techniques and other NDT methods are illustrated in Table 2.7.

Table 2. 7: Comparison of AE characteristics with other NDT methods [101]

Acoustic Emission	Other NDT Methods
Requires stress	Do not require stress
Each loading is unique	Inspection is directly repeatable
More material sensitive	Less material sensitive
Less geometry sensitive	More geometry sensitive
Less intrusive on plant process	More intrusive on plant process
Requires access only at sensors	Requires access to whole area of inspection
Main problems noise related	Main problems geometry related

2.6.12 Acoustic Emission Signal Correction and Pre-processing

Since an Acoustic Emission Signal is a composite of super-imposed momentary features, it is essential to process it to abstract parameters of significance. There are myriads of signal processing methods in use for the analysis of AE signals. The abstracted features are valuable for testing or monitoring purposes. The preeminent methods for signal analysis are time series analysis, Fast Fourier Transform (FFT), Gabor transform (or window (local) Fourier transform), Wigner–Ville distribution, and wavelet transform. For this research, only the FFT method will be discussed.

There is urgency to modify an Acoustic Emission signal into a mode that mirrors all the significant parameters embedded within. Examples of such parameters are frequency, amplitude and other sources of distortion. The modification process embroils filtering out electrical noise with the aid of a signal processing tool such as Fast Fourier Transform (FFT). The raw signal is vague, containing both the necessary and undesirable parameters fused together. There are various approaches to enumerate the Discrete Fourier Transform (DFT) of a signal. The FFT approach has the convenience of significantly shortening enumeration time.

The leading step in FFT signal analysis is the selection of the primary DFT equation:

$$X_p = \sum_{n=0}^{N-1} x_n e^{-j\frac{2\pi}{N}np} \quad (2.13)$$

Separating Eq. (2.13) into odd and even components:

$$X_p = \sum_{n=0}^{\frac{N}{2}-1} x_{2n} e^{-j\frac{2\pi}{N}(2n)p} + \sum_{n=0}^{\frac{N}{2}-1} x_{2n+1} e^{-j\frac{2\pi}{N}(2n+1)p} \quad (2.14)$$

$$= \sum_{n=0}^{\frac{N}{2}-1} x_{2n} e^{-j\frac{4\pi}{N}np} + e^{-j\frac{2\pi}{N}p} \sum_{n=0}^{\frac{N}{2}-1} x_{2n+1} e^{-j\frac{4\pi}{N}np} \quad (2.15)$$

$$= A_p + W^p B_p \quad (2.16)$$

Where

$$A_p = \sum_{n=0}^{\frac{N}{2}-1} x_{2n} e^{-j\frac{4\pi}{N}np}; \quad (2.17)$$

$$B_p = \sum_{n=0}^{\frac{N}{2}-1} x_{2n+1} e^{-j\frac{4\pi}{N}np} \quad (2.18)$$

And

$$W = e^{-j\frac{2\pi}{N}}. \quad (2.19)$$

A_p and B_p are DFTs of length $\frac{N}{2}$ each:

$$A_p \text{ equals the sequence } \{x_{2n}\} = \{x_0, x_2, \dots, x_{N-4}, x_{N-2}\} \quad (2.20)$$

$$\text{And } B_p \text{ equals the sequence } \{x_{2n+1}\} = \{x_1, x_3, \dots, x_{N-3}, x_{N-1}\} \quad (2.21)$$

$$\int_{-\infty}^{\infty} \phi(x)(x+l)dx = \phi_{0,l} \quad (2.22)$$

2.7 Computational/Artificial Intelligence

Adaptive Neuro-Fuzzy Inference System (ANFIS) and Artificial Neural Network (ANN) are branches of Computational Intelligence in which the human brain is represented by computational models. ANFIS and ANN are the prediction methods used in this research. A comparison was made between the two prediction models to determine their accuracy in surface roughness determination. The computational models mimic the human brain in terms of learning capability and problem-solving approach. These brain attributes are the foundation of Computational Intelligence [102]. Computational Intelligence is an integration of technologies from various fields (see Figure 2.14). The two phases of Computational Intelligence development are simulation of human experience followed by rule-based conclusions and modelling using ANFIS and ANN. Neural networks can model parameters whose relationship is non-linear by checking for patterns in provided data. Both ANN and ANFIS are going to be described, but ANN will be explained first.

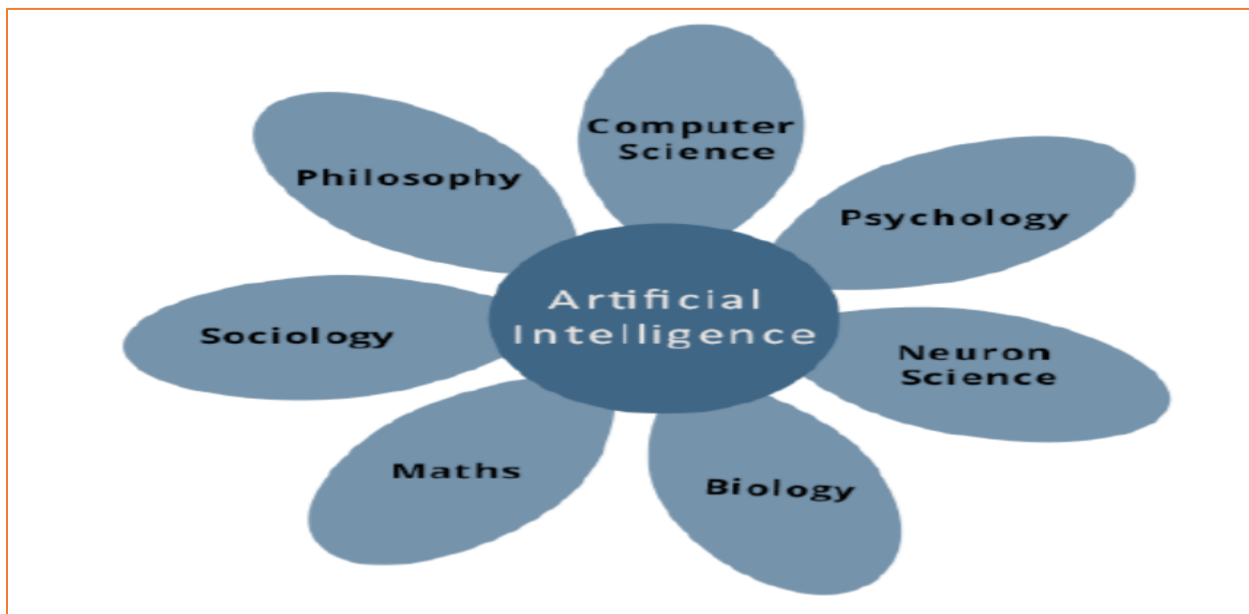


Figure 2. 14: Artificial Intelligence Disciplines [103]

A comparison is made between the conventional computing methods and soft computing methods as illustrated in Table 2.8.

Table 2. 8: Differences in approach between conventional computing and Soft Computing [104]

Characteristics	Conventional Computing	Soft Computing
Functions	By Rules	By example
Learning Method	Logically	Perceptual Pattern
Processing Style	Sequential	Parallel

2.7.1 Previous Applications of ANFIS and ANN in Surface Roughness Prediction

The complex nature of parameter interaction during the machining process has made researchers develop more efficient methods of surface roughness prediction. A survey of researches based on surface roughness prediction using computational intelligence reveals that ANFIS, ANN and genetic algorithms have been used. Among the three methods, ANFIS and ANN are commonly utilized.

Asiltürk and Çunkas [105] used a feed-forward ANN in surface roughness modeling and prediction turning operations on AISI 1040 steel. Dong and Wang [106] proposed an ANFIS model in end milling surface roughness prediction of 6061 aluminum alloy. A radial basis feed forward Artificial Neural Network was used by Munoz-Escalon and Maropoulos [107] in surface roughness prediction during face milling of Al 7075-T735. Calculation of Pearson correlation coefficients was done to ascertain input parameters correlation with surface roughness. The cutting parameters used are cutting speed, feed per tooth, axial depth of cut, chip's width and chip's thickness.

Jiao et al. [108] utilized an ANFIS model in predicting surface roughness of turned surface. A five-layered feed forward network was used in training the hybrid model. Many other researchers have implemented computational intelligence methods in surface roughness prediction of various materials during machining. A review of the researches reveals that the computational methods are more accurate than the regression model.

2.7.2 Fuzzy Modeling & Fuzzy Inference System

2.7.2.1 Boolean Logic vs Fuzzy Logic

The characteristics of a fuzzy event are vagueness and impreciseness. A fuzzy event cannot be classified as either true or false as it is a continuum between the two extreme values. In line with the above stated property, any value in the range 0 to 1 can be assumed by an event in fuzzy logic. The event value is called the truth value, which denotes the degree of membership of the event to the fuzzy set. A lower truth value closer to 0 represents a weaker degree of membership while a higher value closer to 1 represents a stronger degree of membership [109]. The value 0 denotes absolute falseness while a 1 denotes absolute truthfulness.

The best way to solve impreciseness in real everyday problems is using fuzzy logic systems. For example, considering the condition “add cold water” in a washing machine, for a human brain it is easy to understand the meaning of the statement. It is a different story when the task must be executed by a computer as it does not know which temperature value is considered as being cold. Cold can be any temperature value from 0° C to maybe 32° C. If a limit is given of the maximum temperature to be taken as cold, for example 32°C, any temperature above that such as 32.1° C is taken as hot. Such uncertainties are best solved by fuzzy logic systems. Fuzzy control has the advantage that no detailed plant mathematical model is required as the operator and designer experiences are embedded into the fuzzy controller [110]. Figure 2.15 shows the differences between a fuzzy logic system and Boolean logic.

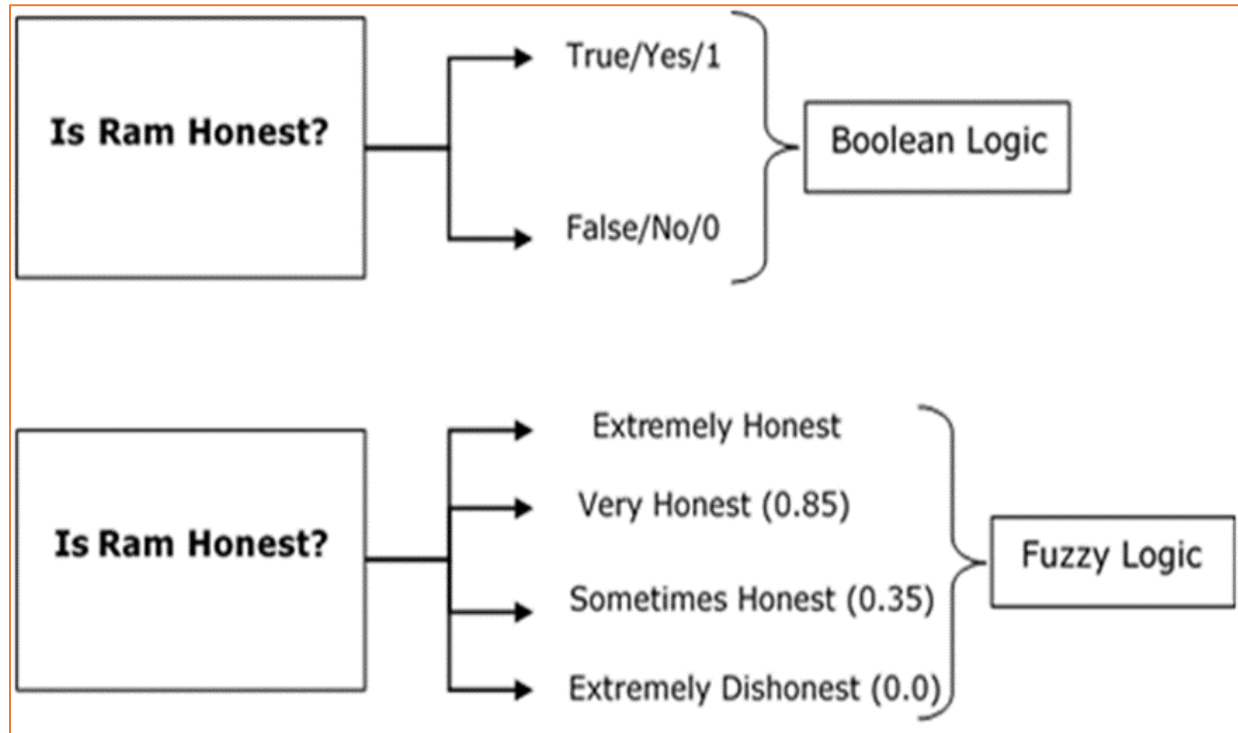


Figure 2. 15: Differences between Boolean Logic and Fuzzy Logic [103]

2.7.2.2 Fuzzy Set Theory

In 1965, Lotfi Zadeh [111] introduced a mathematical model called fuzzy set theory to represent linguistic vagueness. Since its introduction, the fuzzy set theory has evolved and advanced greatly. Most of the available conventional modelling tools available are crisp and precise in nature. Crisp statements are either true or false and nothing in between, that is, an element either belongs to a set or it does not belong. The fuzzy set theory differs from classical theory in terms of element membership. While classical set theory membership is crisp, fuzzy set theory membership takes a range of values between 0 and 1 [112]. The fuzzy set theory resembles the biological brain when dealing with vague data. Conventional models of problem solving require understanding of all variables at play. Due to the complexity of real-life problems, it is nearly impossible to know all variables at play. Fuzzy modelling is simplified by putting together numerous parameters. Figure 2.16 represents a crisp set and fuzzy set respectively.

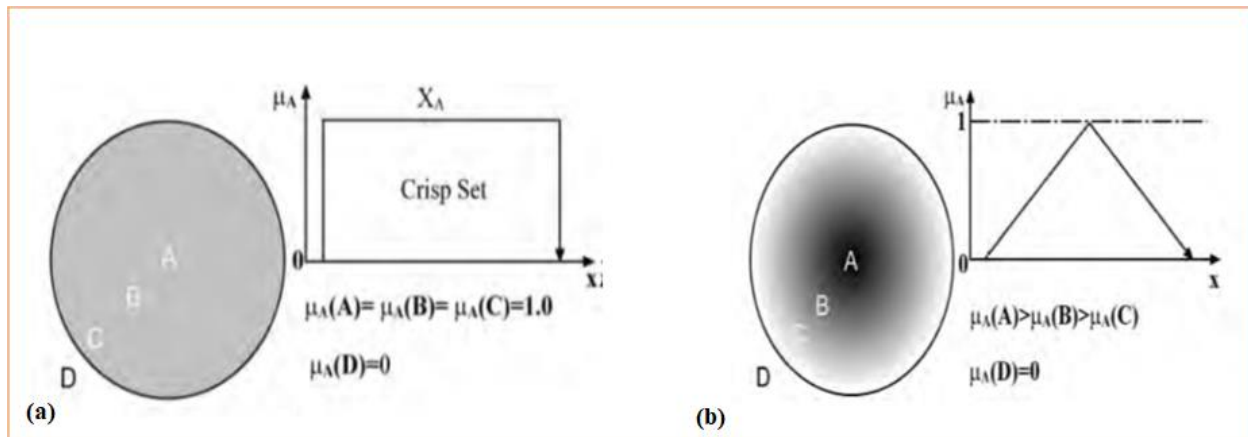


Figure 2. 16: (a) Crisp Set and (b) Fuzzy Set [113]

Linguistic variables like small, tall, large, low, fast, medium, slow, high and heavy are represented by fuzzy sets. In fuzzy set theory, it is possible for an element to belong to more than one set at a time. A fuzzy set A in its field of discourse, U , is represented as a set of ordered pairs. A pair is composed of a variable x and its associated degree of membership as shown by equation (2.23). A diagrammatic representation of the mapping of each variable to its associated degree of membership is known as a membership function [114].

$$S = \{(x, \mu(x)) \mid x \in U\} \quad (2.23)$$

2.7.2.3 Fuzzy Inference Systems

The primary function of a Fuzzy Inference System is decision making. To accomplish this goal, it makes use of the “IF...THEN” rules together with connectors “OR” or “AND”. A Fuzzy Inference System (FIS) contains the fuzzy reasoning process. A complete FIS has three stages from data input to the desired output. These three stages in their order are fuzzification, rule evaluation and defuzzification. A detailed system on how the process works is shown in Figure 2.17.

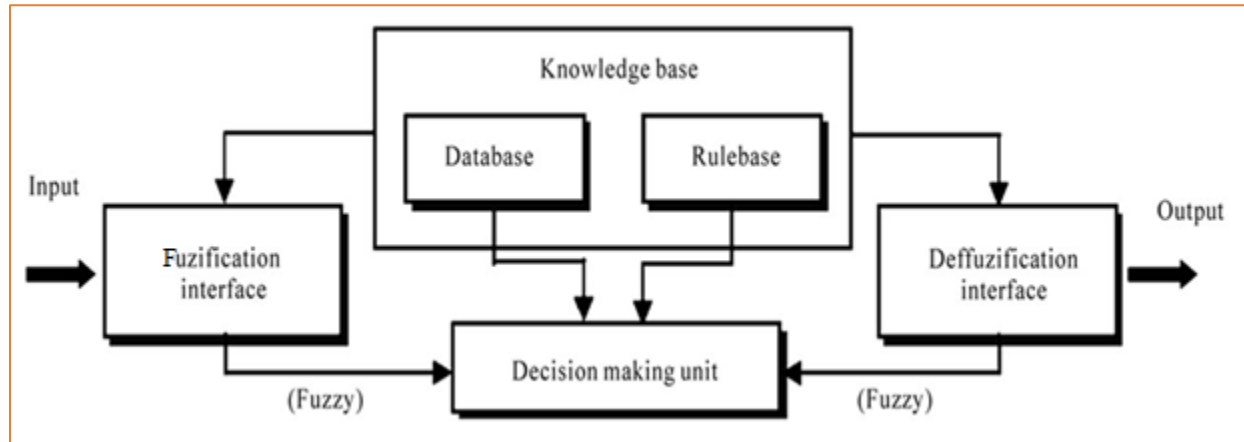


Figure 2. 17: Fuzzy Inferencing Unit [115]

2.7.2.4 Fuzzification

The first stage of the Fuzzy Inference System is called Fuzzification. At this stage crisp quantities are converted to fuzzy quantities. Sensors are used to determine everyday classical variables such as temperature, pressure and speed. These variables must be converted to fuzzy variables before they can be processed by a Fuzzy Inference system. During the fuzzification stage, every input is assigned its own group of Membership Functions (MF) to which it is converted. The universe of discourse is represented by the horizontal axis in the plot of input variable against degree of membership and all membership functions and crisp input values are contained within [116]. Figure 2.18 is a representation of membership function shapes for crisp inputs within the universe of discourse.

The shape and labelling of the input variables membership functions to be used must be chosen prior to coming up with the membership function number during the design process. In selecting the membership function shape, accuracy of the output, ease of use and economics of computer resources must be considered. Knowledge of the number of regions into which the universe of discourse must be partitioned helps in the determination of membership function numbers. The number of labels corresponds to the number of membership functions and each label represents a region [117].

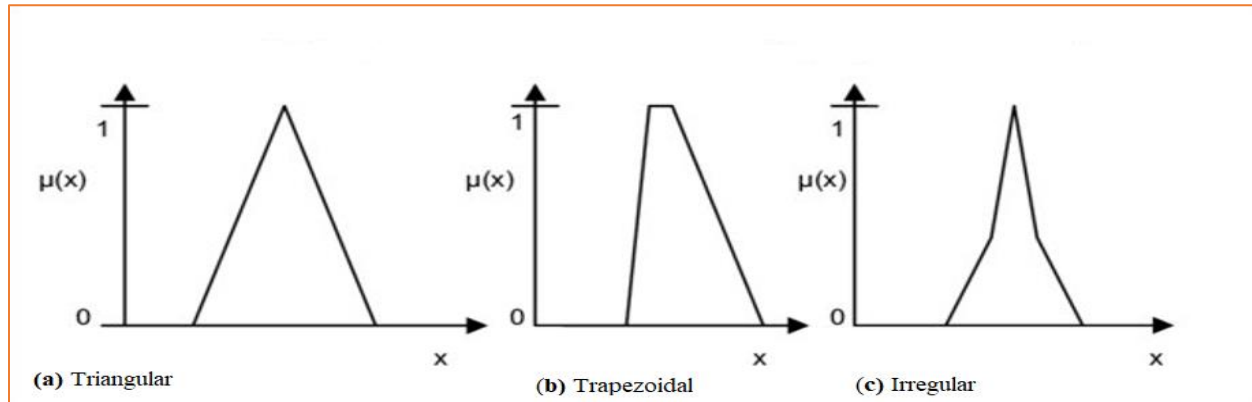


Figure 2. 18: Membership function shapes [118]

Experience is a very integral factor in choosing the Membership Function (MF) shape and number. The membership function shape used must be accurate and the number of the membership functions must not be too few or too many. Using too few membership functions causes slow output response and system oscillation while too many MFs reduce system stability and misfiring. The membership functions must overlap so as to avoid the system being reduced into a Boolean logic system [119]. The input must not belong to more than two membership functions and the overlapping membership function grades must add up to not more than 1. The membership functions must not cross each other at the maximum truth value.

At this stage, each crisp input value and intersection point within the universe of discourse is mapped with each membership function and transposed onto the μ axis. The degrees of truth are the ones represented by the μ values. The μ values are related to each label as fuzzy inputs. The results from this stage are carried to the rule evaluation stage in the fuzzy inference system process.

2.7.2.5 Rule Evaluation

A series of IF-THEN statements constitute the Rule evaluation procedure. In the statement lies an operator popularly known as Zadeh operator. Experience and familiarity are required in rule determination at this stage of Fuzzy Inference System. In this thesis, such experience was gained

using previously obtained turning data in literature. The syntax for the rules used is strict and it is structured as follows:

IF (input1(X1) is membership function1) ZADEH OPERATOR (input2 (X2) is membership function2)THEN (output (Y1) is output membership function)

X and Y represent antecedent and consequent respectively.

The three types of Zadeh operators used are AND, OR and NOT. The output membership function is influenced by the linguistic variable used. The Zadeh operator can afford a maximum of two membership functions. There is a similarity between Boolean operators and Zadeh operators such that:

In fuzzy logic: $X1 \text{ AND } X2 = \min (X1, X2)$. The relationship is represented by equation (2.24).

$$\mu_{A \cap B} = \min [\mu_A (X1), \mu_B (X2)] \quad (2.24)$$

In fuzzy logic: $X1 \text{ OR } X2 = \max (X1, X2)$. The relationship is represented by equation (2.25).

$$\mu_{A \cup B} = \max [\mu_A (X1), \mu_B (X2)] \quad (2.25)$$

In fuzzy logic: The opposite of the set is represented by NOT as represented by equation (2.26).

$$(\mu_A)^- = [1 - \mu_A (X)] \quad (2.26)$$

The above equations give the rule strengths from the interfacing of input antecedents X1 and X2 and the resulting strengths values are called fuzzy outputs.

2.7.2.6 Defuzzification

The defuzzification stage is the third and final stage of the fuzzy inference system. At this stage, the conversion of fuzzy outputs into crisp outputs takes place. In fuzzy logic controllers, the crisp value represents the action to be taken in process control. The numerous defuzzification methods

include the Center of Gravity Method (COG), Center of Sums Method (COS), Center of Area or Bisector of Area Method (BOA), Weighted Average Method and Maxima Method [120].

The factors that must be considered in selecting the defuzzification technique in each application are suitability of the design, the efficiency of the technique, continuity of defuzzification result and compatibility with fuzzy system. Continuity of defuzzification result means that small changes in membership values of the fuzzy output must give rise to small changes in crisp result. This principle is particularly important in fuzzy logic controllers. Computational efficiency is determined by the nature and number of computations carried out to arrive at the defuzzification result [121].

For the purposes of this research, only the Center of Gravity method shall be discussed. This method utilizes fuzzy set centroid to calculate the crisp output value. The first stage is the division of the total membership function area into sub-divisions. Each sub-division has its area and centroid calculated. To simplify calculations in the microcontroller, a restriction is put on the output membership functions to singletons. The result of this stage is crisp, and it is passed out of the FIS for processing elsewhere. The crisp value is given by equation (2.27).

$$X = \frac{\sum_{i=1}^n x_i \cdot \mu(x_i)}{\sum_{i=1}^n \mu(x_i)} \quad (2.27)$$

Where

x_i = sample element.

$\mu(x_i)$ = membership function.

n = number of elements in the membership function.

2.7.2.7 Mamdani-Type FIS VS. Sugeno-Type FIS

When dealing with expert knowledge, the Mamdani method is better accepted as it gives the allowance for expertise description in a human-like way. Mamdani-type FIS finds most of its applications in decision support. On the other hand, it works better for dynamic non-linear systems control where optimization and adaptive methods must be employed. The most notable difference between Mamdani-type FIS and Sugeno-type FIS stems from the conversion of fuzzy inputs into

crisp outputs. The weighted average method is used for crisp out computation in Sugeno-type FIS while the Mamdani-type FIS employs the defuzzification technique [122]. The Sugeno-type FIS has greater processing speed as the time consuming defuzzification process is replaced by the efficient weighted average method. The Sugeno-type FIS has linear or constant membership functions while the membership functions for Mamdani-type FIS are in the form of fuzzy sets [123].

2.7.3 Artificial Neural Networks

The birth and growth of Artificial Neural Networks is inspired by the amazing way in which the human brain operates. Unlike the typical computers, the human brain does not need coding for it to solve complex problems. It learns and can adjust to solve problems from experience gained from similar previously encountered problems. The inability of modern computers to learn, coupled with the fact that not all real-life problems can be expressed in code form, has inspired researchers to come up with models that emulate the biological nervous system [124].

The human brain's massive cognitive efficiency is attributed to its basic part called a neuron which acts as a biological switch in the nervous system. The neuron collects, processes and transmits signals in the form of electrical impulses [125]. The feature responsible for information reception on the neuron is called a dendrite and is indicated on the neuron structure diagram in Figure 2.19. Received signals accumulate in the nucleus until a threshold value is attained, after which the signal is transmitted to adjacent neurons through the axon. Signal effect on a neuron is dependent on the weight of the synapse.

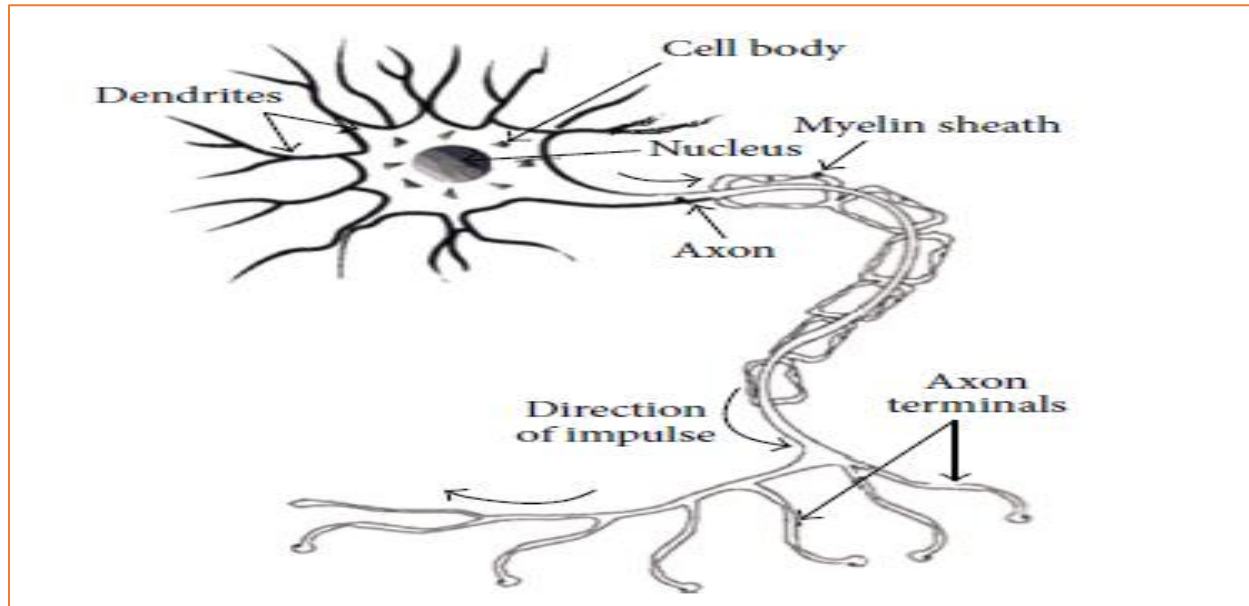


Figure 2. 19: Biological Neuron Structure [126]

The mathematical neuron model was born out of the researchers' push for low energy consumption computational tools capable of learning and performing distributed computation with high input noise tolerance. Artificial neurons are represented as nodes in Artificial Neural Networks. A signal traverses the network through a layered assemblage of nodes, with the signal being transformed at each layer. The layers of nodes between the input and output are called hidden layers. Artificial Neural networks have the competence to alter the weights based on the form of input data received. The mathematical model of a neuron is shown in Figure 2.20.

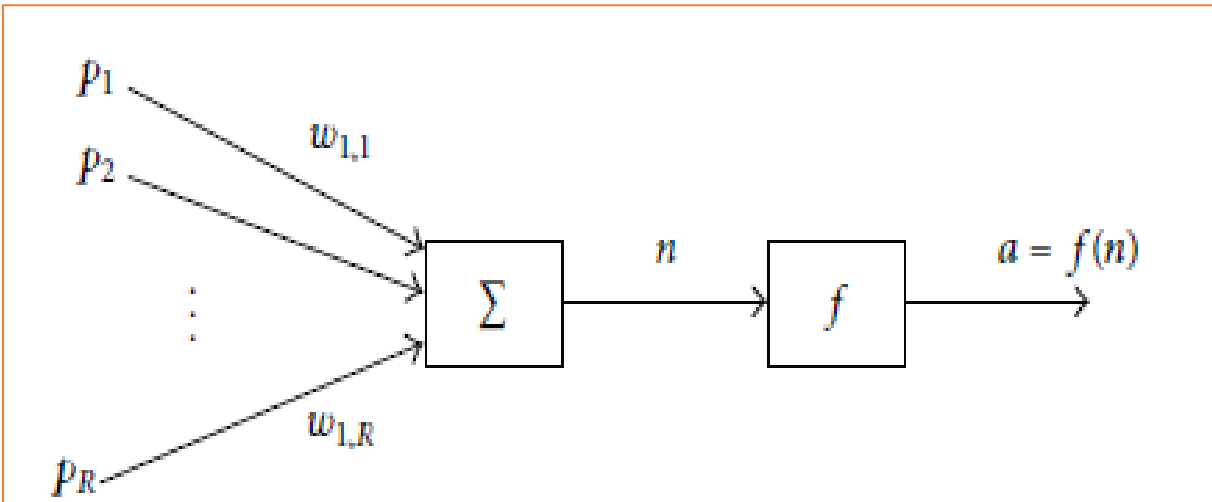


Figure 2. 20: Mathematical Model of a Neuron [126]

2.7.3.1 Neural Network Architecture

Architecture refers to the arrangement and connection pattern of nodes. Based on the inter-connection of nodes, there exist two main groups of Artificial Neural Networks:

- Feed-forward networks
- Feed-back networks

2.7.3.1.1 Feed-Forward Artificial Neural Networks

In Feed-Forward Artificial Neural Networks, the nodes are connected in one direction from the input towards the output. A neuron in a preceding layer is connected to every other neuron in the next layer [127]. In this architecture type, no output is fed back to the network (see Figure 2.21). This is the most common of the two architectures. Feed-Forward Artificial Neural Networks have applications in pattern generation, recognition (character recognition) and classification (customer data bases) [128].

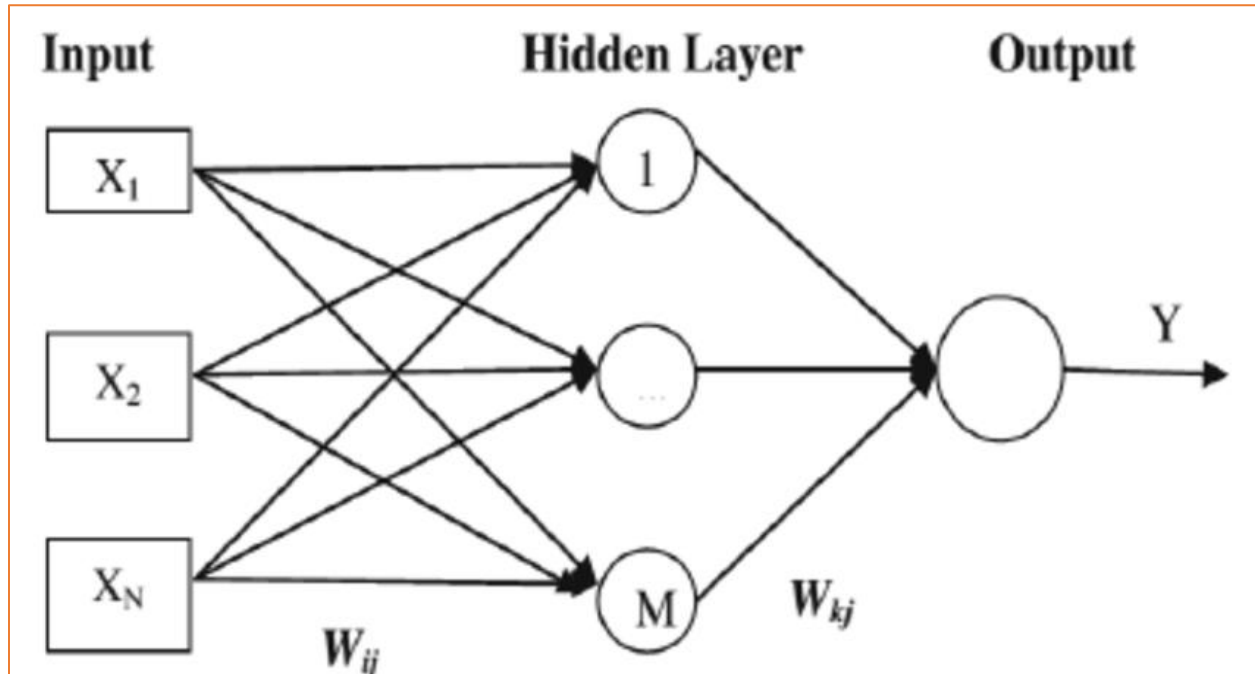


Figure 2. 21: Feed-forward Artificial Neural Network [129]

Figure 2.21 shows a one-layer Feed-forward Neural Network with the following parameters:

$$\text{Number of inputs} = n$$

$$\text{Number of outputs} = m$$

The output and input vectors are respectively expressed as

$$y = [y_1 \ y_2 \ \dots \ y_m]^t \quad (2.28)$$

$$x = [x_1 \ x_2 \ \dots \ x_n]^t \quad (2.29)$$

Each input neuron has a weight associated with it and from Figure 3, the activation value of neuron 1 is given as:

$$a_1 = w_{11}x_1 + w_{12}x_2 + \dots + w_{1n} \quad (2.30)$$

The activation value of the i th neuron can thus be written as:

$$a_i = \sum_{j=1}^n w_{ij} x_j \quad \text{for } i = 1, 2, \dots, m \quad (2.31)$$

The non-linear mapping due to transformation by each of the m neurons is expressed as:

$$y_i = f(w_i^t x), \text{ for } i = 1, 2, \dots, m \quad (2.32)$$

where w_i is defined as

$$w_i \triangleq [w_{i1} \ w_{i2} \ \dots \ w_{in}] \quad (2.33)$$

The input space is mapped to the output space by the following expression

$$y(t) = \Gamma[Px(t)] \quad (2.34)$$

Where W is the weight matrix given by

$$P \triangleq \begin{bmatrix} w_{11} & \dots & w_{1n} \\ \vdots & \ddots & \vdots \\ w_{m1} & \dots & w_{mn} \end{bmatrix} \quad (2.35)$$

2.7.3.1.2 Feed-back Artificial Neural Networks

Feedback artificial Neural Networks are also called recurrent networks. In feedback Artificial Neural Networks, weight adjustment information is fed back from the output layer to previous layers to reduce output error. It has applications in speech recognition [129]. Figure 2.22 shows the Artificial Neural Network architecture.

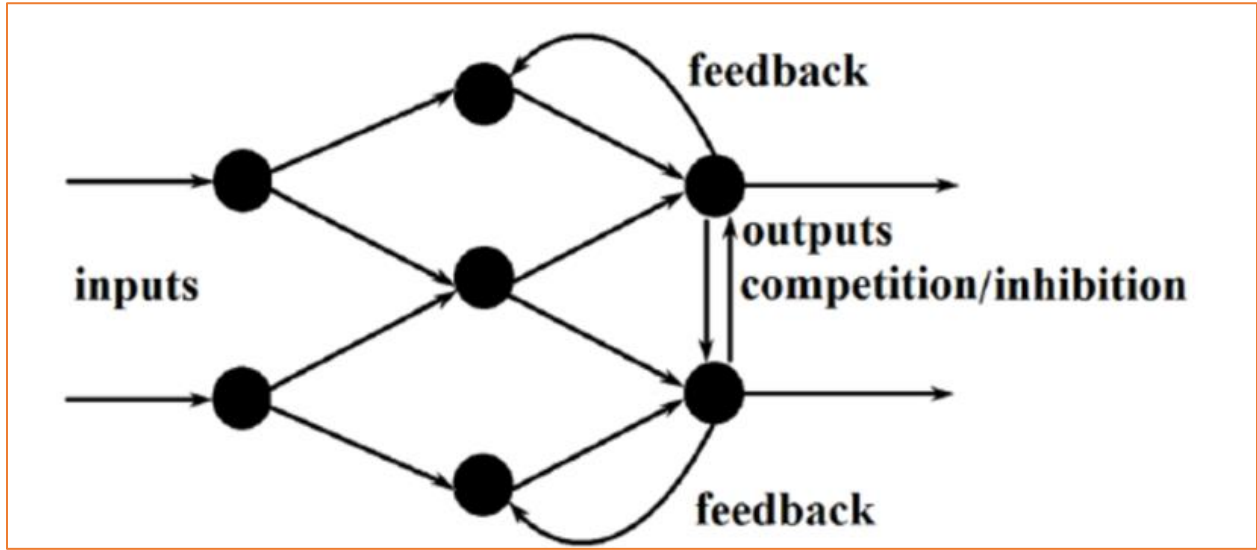


Figure 2. 22: Feedback Artificial Neural Network Architecture [130]

Output o_j controls o_i in the loop. The feedback loop delay elements introduce true delay between t and Δt . Using the feedforward notation,

$$o(t + \Delta) = \Gamma[w_0(t)] \tag{2.36}$$

represents $o(t)$ mapping to $o(t + \Delta)$.

Equation (2.36) is represented by the block diagram in Figure 2.23.

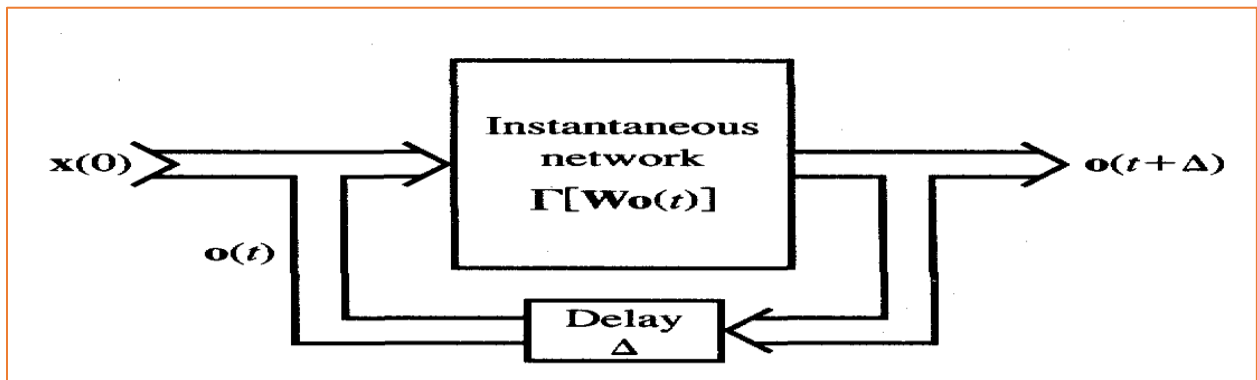


Figure 2. 23: Mapping Block Diagram [129]

2.7.3.2 Learning in Artificial Neural Networks

The capability of Artificial Neural Networks to learn is achieved by inter-neuron weighted connections. In real life, there are some problems that cannot be expressed in code. That is when learning algorithms come in handy. An example of such a problem is facial recognition. The different learning types for Artificial Neural Networks are:

2.7.3.2.1 Supervised Learning

During the learning process, both the input and the expected output are presented to the network. With the given sets of data, the system can compute resultant error from the difference between the expected output and actual output. The error is fed back into the system to adjust the weights on the neuron interconnections. The most commonly used rule in this category is the delta rule (Back Propagational Neural Networks). Learning occurs at each cycle that the system is presented with processing data. Each cycle is called an epoch. When a network is presented with data, it first makes a guess as to what it may be. It then uses the error to adjust the weights of the connections between nodes. Firstly, the network calculates the output based on equation (2.37):

$$output = f(input1 \times weight1 + input2 \times weight2 + \dots) \quad (2.37)$$

Or

$$O = f(\sum_{i=1}^n x_i w_i) \quad (2.38)$$

The error can now be found from the difference between the actual output and the target output:

$$error = target\ output - actual\ output \quad (2.39)$$

Or

$$e = t - o \quad (2.40)$$

The error is used to adjust the weights:

$$\text{weight change} = \text{learning rate} \times \text{error} \times \text{input} \quad (2.41)$$

Or

$$\Delta w = r \times e \times x \quad (2.42)$$

To ensure that only small changes are made to the weights on each iteration, a small learning rate (r) is applied. If the learning rate is too high the perceptron can jump too far and miss the solution, if it's too low, it can take an unreasonably long time to train. This gives a final weight update equation of:

$$\text{weight change} = \text{learning rate} \times (\text{target output} - \text{actual output}) \times \text{input} \quad (2.43)$$

Or

$$\Delta w = r(t - o)x_i \quad (2.44)$$

2.7.3.2.2 Unsupervised Learning

In this learning type, only input data set is provided to the network. The network must find a pattern between the provided data without any outside influence. This is the type of learning used in data mining applications such as finding user's preferences. This is achieved from analyzing the preferences of previous similar users.

2.7.3.2.3 Reinforcement Learning

A reward is offered to the network depending on how well it has performed. Reinforcement learning has a feedback mechanism like the supervised learning. Only one set of data is presented to the network and through trial and error, the system maximizes on the offered reward.

2.7.3.3 Artificial Neural Networks Learning Rules

A desirable feature of Artificial Neural Networks is their ability to learn from experience. The learning is achieved through variation of neural interconnection weights. The mechanism of

varying the weights is known as a learning rule. There are numerous Artificial Neural Network Learning Rules.

2.7.3.3.1 Hebbian Learning Rule

The Hebbian Learning rule was introduced by a neurophysiologist by the name Donald Hebb in 1949. It later developed to be an influential rule in soft computing. Following extensive study of neurons, Hebb established that repeated stimulation of a neuron by an adjacent neuron lowers the activation threshold. The rule states that “the connection between adjacent neurons is strengthened by simultaneous firing of the neurons” [131]. Feed-forward Neural Networks use this rule during the unsupervised learning process. The Hebbian learning rule is mathematically represented in Figure 2.24.

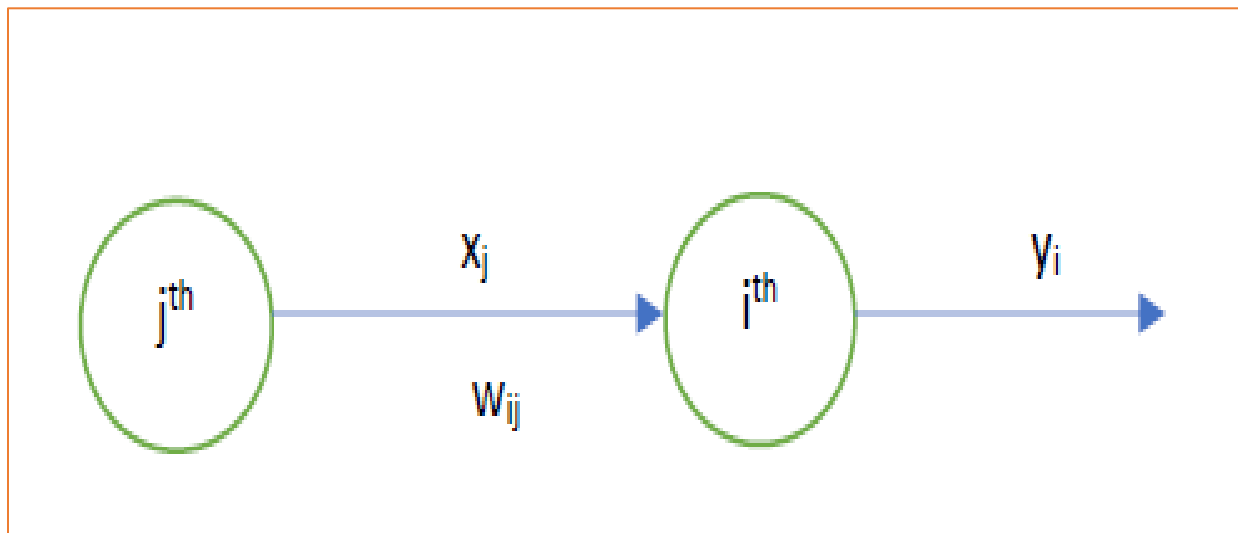


Figure 2. 24: Excitation effect of first node [131]

According to Hebb,

$$w_{ij} = \eta x_j y_i \quad (2.45)$$

Where w_{ij} = common weight when there is excitation from the j th to the i th node

X_j = activation of the j th node

Y_i = output to the i th node

η = step size weight control

2.7.3.3.2 Perceptron Learning Rule

The Perceptron Learning Rule was introduced by Rosenblatt. Its name is derived from the basic part of a neuron, the perceptron. The perceptron learning rule uses a linear classifier to categorize input data into two groups. Error correction is achieved by comparison of actual output and target output. Weights between adjacent nodes are adjusted based on identified error. The perceptron learning rule is used in single layer feed forward architecture networks. The operation principle of the perceptron learning rule is similar to the Hebb learning rule with the only difference being the absence of connection weights modification in the event of correct network response. In addition to weight adjustment, the rule also adjusts the threshold β [132].

$$\Delta\beta = \begin{cases} 0, & x \leq \beta \\ 1, & x > \beta \end{cases} \quad (2.46)$$

2.7.3.3.3 Delta Learning Rule (Widrow-Hoff Rule)

The Delta Learning Rule was introduced by Bernard Widrow and Marcian Hoff. This rule is also called the Least Mean Square Method. The Delta Learning Rule has a continuous activation function and falls within the supervised learning category. It compares the actual output to the desired output of the system and the error is calculated. The summation of the product of weight and input value gives the output node's activation. The Widrow-Hoff rule utilizes Gradient Descent learning. According to McClelland and Rumelhart [133], "error is minimized by modifying weights along the most direct path". Therefore, the first order derivative of error with respect to the weight is proportional to the negative change of the weight.

2.7.4 Adaptive Neuro-Fuzzy Inference Systems

2.7.4.1 Overview of Adaptive Neuro-Fuzzy Inference System

According to Jang [134], an Adaptive Neuro-Fuzzy Inference System is a hybrid of Artificial Neural Networks (ANN) and Fuzzy Inference Systems (FIS). Unlike in fuzzy logic systems where fuzzy rules are obtained from human expert knowledge, ANFIS automatically generates the fuzzy if then rules [135]. The use of human expert knowledge gets complicated in terms of time and number of rules to be generated, as the system to be modelled becomes bigger. ANFIS combines the advantages of both Fuzzy Logic systems and ANN. The two types of fuzzy inference systems are Sugeno-Takagi and Mamdani systems. The five data transformation stages of ANFIS are fuzzification, fuzzy operator application, application method, output aggregation and defuzzification.

2.7.4.2 ANFIS Architecture

An Adaptive Neuro-Fuzzy Inference System network is a multilayer network of interconnected adaptive nodes. The nodal outputs are dependent on the weights gained from previous experience. Error is minimized by modifying the weights as prescribed by the learning rules. The Takagi-Sugeno fuzzy inference system with two inputs is shown in Figure 2.25 while Figure 2.26 shows the ANFIS architecture.

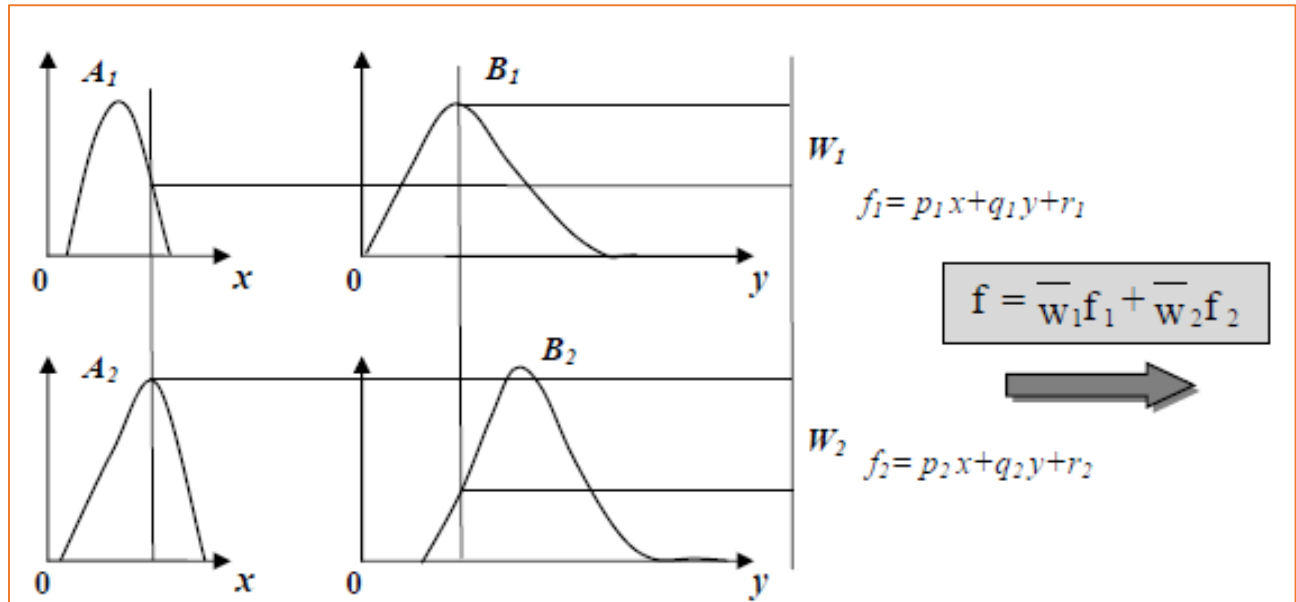


Figure 2. 25: First order Sugeno model [136]

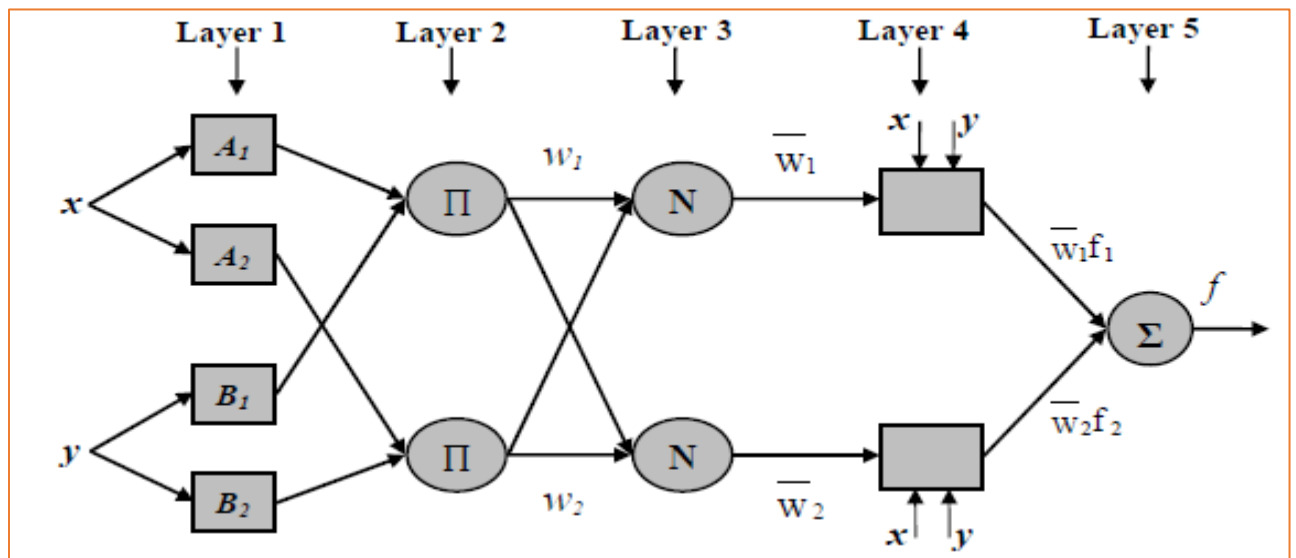


Figure 2. 26: ANFIS Architecture [136]

For the ANFIS structure with two inputs and one output, the rule base contains the Takagi-Sugeno fuzzy if-then rule as follows:

$$\text{If } x \text{ is } A \text{ and } y \text{ is } B \text{ then } z \text{ is } f(x, y)$$

where A and B are the fuzzy sets in the antecedents and $z = f(x, y)$ is a crisp function in the consequent. Usually $f(x, y)$ is a polynomial for the input variables x and y . For a first order two rule Sugeno fuzzy inference system, the two rules may be stated as:

$$\text{Rule 1: If } x \text{ is } A_1 \text{ and } y \text{ is } B_1 \text{ then } f_1 = p_1x + q_1y + r_1 \quad (2.47)$$

$$\text{Rule 2: If } x \text{ is } A_2 \text{ and } y \text{ is } B_2 \text{ then } f_2 = p_2x + q_2y + r_2 \quad (2.48)$$

Layer 1: Membership functions for input parameters are contained in this layer. The examples of membership functions used in Layer 1 are triangular and bell shaped. The membership function for layer one is given by the following equation,

$$O_i^1 = \mu_{A_i}(x) \quad (2.49)$$

Where x = node i input

A_i = linguistic variable associated with node i

Layer 2: the weight of each membership function is checked in layer 2. Input variables from layer 1 are received and it represents the fuzzy sets of the received input parameters. Membership value computation takes place at this stage and the degree of membership to a given set is determined. The result of layer 2 is forwarded to layer 3. Incoming signals are amplified in this layer. The firing strength of the function is represented by the output at this node.

$$O_i^2 = \mu_{A_i}(x)\mu_{B_i}(y) \quad (2.50)$$

Where $i = 1:2$

Layer 3: The alternative name of layer 3 is the rule layer. Fuzzy rule pre-condition matching is performed by the nodes in this layer. At this level, the ratio of the i th rule's firing strength to the sum of all firing strengths is calculated.

$$O_i^3 = \bar{W}_i = \frac{W_i}{W_1+W_2} \quad (2.51)$$

Where $i = 1:2$

Layer 4: The alternative name for this layer is the defuzzification layer. This gives the output of the inference system. The node function at this stage is given as follows:

$$O_i^4 = f_i \bar{W}_i (P_i x + Q_i y + R_i) \quad (2.52)$$

Where $i = 1:2$

Layer 5: Transformation of fuzzy results and the summation of all incoming signals are computed at this stage.

$$O_i^5 = \text{system output} \quad (2.53)$$

Where $i = 1:2$

2.7.4.3 ANFIS Learning Algorithm

A learning algorithm equips the ANFIS model with the capability to learn about a given input/output data set. The procedure entails computation of membership function parameters for the given input/output data set. The calculated membership function parameters determine the association between the input and output data set. During the learning process, the membership function parameters are modified to reduce errors. The learning algorithm has the responsibility of mapping all the input data to the output data during the training stage [137]. According to research, a hybrid learning algorithm that combines Least Squares Method (LSM) and Gradient Descent Method (GDM) has enhanced convergence. Layer 4 consequent parameter optimal value is identified by the least squares method while the premise parameter is fixed. The efficiency of the fuzzy inference system is determined by the gradient vector as the value of the gradient vector obtained determines the degree of adjustment required to reduce error [138]. Convergence is improved by reduction of the search space through premise parameters fixing. The forward propagation of the hybrid learning algorithm employs the least squares method (LSM) while the backward propagation employs the gradient descent method (GDM). Table 2.9 shows a comparison between the two passes in the hybrid learning algorithm.

Table 2. 9: The two passes in the hybrid learning algorithm [119]

	Forward Pass	Backward Pass
Premise Parameters	Fixed	Gradient descent
Consequent Parameters	Least-squares Estimator	Fixed
Signals	Node outputs	Error Signals

2.7.4 Regression Model

Regression analysis is a statistical means for estimating the relationship among variables. The variables include a set of independent and dependent variables. The independent variables are also known as predictor variables while the dependent variable is called the criterion variable. Knowledge of the relationship among variables enables the estimation of the dependent variables in situations where only independent variables are available. The regression model is a widely used model in surface roughness prediction during single point diamond turning. The model is the form of a mathematical equation shown by equation 2.54. The significance of the independent variables can be assessed using the Analysis of Variance (ANOVA).

$$Y = b_0 + b_1x_1 + \dots + b_px_p \quad (2.54)$$

Where

Y = dependent variable

x_i = independent variables

b_i = regression coefficients

2.8 Conclusion

The purpose of this review was to gain an insight into the various factors that affect surface roughness as well as the available surface roughness prediction models. It is clear from the reviewed literature that surface roughness is directly affected by cutting parameters. It is also evident that the extracted acoustic emission signals contain some unique signatures that are valuable in surface roughness prediction. There is limited research on the use of Adaptive Neuro-Fuzzy Inference System model incorporating acoustic emission signal parameters. Hence the decision to study that field. This study will expand the already available body of knowledge on surface roughness prediction methods for RSA-443. The next chapter explains the major components and stages used in ultra-high precision diamond turning of RSA-443.

CHAPTER THREE

3.0 MATERIALS AND METHODOLOGY

3.1 Introduction

In this chapter, the stages involved in achieving the research objectives are highlighted. These stages range from materials selection, through design of experiment to the prediction of surface roughness. Lastly, the Adaptive Neuro-Fuzzy Inference System (ANFIS) prediction results are analyzed by comparison to Regression model results using Mean Absolute Percentage Error (MAPE). The Ultra-High Precision Diamond Turning (UHPDT) process is performed under two types of coolants: kerosene and water.

3.2 Workpiece Material Selection

A 60 mm diameter cylindrical specimen of RSA-443 is used in this investigative research. The workpiece is firmly fixed to an adapter disk for ease of holding with the machine vacuum chuck. The RSA 443 workpiece contains 40% silicon. Figure 3.1 shows the RSA 443 workpiece mounted on an aluminum adapter disk. Table 3.1 shows the mechanical, physical and thermal properties of RSA 443.

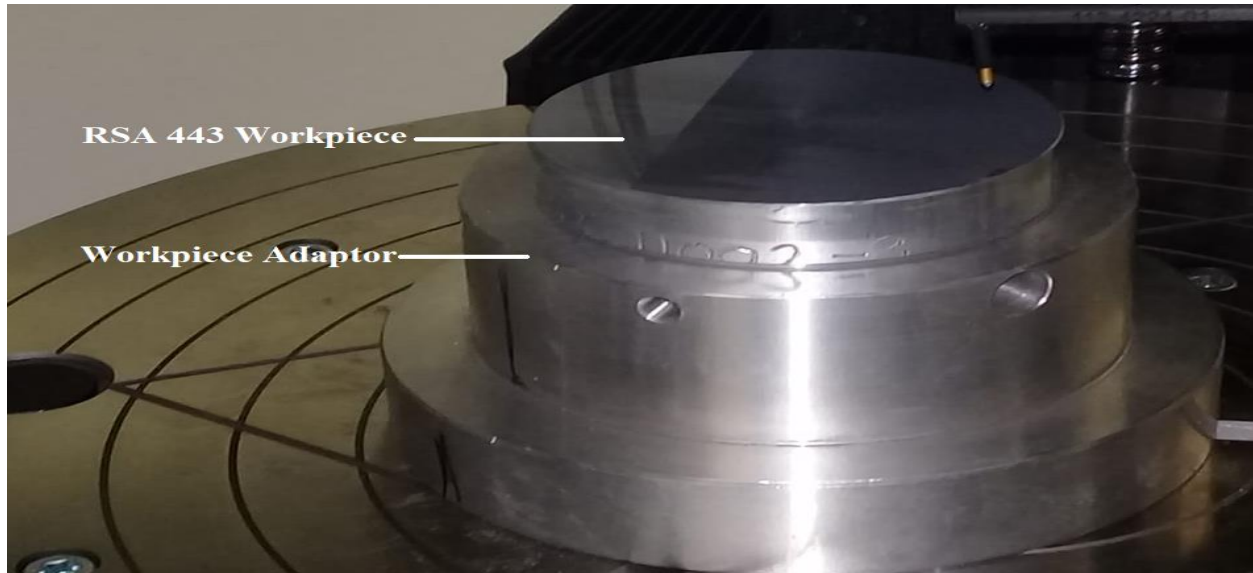


Figure 3. 1: RSA 443 Workpiece Mounted on Aluminum Adapter Disk

Table 3. 1: Mechanical Properties of RSA 443 Alloy [139]

Property	Nominal Value	Unit
Hardness	105	HB
Density	2.54	g/cm^2
Thermal Expansion	13.6	$10^{-6}/\text{K}$
Young's Modulus	102	GPa
Ultimate Tensile Strength	245	MPa
Yield Strength	155	MPa
Elongation	1.5	%

3.3 Design of Experiment

The steps followed in designing the experiment are shown in Figure 3.2.

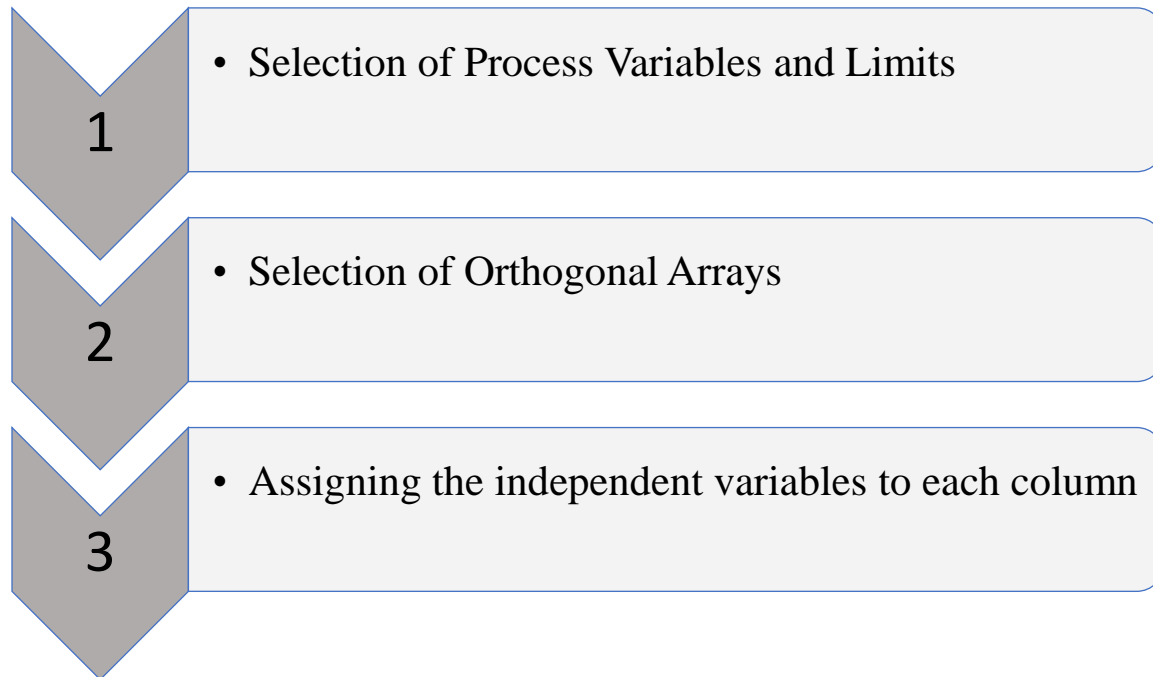


Figure 3. 2: Design of Experiment Steps

3.3.1 Selection of Process Variables and Limits

Spindle speed, feed rate and depth of cut have been chosen as process variables in this investigative research study. Three levels have been decided for each of the three cutting parameters with the manufacturer's recommended value as the center value. The spindle speed should be as high as practical in order to save time and to minimize temperature rise in the part. The depth of cut should be as great as possible within the limits of part strength, chucking equipment, power of the machine tool and amount of stock to be removed in order to minimize the number of cuts required. Feed depends on the desired finish and on the strength and rigidity of the workpiece. The process

parameters with their associated levels are shown in Table 3.2. The recommended process parameters are given in the ASM Handbook of Machining that is attached in Appendix B.

Table 3. 2: Process Parameters with associated levels

Parameters	Levels		
	1	2	3
Spindle Speed (rpm)-A	1250	1750	2500
Feed (mm/min)-B	7.5	15	22.5
Depth of Cut (μm)-C	5	15	25

3.3.2 Selection of Orthogonal Arrays (Taguchi Design)

Orthogonal arrays enable the determination of parameter effects on a response using the least number of experimental runs. Before selecting an orthogonal array, the minimum number of experiments to be conducted is to be fixed based on equation (3.1).

$$N_{\text{Taguchi}} = 1 + NV(L - 1) \quad (3.1)$$

Where N_{Taguchi} = Number of experiments to be conducted

NV = Number of parameters

L = Number of levels

The pre-condition for equation (3.1) is that $L \geq 4$. Hence, in this research, $NV=3$ and $L=4$.

Substituting NV and L in equation (3.1);

$$N_{\text{Taguchi}} = 1 + 3(4 - 1) = 9$$

According to this result, at least 9 experimental runs (L9 Taguchi orthogonal array) are to be conducted.

3.3.3 Assigning the independent variables to each column

The independent variables and their respective levels are expressed in tables (see Table 3.3 and Table 3.4).

Table 3. 3: Levels of process parameters used in Taguchi (L9) Orthogonal Array

Experiment Number	Levels		
	A	B	C
1	1	1	1
2	1	2	2
3	1	3	3
4	2	1	2
5	2	2	3
6	2	3	1
7	3	1	3
8	3	2	1
9	3	3	2

Table 3. 4: Experimental design using L9 Taguchi orthogonal array

Experiment Number	Levels		
	Spindle Speed (rpm)	Feed (mm/min)	Depth of Cut (μm)
1	1250	7.5	5
2	1250	15	15
3	1250	22.5	25
4	1750	7.5	15
5	1750	15	25
6	1750	22.5	5
7	2500	7.5	25
8	2500	15	5
9	2500	22.5	15

3.3.4 Tool Centering and Spindle Balancing

Prior to executing the experiment, the cutting tool is centered (see Figure 3.3), and the spindle is balanced (see Figure 3.4) to eliminate unwanted oscillations that negatively impact on the ultra-high precision diamond turning results. In this research, spindle balancing was carried out at 2 500

rpm, 2 000 rpm and 1 000 rpm. These selected balancing values cover all speed levels, that is, low, medium and high speeds that are used in this research.

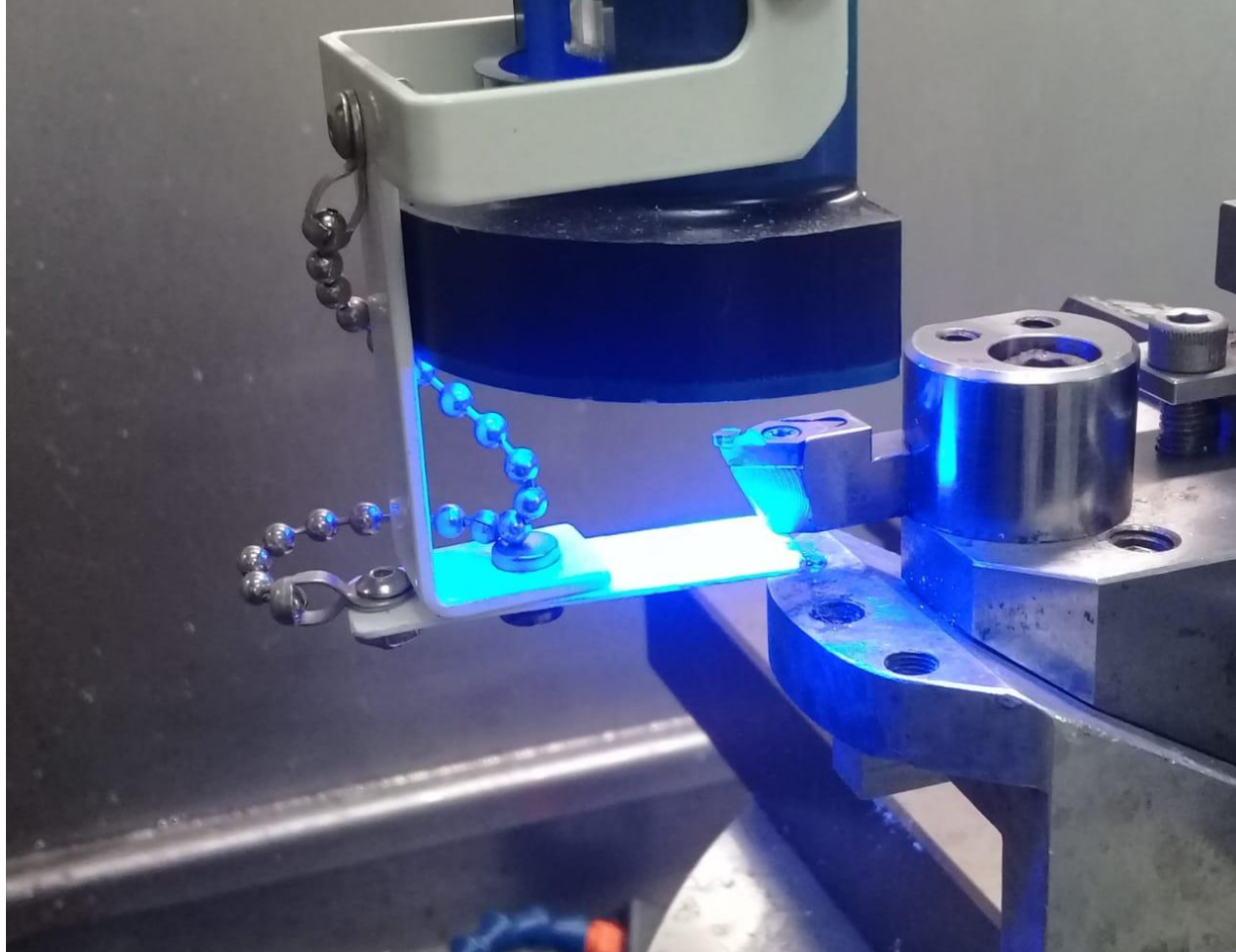


Figure 3. 3: Diamond Cutting Tool Centering

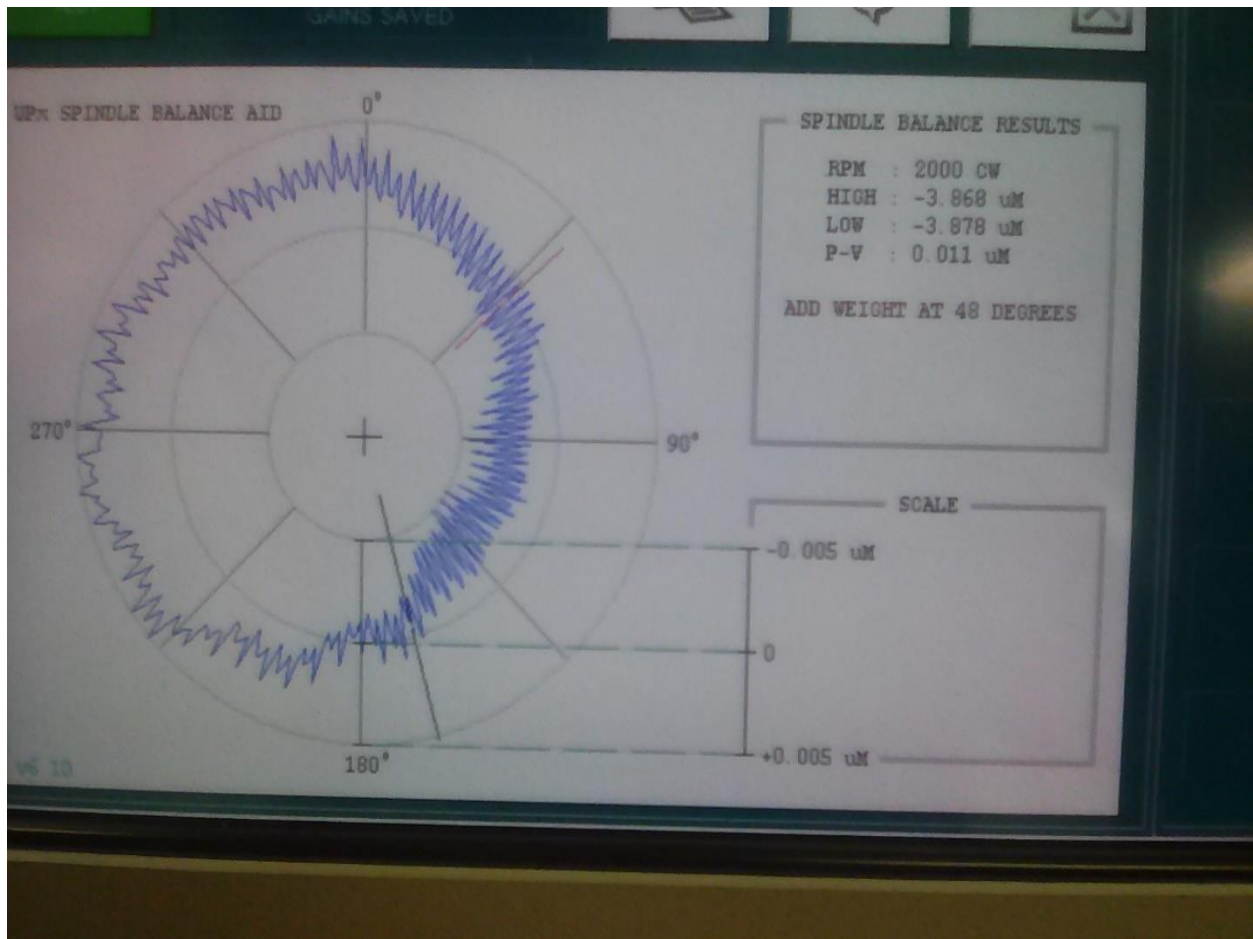


Figure 3. 4: Spindle balancing platform DIFFSYS

3.3.4 Ultra-High Precision Diamond Turning Setup

The ultra-high precision diamond turning process was performed on an ultra-grind Nanoform 250 Computer Numerical Control (CNC) machine with the machining setup shown (see Figure 3.5). The features of the CNC machine include a foolproof human machine interface, a natural built-in granite base for machine stability and an FEA optimized dual frame for protection against adverse environmental conditions. The cutting conditions of the ultra-high precision diamond turning experiments are summarized in Table 3.5.

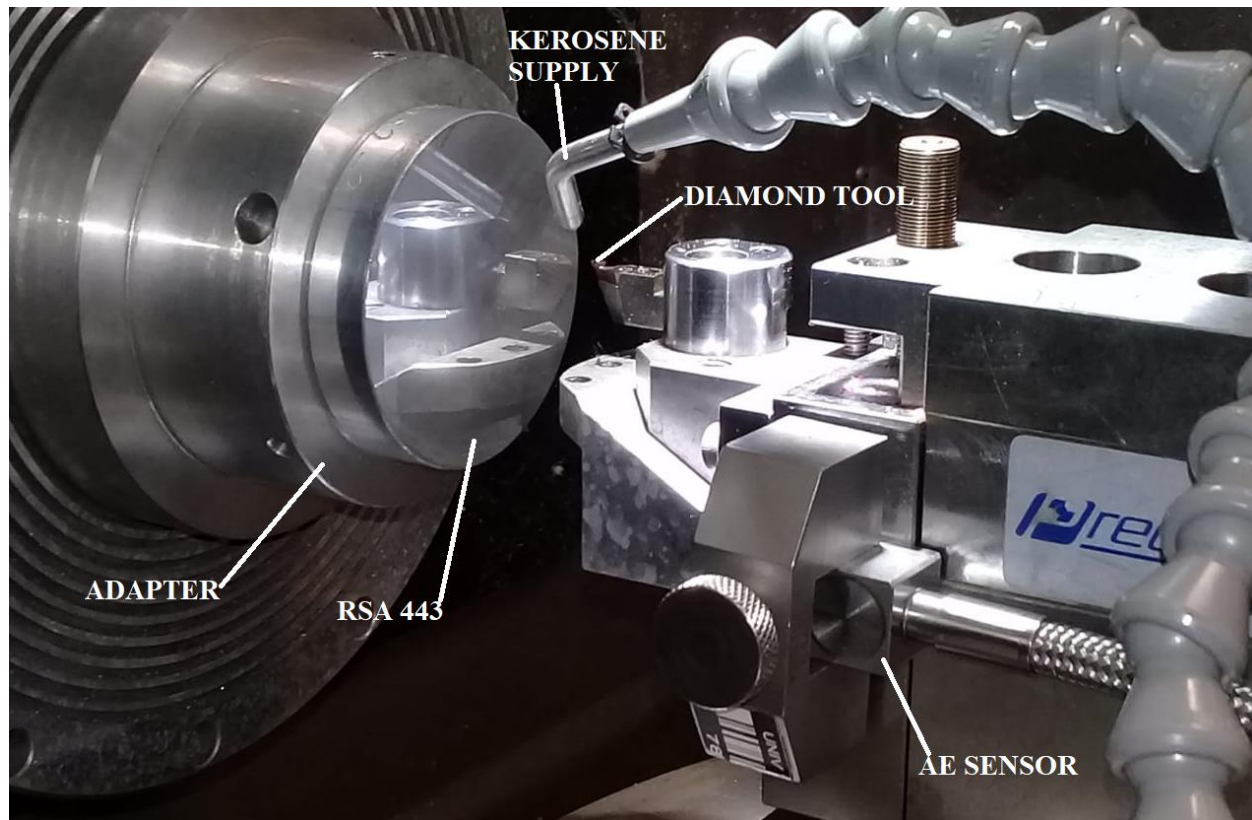


Figure 3. 5: Ultra-High Precision Diamond Turning Setup

Table 3. 5: RSA 443 Cutting conditions

Cutting Condition	Specification
Workpiece	RSA 443
Rake angle	-5°
Nose radius	0.5 mm
Tool	Single crystal natural diamond

3.3.4.1 Experimental Procedure

- The Piezotron sensor is secured to the spindle mount by means of a magnetic clamp at 4cm from workpiece to detect acoustic emission signals generated during the ultra-high precision diamond turning of RSA 443.
- A Kistler Piezotron coupler (5125B) is directly connected to the Piezotron sensor. Its purpose is to amplify, filter and RMS conversion of the acquired acoustic emission signal.
- Tool centering and balancing using gauge indicator and spindle balancing platform was done.
- Machine G-codes for the turning operation were entered.
- Facing of workpiece surface was done before actual tests were run.
- The acoustic emission data of each experimental run was acquired. The LabVIEW software (front panel) showing AE signal during RSA 443 machining is shown in Figure 3.6.
- The surface roughness of each experimental run was determined using a Taylor Hobson Profilometer, prior to the subsequent experimental run.

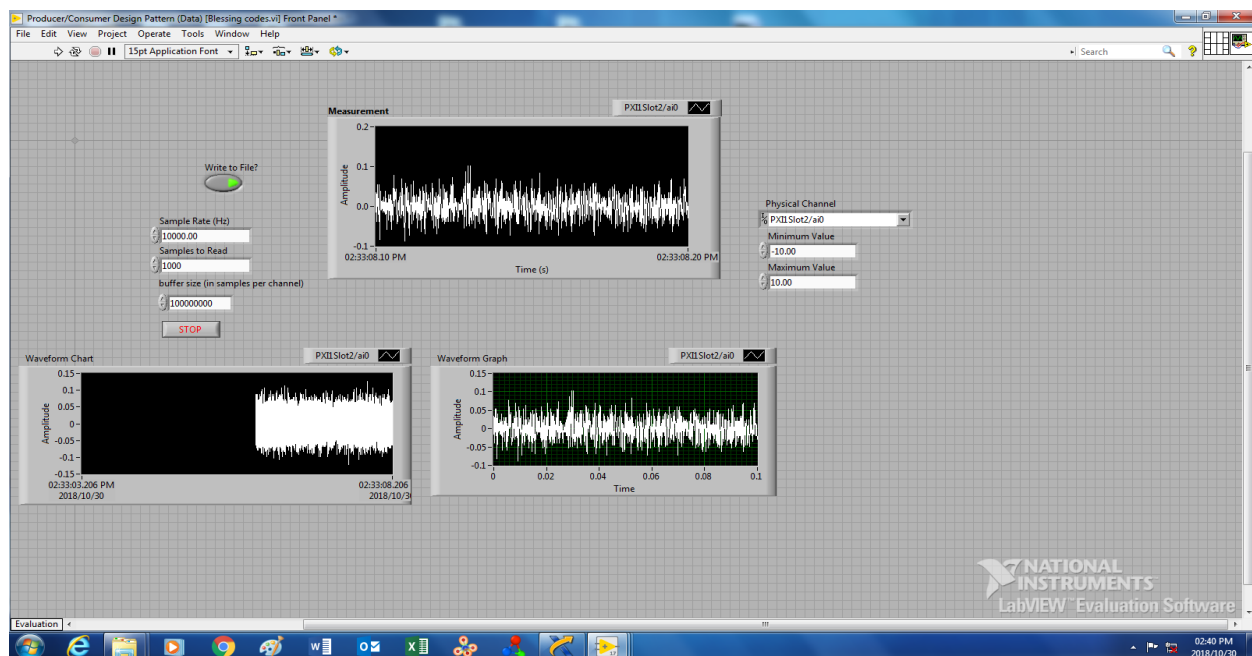


Figure 3. 6: LabVIEW Software (front panel) showing AE signal during RSA 443 Machining

3.3.5 Surface Roughness Measurement Setup

A contact-type Taylor-Hobson profilometer (see Figure 3.7) was used to measure the surface roughness of machined workpieces since it can be used with a wide variety of surface types. Transverse direction surface roughness measurements of the machined workpiece are made and recorded in a table. The description of the profilometer used is represented by Table 3.6.

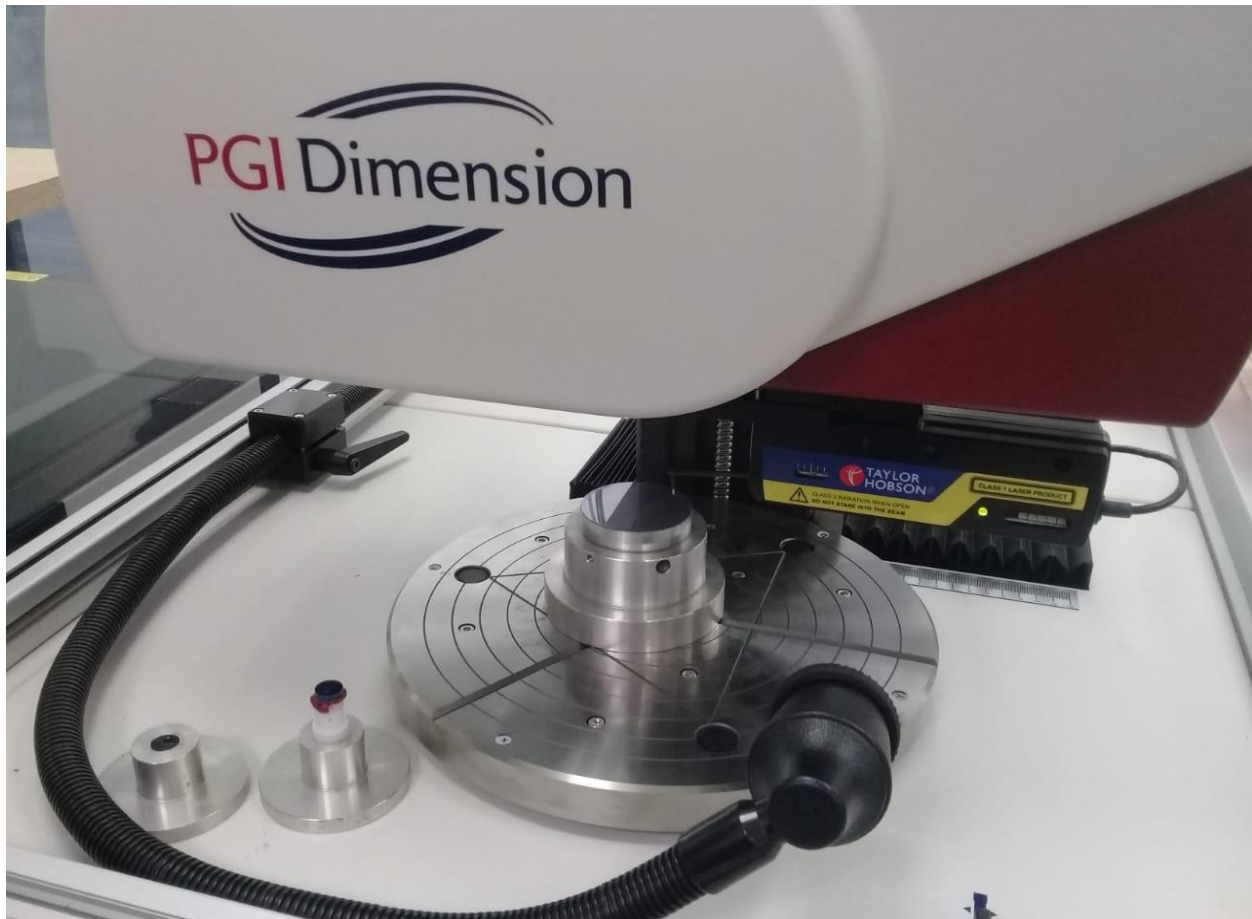


Figure 3. 7: Taylor Hobson Profilometer

Table 3. 6: Taylor Hobson Profilometer Description

Feature	Specification
Repeatability	50 nm
Diameter of optics measuring possibility	<2 mm
Maximum measured diameter	300 mm
Maximum surface sag	20 mm

3.3.6 Acoustic Emission Signal Acquisition Experiment Process Flow

The acoustic emission signal data acquisition process has three segments namely, sensing, signal processing and storage and display (see Figure 3.7). The Piezotron sensor is a transducer that converts force into an electrical signal which is magnified by an amplifier. The in-built filter eliminates the noise components of the signal that is interfaced to the storage and display unit by the data acquisition card. The acoustic emission signal circuit components specifications for this research are given (see Table 3.7). The components used are active components that require power supply to work.

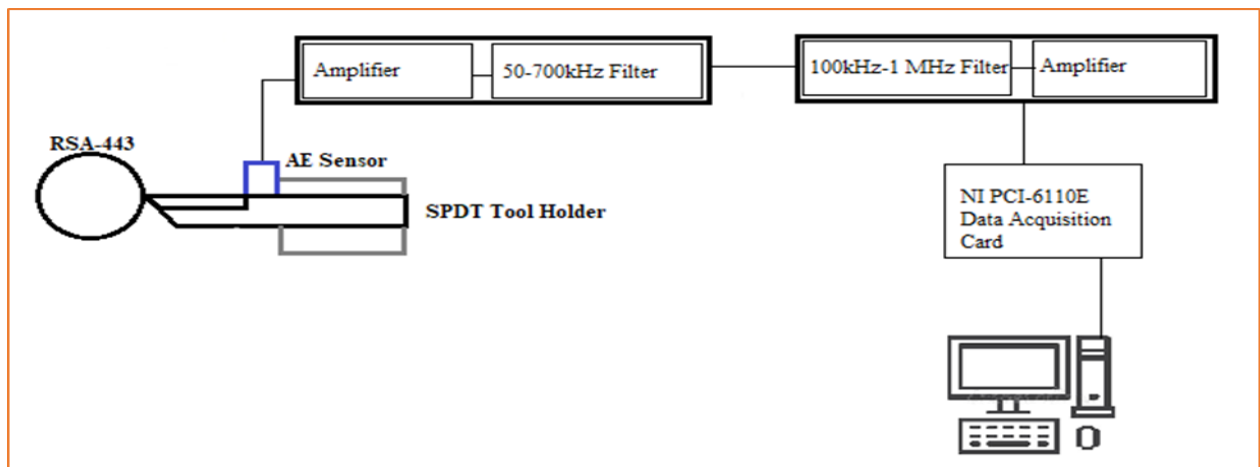






Figure 3. 8: Acoustic Emission Signal Acquisition Experiment Process Flow

Table 3. 7: Acoustic Emission Signal Circuit Components Specifications.

COMPONENT	SPECIFICATION	IMAGE
Piezotron Sensor	Kistler 8152B	 A cylindrical piezotron sensor with a threaded end and a label that reads 'KISTLER 8152C1050500 SN 0000005 CE'.
Piezotron Coupler	Kistler 5125B	 A blue rectangular piezotron coupler with two BNC connectors on the front and a label that reads 'KISTLER 5125B'.
Connector	BNC-2110	 A small, rectangular BNC-2110 connector with multiple ports.
Power Source	Input/output Voltage (220V/24V)	 A silver metal power source with a perforated top and a label that reads '24V 10A'.
High Pass Filter	50 kHz to 700 kHz	In-built
Low Pass Filter	100 kHz to 1 MHz	In-built
Data Acquisition Card	NI PCI-6110E	

3.3.7 Acoustic Emission Signal Feature Extraction

Once the acoustic emission signal has been captured, a systematic approach is utilized to extract signal features of interest. In this case, peak rate, AERms and peak frequency are determined for the captured acoustic emission signals.

3.3.5.1 Acoustic Emission Peak Rate Determination

Figure 3.9 is a flow chart for the MATLAB algorithm that was developed to determine the peak rate of the acoustic emission signals in time domain. The algorithm is shown in Appendix C. In this thesis, a peak is defined as a point whose value is greater than 0.04 and greater than its adjacent points. The value of 0.04 was judiciously chosen by the student as a way of dealing with well pronounced peaks. Below the value, the peaks are not distinct.

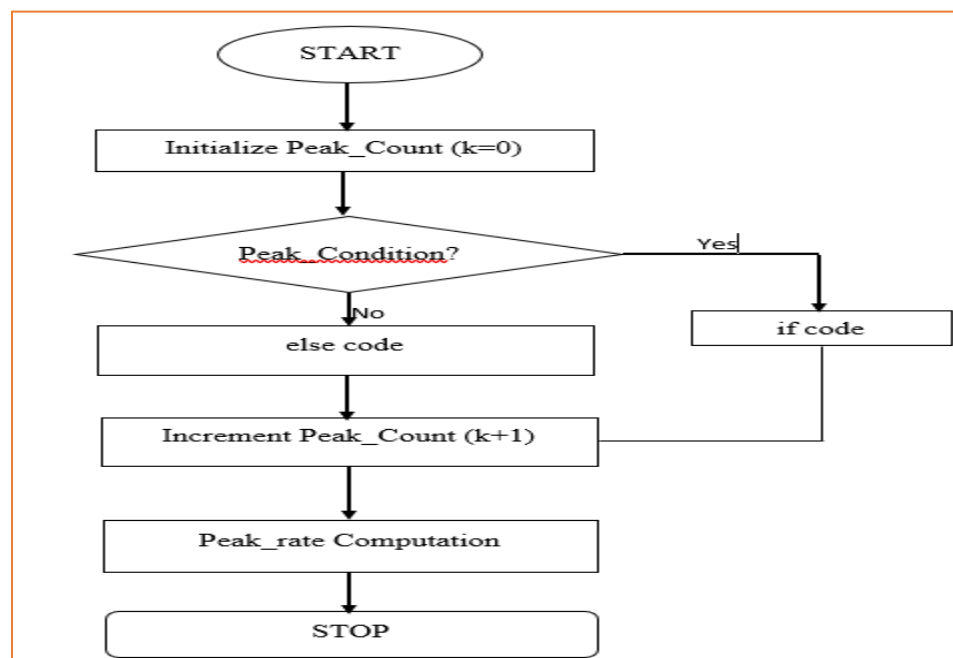


Figure 3. 9: Acoustic Emission Peak Rate Determination Flow Chart

3.3.5.2 Acoustic Emission Root Mean Square Determination

Acoustic emission Root Mean Square is determined according to equation (3.2).

$$RMS = \sqrt{\frac{1}{N} [\sum_{i=1}^N (X_i)^2]} \quad (3.2)$$

Where N = total number of events

X_i = amplitude vibration signal

i = order of event

3.3.5.3 Peak Frequency Determination

The signal peak frequency was extracted from the Fourier transformed signal in the EXCEL platform. Figure 3.10 represents the steps that were taken to achieve the task:

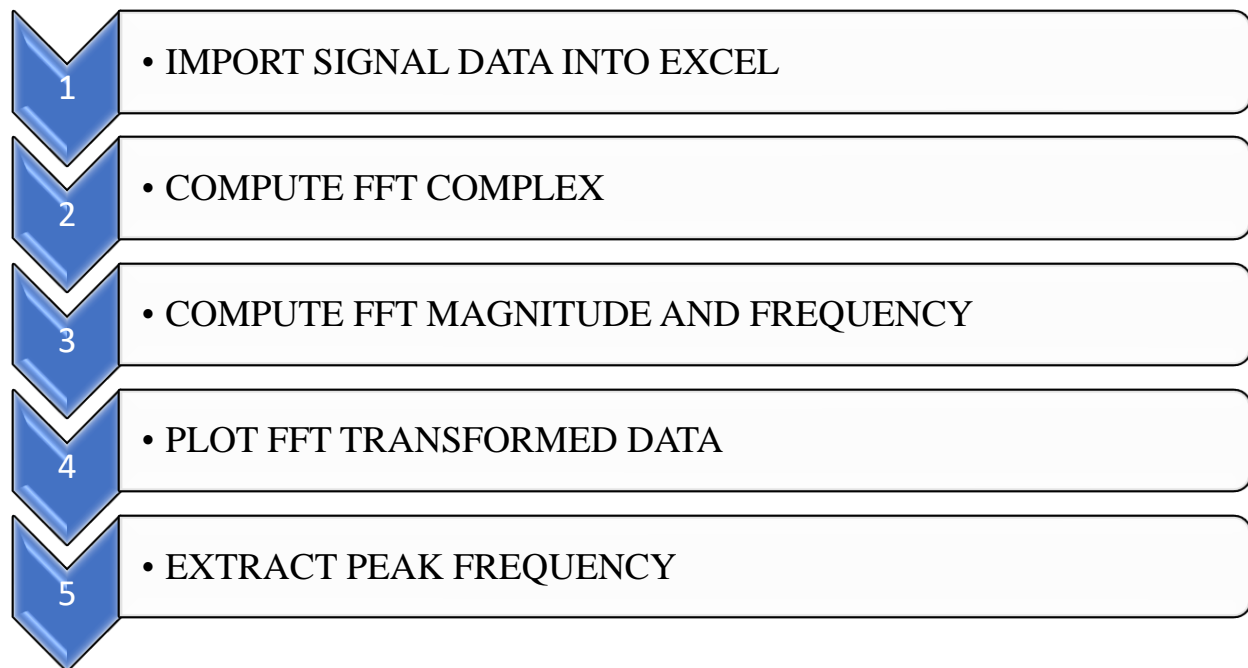


Figure 3. 10: Peak Frequency Determination Flow Chart

3.3.6 Adaptive Neuro-Fuzzy Inference System Modelling

In this investigative research, a two-layered feed-forward ANFIS architecture with six inputs is used to predict the surface roughness of single point diamond turned RSA 443. Use is made of the Sugeno-style Fuzzy Inference and gaussian membership functions. Three (3) membership functions will be used and they will divide the range into 3 equal portions. The ANFIS model process flow followed in this thesis is presented in Figure 3.11. Use is made of ANFIS toolbox in MATLAB environment.

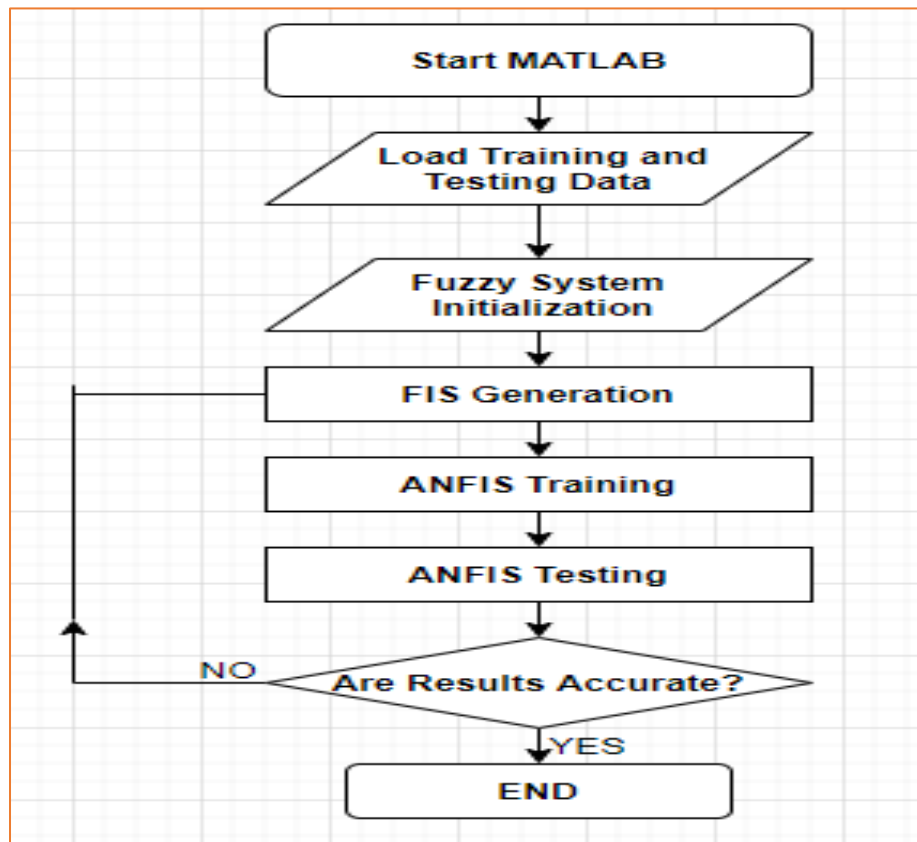


Figure 3. 11: ANFIS Model Process Flow

- Fuzzy System Initialization: At this stage, both training data sets and checking data sets are loaded from storage file to the workspace and subsequently to the ANFIS graphical user interface. The used data has six input parameters namely, feed rate, cutting speed, depth of cut, AErms, peak frequency and peak rate. Surface roughness parameter (Ra) is the output from the model. The loaded data is in numeric matrix format with the first

columns representing inputs while the output is represented by the last column. The ANFIS Editor display in Fig. 3.12 shows the loading sub-display.

- **Generation of Fuzzy Inference System:** This stage follows the loading of data into the system. The Inference System is generated by FIS command in the ANFIS editor graphical user interface. The Sugeno-style Fuzzy Inference is used in this research. At this stage, the number and type of membership functions used is specified. The gaussian membership functions will divide the range into 3 equal portions.
- **Initiate Learning Process:** Since a complete fit is not achievable, the default tolerance of 0 is changed, hence a tolerance of 0.001 is used in this research. The default number of epochs in MATLAB is 3. This value is not enough for training, hence 20 epochs are used in this research. The epochs are the number of iterations that must be carried out until the data begins to overfit.
- **Validation of Results:** Once the training process has been completed, the results are tested by comparison with testing data. In this thesis, three additional experimental runs are carried out to provide testing data. Seven data sets are used as training data while the remaining five data sets are used as testing data.

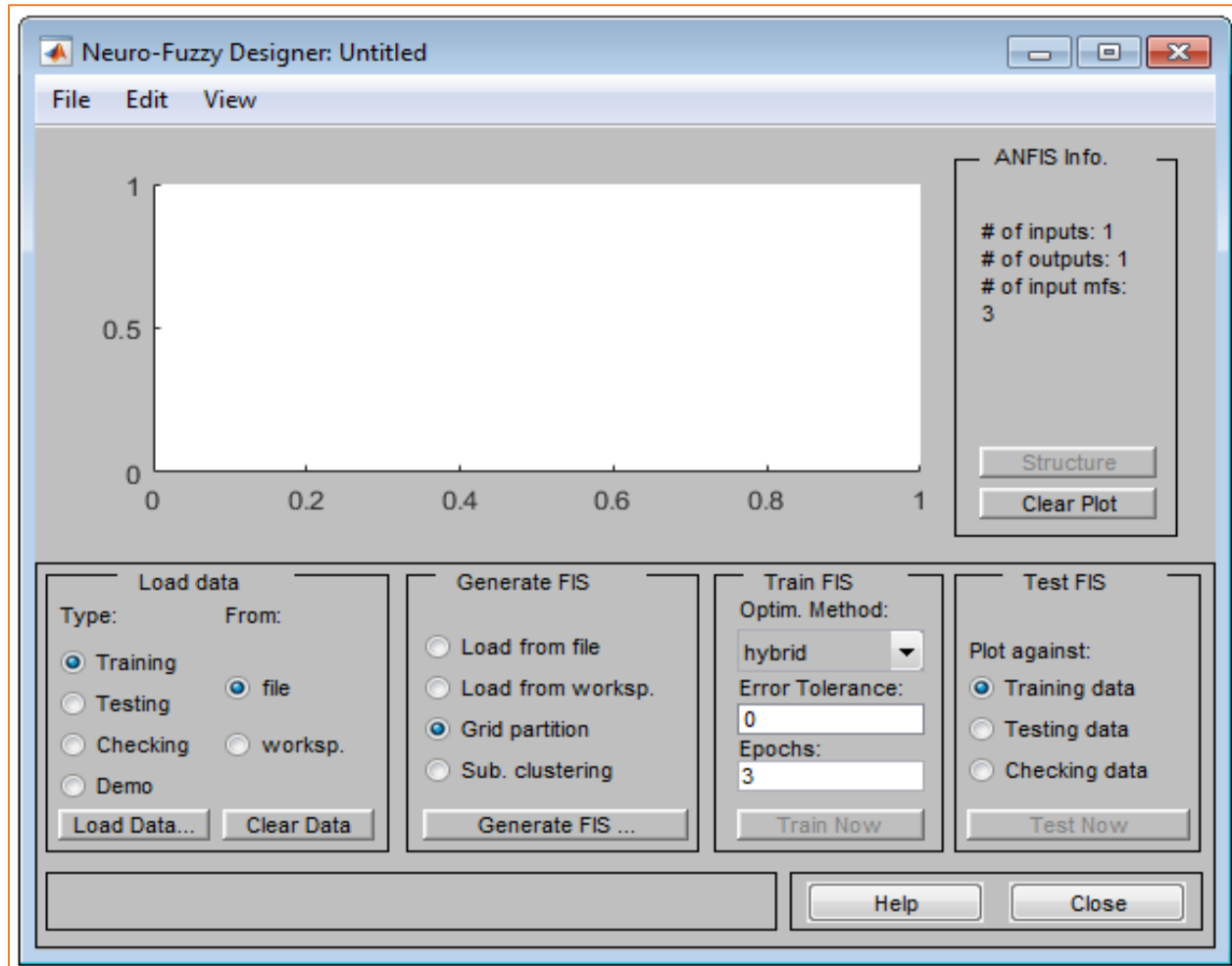


Figure 3. 12: ANFIS Editor Display

3.4 Conclusion

This chapter has managed to explain the major components and stages used in ultra-high precision diamond turning of RSA-443. The next chapter is aimed at investigating the surface roughness prediction accuracy of ANFIS. Comparison is made of ANFIS prediction accuracy to RSM. Use is made of the Mean Absolute Percentage Error.

CHAPTER FOUR

4.0 RESULTS AND DISCUSSION

4.1 Introduction

This section presents results obtained during Ultra-High Precision Diamond Turning (UHPDT) of RSA 443 under different coolants (kerosene and water). A comparison is made between surface finishes for water and kerosene coolants. For both coolants, the surface profile charts for the worst and best surface roughness finishes are presented. Acoustic emission signal features (AERms, peak rate and prominent frequency) are acquired from the captured signals. Using cutting parameters (spindle speed, depth of cut and feed rate) and signal parameters, Regression and ANFIS models are utilized in predicting the surface roughness of the machined components. The model accuracy for both coolants is determined using the Mean Absolute Percentage Error (MAPE) method. MATLAB software is utilized in surface roughness prediction in this chapter.

4.2 Surface Roughness Experimental Results

The Surface Roughness Experimental Results using kerosene and water coolants are tabulated in Table 4.1. The series plots of measured surface roughness for both coolants are shown in Figure 4.1.

Table 4. 1: Surface Roughness Experimental Results

Experiment Number	Spindle Speed (rpm)	Feed (mm/min)	Depth of Cut (μm)	Ra (nm)	
				Kerosene Coolant	Water Coolant
1	1250	7.5	5	21	16
2	1250	15	15	33	21
3	1250	22.5	25	38	29
4	1750	7.5	15	17	14
5	1750	15	25	23	20
6	1750	22.5	5	26	21
7	2500	7.5	25	12	11
8	2500	15	5	18	14
9	2500	22.5	15	19	17

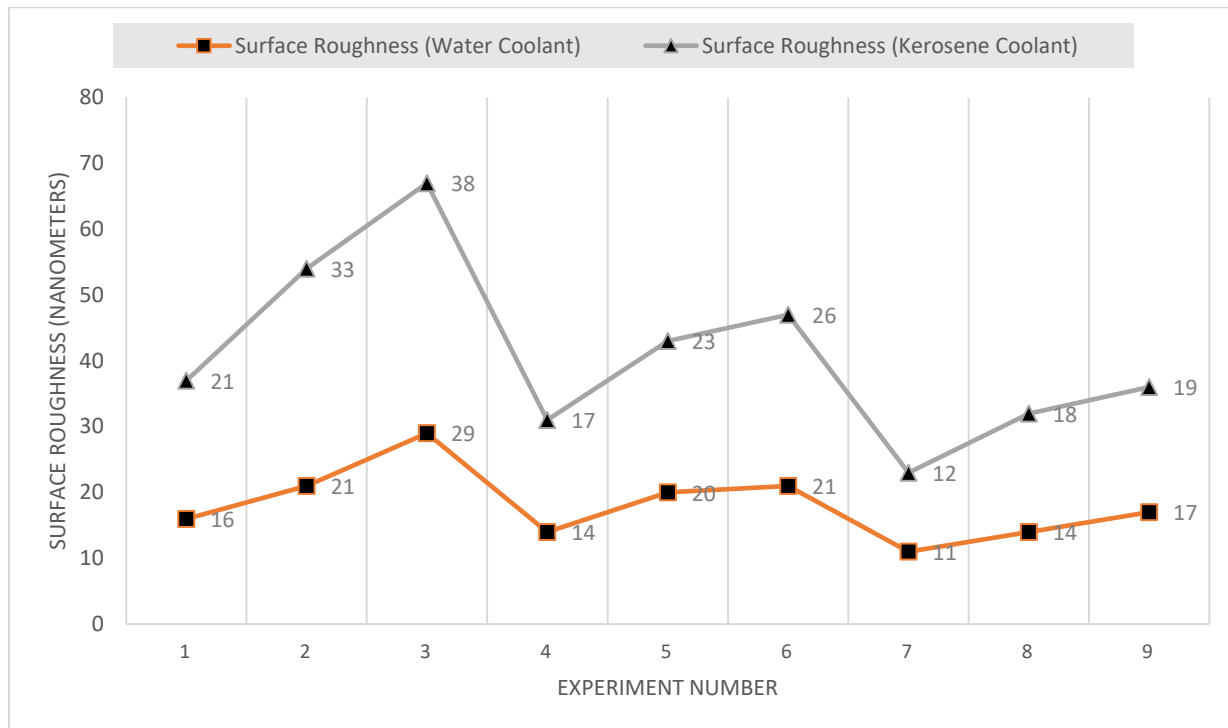


Figure 4. 1: Series Plots of Experimental Surface Roughness

The results indicate that the surface roughness values obtained using water as a coolant are better when compared to kerosene results. For either of the coolants, the lowest roughness values (12nm for kerosene and 11nm for water) occurred at a high spindle speed of 2500rpm, low feed of 7.5mm/min and depth of 25 μ m. Better surface finishes during ultra-high precision diamond turning of RSA 443 can be obtained at high speed and low feed. The worst surface roughness values for either coolants (38nm for kerosene and 29nm for water) occurred at low spindle speed of 1250rpm, high feed of 22.5mm/min and cutting depth of 25 μ m. These findings indicate that larger feed rate and lower spindle speed negatively impact on surface roughness. In this investigative research, both data sets will be used for prediction purposes. The percentage difference between surface roughness values is expressed as ΔRa . Spindle speed, feed rate and depth of cut are denoted by X1, X2 and X3 respectively while the surface roughness parameters for kerosene and water are denoted by Rk and Rw respectively. Table 4.2 presents the percentage differences between water and kerosene surface roughness values.

ΔR_a is calculated using equation 4.1:

$$\Delta R_a(\%) = \left(\frac{R_K - R_W}{R_K} \right) \times 100. \quad (4.1)$$

Where R_K = Kerosene-based surface finish parameter

R_W = Water-based surface finish parameter

Table 4. 2: Percentage Difference Between Water and Kerosene Surface Roughness Values

X1	X2	X3	Ra (nm)		ΔR_a (%)
			Rk	Rw	
1250	7.5	5	21	16	-23.81
1250	15	15	33	21	-36.36
1250	22.5	25	38	29	-23.68
1750	7.5	15	17	14	-17.65
1750	15	25	23	20	-13.04
1750	22.5	5	26	21	-19.23
2500	7.5	25	12	11	-8.33
2500	15	5	18	14	-22.22
2500	22.5	15	19	17	-10.53
Delta-Mean					-19.43

The mean percentage change from kerosene to water-based results is -19.43%. The negative sign depicts a decrease in surface roughness. The largest change in surface roughness occurs at the second experiment run with a value of -36.36%. The lowest change in surface roughness occurs at the seventh experiment run with a value of -8.33%. The best and the poor surface roughness profile charts from the Surface Profilometer for RSA 443 are given in Figure 4.2 and Figure 4.3.

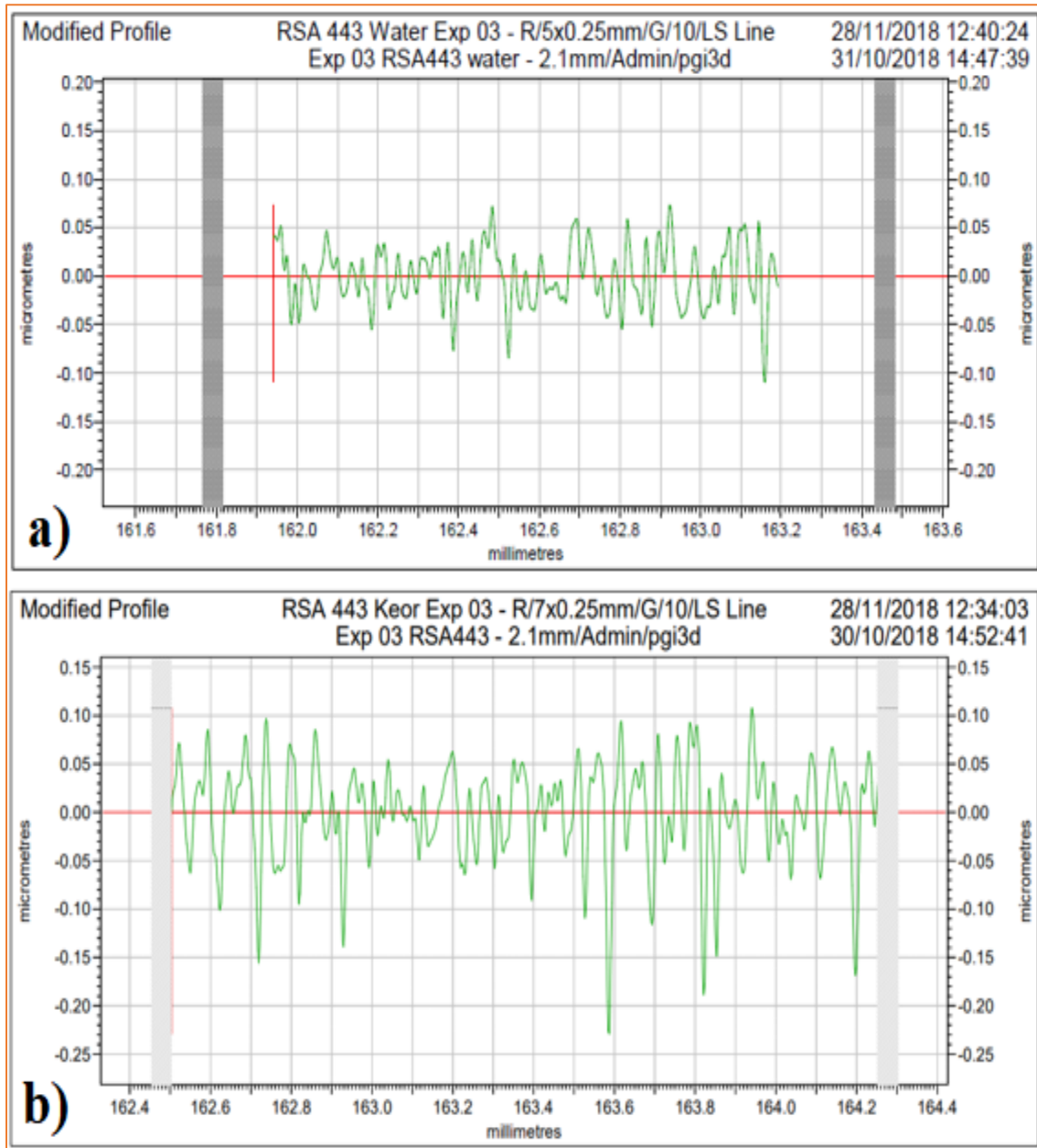


Figure 4. 2: a) Surface Profile Chart for Worst Water Ra value (29 nm) and b) Surface Profile Chart for Worst Kerosene Ra value (38 nm)

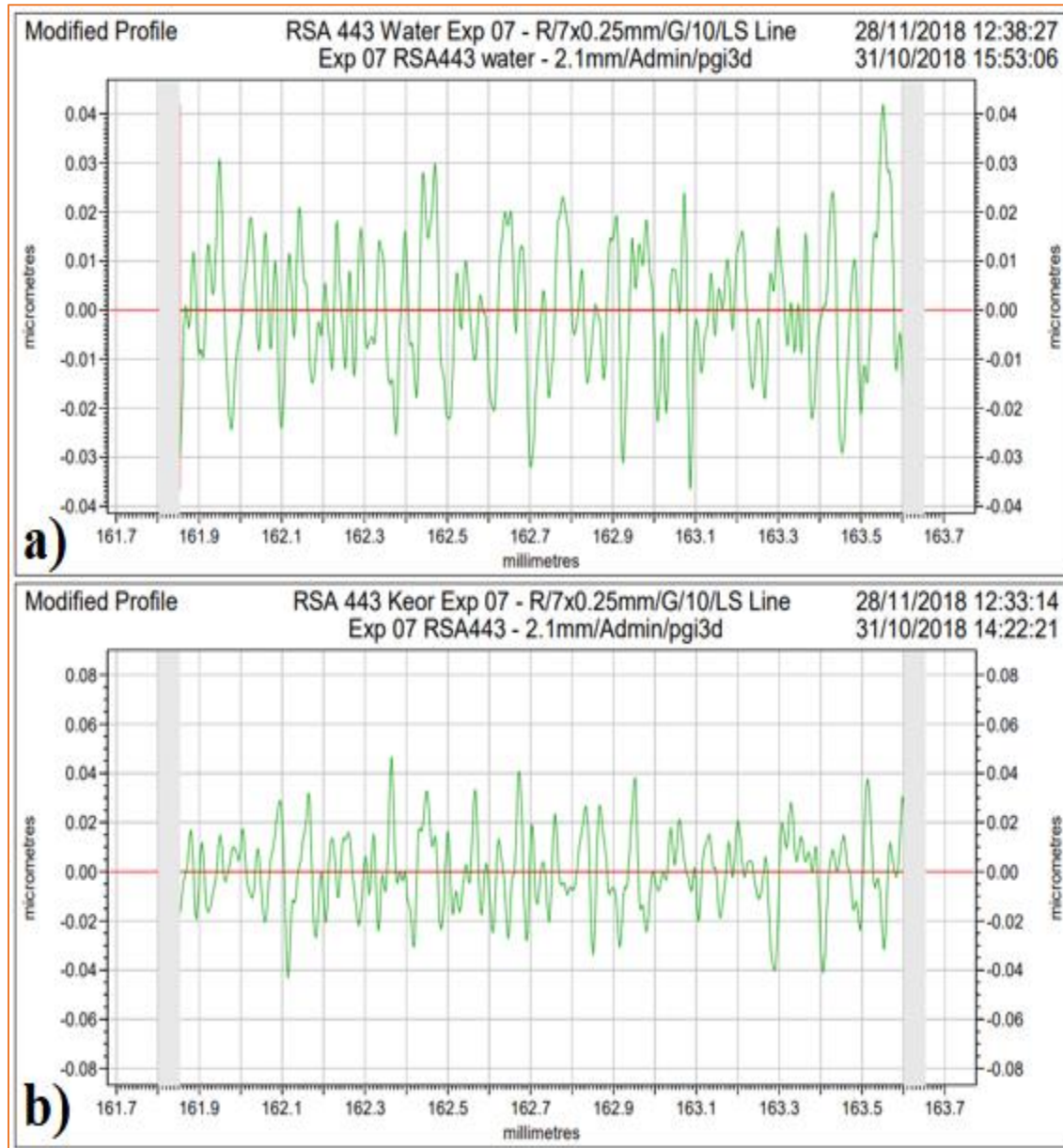


Figure 4. 3: a) Surface Profile Chart for Best Water R_a value (11 nm) and b) Surface Profile Chart for Best Kerosene R_a value (12 nm)

4.3 Determination of Acoustic Emission Signal Parameters

Acoustic emission root mean square (AE_{rms}), prominent frequency and peak rate are determined from the emitted AE signal. The acoustic emission signal amplitude variation with time and

corresponding prominent frequency for experimental runs 3 and 7 for either coolant is shown in Figures 4.4 and 4.5. The acoustic emission signal count rate for all signals are determined. In this research, a peak is defined as a sample greater than its two nearest neighbors and greater than 0.04. the MATLAB code for peak rate determination is included in Appendix B. All determined acoustic emission signal parameters are presented in Table 4.3 and Table 4.4.

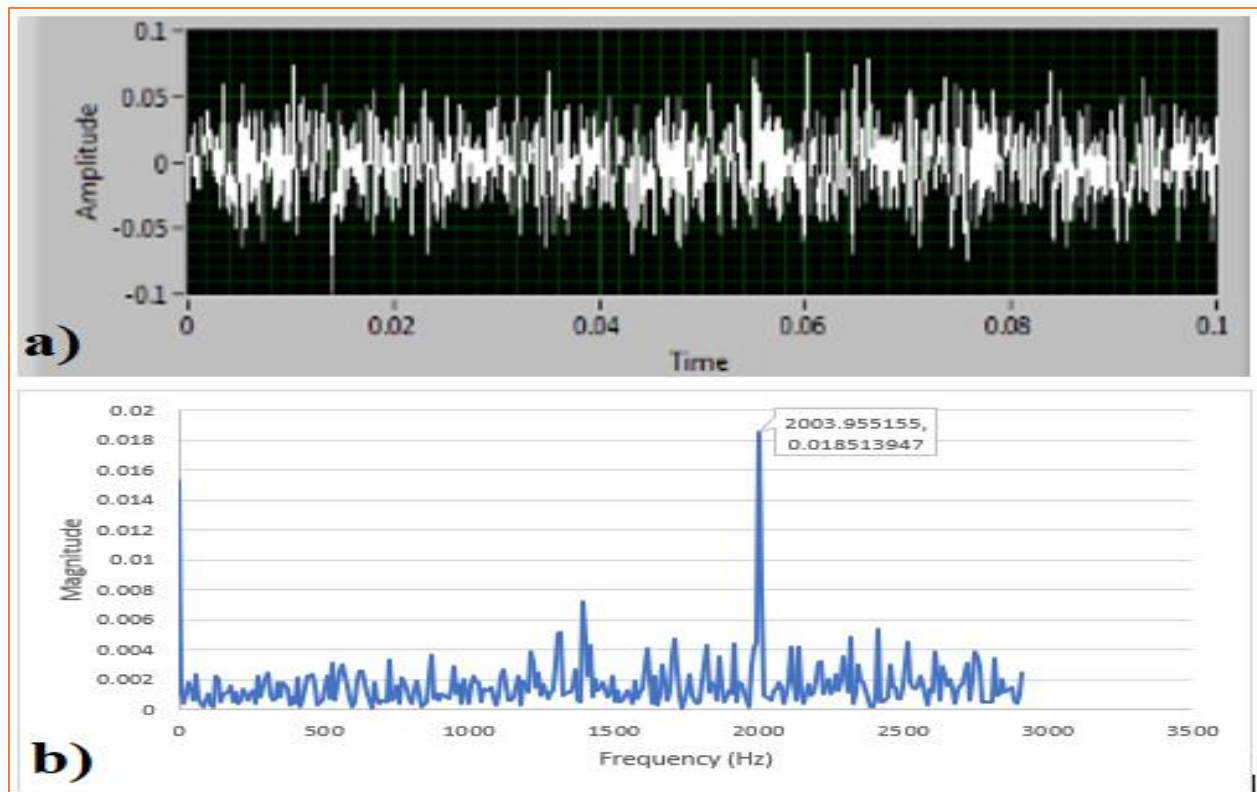


Figure 4. 4: a) Time domain signal for $R_a=38\text{nm}$ (kerosene) and b) Frequency domain signal for $R_a = 38\text{nm}$ (kerosene)

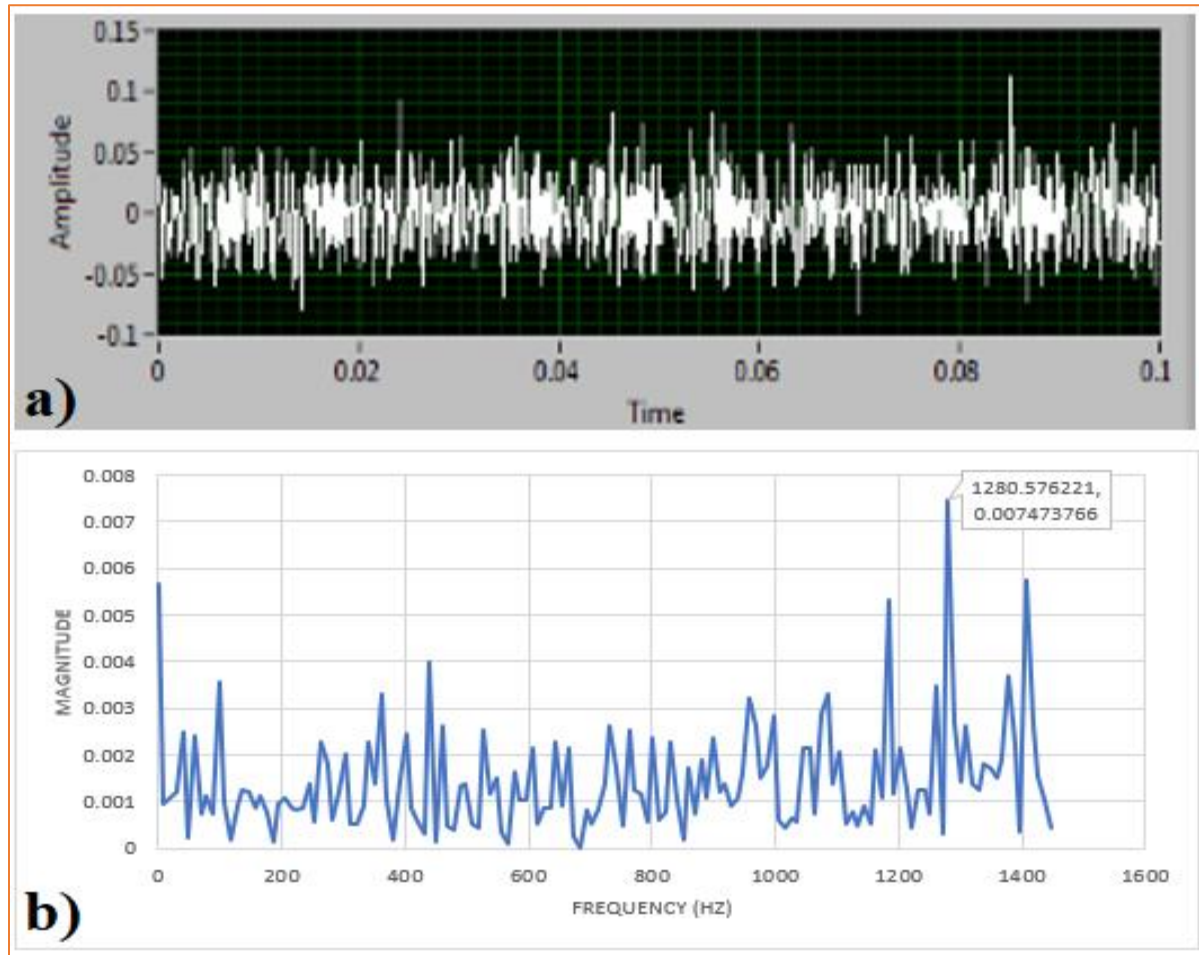


Figure 4. 5: a) Time domain signal for $R_a = 12\text{nm}$ (kerosene) and b) Frequency domain signal for $R_a = 12\text{nm}$ (kerosene)

Table 4. 3: Acoustic Emission Signal Analysis Results (Kerosene Coolant)

Experiment Number	Spindle Speed (rpm)	Feed (mm/min)	Depth of Cut (μm)	AERms (V)	Prominent Frequency (Hz)	Peak Rate (min^{-1})	R_a (nm)
1	1250	7.5	5	2.968e-2	566.973	4.1914e+04	21
2	1250	15	15	2.750e-2	645.176	1.14e+04	33
3	1250	22.5	25	2.825e-2	2003.955	3.8e+04	38
4	1750	7.5	15	2.781e-2	674.502	4.215e+04	17
5	1750	15	25	2.786e-2	1133.945	2.49e+04	23
6	1750	22.5	5	2.837e-2	2003.955	4.56e+04	26
7	2500	7.5	25	2.786e-2	1280.576	3.6e+04	12
8	2500	15	5	3.432e-2	2003.955	3.1e+04	18
9	2500	22.5	15	2.831e-2	1309.902	4.2e+04	19

Table 4. 4: Acoustic Emission Signal Analysis Results (Water Coolant)

Experiment Number	Spindle Speed (rpm)	Feed (mm/min)	Depth of Cut (μm)	AERms (V)	Prominent Frequency (Hz)	Peak Rate (min^{-1})	Ra (nm)
1	1250	7.5	5	3.090e-2	2003.955	6.102e+04	16
2	1250	15	15	2.746e-2	1300.127	4.002e+04	21
3	1250	22.5	25	3.140e-2	2003.955	6.710e+04	29
4	1750	7.5	15	2.696e-2	1407.656	3.227e+04	14
5	1750	15	25	2.661e-2	1407.656	3.234e+04	20
6	1750	22.5	5	2.639e-2	527.871	3.198e+04	21
7	2500	7.5	25	2.627e-2	1261.025	2.920e+04	11
8	2500	15	5	2.151e-2	469.219	1.397e+04	14
9	2500	22.5	15	2.721e-2	1397.881	3.513e+04	17

4.4 Regression Model Prediction of Surface Roughness

The regression model is formulated from the combination of different operating conditions and the measured surface roughness values at every experiment stage. The regression equation is calculated using Excel statistics analysis software. The Regression model computation results are presented in Table 4.5.

4.4.1 Water-Based Results Surface Roughness Prediction using Regression Model

The null hypothesis H_0 and the alternative hypothesis H_1 are formulated as follows:

$$H_0: R_a = b_0 \quad (4.2)$$

$$H_1: R_a = b_0 + b_1x_1 + \dots + b_px_p \quad (4.3)$$

Table 4. 5: Regression Model Computation Results

SUMMARY OUTPUT								
<i>Regression Statistics</i>								
Multiple R	0.997660035							
R Square	0.995325545							
Adjusted R Square	0.981302179							
Standard Error	0.731413314							
Observations	9							
<i>ANOVA</i>								
	<i>df</i>	<i>SS</i>	<i>MS</i>	<i>F</i>	<i>Significance F</i>			
Regression	6	227.818958	37.9698	70.9762	0.0139579			
Residual	2	1.06993087	0.53497					
Total	8	228.888889						
	<i>Coefficients</i>	<i>Standard Error</i>	<i>t Stat</i>	<i>P-value</i>	<i>Lower 95%</i>	<i>Upper 95%</i>	<i>Lower 95.0%</i>	<i>Upper 95.0%</i>
Intercept	42.33799131	8.44437388	5.01375	0.03755	6.004783	78.6712	6.004783	78.67119962
X1	-0.005960501	0.00080933	-7.3648	0.01794	-0.009443	-0.002478	-0.00944275	-0.002478254
X2	0.519925346	0.05651983	9.19899	0.01161	0.2767401	0.7631106	0.27674013	0.76311056
X3	0.201290757	0.04114664	4.89203	0.03934	0.024251	0.3783305	0.02425104	0.378330472
X4	-1169.440491	389.99107	-2.9986	0.09554	-2847.437	508.55565	-2847.43663	508.5556491
X5	-0.00110596	0.00162793	-0.6794	0.56699	-0.00811	0.0058985	-0.00811037	0.005898453
X6	0.000239473	7.8301E-05	3.05837	0.09234	-9.74E-05	0.0005764	-9.7428E-05	0.000576373

The regression model developed is given by equation 4.4:

$$R_a = 42.338 - 0.005961C + 0.520F + 0.201D - 1169.440A_e - 1.106 \times 10^{-3}P_f + 2.395 \times 10^{-4}P_r \quad (4.4)$$

Where

R_a = surface roughness (nm)

C = Spindle Speed (rpm)

F = Feed (mm/min)

D = Depth of cut (μm)

A_e = Acoustic emission root mean square (V)

P_f = Prominent Frequency (Hz)

P_r = Peak rate (min^{-1})

Table 4.6 shows the predicted surface roughness values and the corresponding absolute errors.

Table 4. 6: Regression Model Prediction Results

Exp. No.	Observed R_a (nm)	Predicted R_a (nm)	Residuals	Absolute Error (%)
1	16	16.06	-0.06	0.38
2	21	21.74	-0.74	3.52
3	29	28.75	0.32	1.10
4	14	13.47	0.25	1.79
5	20	19.80	0.20	1.00
6	21	20.83	0.17	0.81
7	11	11.25	-0.25	2.27
8	14	13.91	0.09	0.64
9	17	17.20	-0.20	1.18
MAPE				1.41
Prediction Accuracy				98.59

From regression, R square (R^2) equals 0.995. It means that 99.5% of the variance of Y is explained by x. The adjusted R^2 value equals 0.981 while the multiple correlation (R) equals 0.998. This R value means that there is very strong direct relationship between the predicted data (\hat{Y}) and the observed data (Y).

The overall regression is right tailed, $F(1,6) = 70.98$ and p-value is 0.01396. Since p-value $< \alpha(0.05)$, H_0 is rejected. The linear regression model given by H_1 therefore provides a better fit than the model without the independent variables. The MAPE value for water coolant-based results is 1.41%. This means that the prediction accuracy of the model is 98.59%.

4.4.1.1 Validation of Surface Roughness Prediction Model for Water Coolant Based Results

Table 4.7 is a presentation of validation results for water coolant-based results. During the validation of regression model, cutting and AE signal parameters not used in DOE are input into the model and compared with actual experimental results. For simplicity, the 3 extra data sets in ANFIS training have been utilized for this purpose. The MAPE method has been employed to gauge the regression model accuracy.

Table 4. 7: Validation Results for Water Coolant-based Model

Exp. No.	C (rpm)	F (mm/min)	D (μm)	AE _{rms} (V)	P _f (Hz)	P _r (min ⁻¹)	Exp. R _a (nm)	Predicted R _a (nm)	Abs. Error %
10	1250	7.5	15	3.089e-2	2003.955	6.102e+04	17.48	18.1	3.54
11	1750	15	5	2.761e-2	1410.656	3.234e+04	17.14	14.6	14.81
12	2500	22.5	25	2.721e-2	1397.881	3.513e+04	19.71	19.2	2.58
MAPE									6.97
Prediction Accuracy									93.03

The MAPE value for validation of water coolant-based model is 6.97%. This means that the prediction accuracy of the model is 93.03%. The high prediction accuracy indicates the validity of the model.

4.4.2 Surface Roughness Prediction Regression Model for Kerosene Coolant Based Results

The null hypothesis H_0 and the alternative hypothesis H_1 are formulated as follows:

$$H_0: R_a = b_0 \quad (4.5)$$

$$H_1: R_a = b_0 + b_1x_1 + \dots + b_px_p \quad (4.6)$$

The Excel based statistical regression analysis results are shown in Table 4.7.

Table 4. 8: Regression Model Computation Results

SUMMARY OUTPUT								
Regression Statistics								
Multiple R	0.985111926							
R Square	0.970445507							
Adjusted R Square	0.881782027							
Standard Error	2.814356794							
Observations	9							
ANOVA								
	<i>df</i>	<i>SS</i>	<i>MS</i>	<i>F</i>	<i>Significance F</i>			
Regression	6	520.1587917	86.69313195	10.94526758	0.08606889			
Residual	2	15.84120832	7.920604161					
Total	8	536						
	<i>Coefficients</i>	<i>Standard Error</i>	<i>t Stat</i>	<i>P-value</i>	<i>Lower 95%</i>	<i>Upper 95%</i>	<i>Lower 95.0%</i>	<i>Upper 95.0%</i>
Intercept	25.45083303	29.53608054	0.861686201	0.479673944	-101.6326645	152.5343306	-101.6326645	152.5343306
X1	-0.011814521	0.002172058	-5.439320453	0.03217707	-0.021160134	-0.002468909	-0.021160134	-0.002468909
X2	0.622659908	0.271704757	2.291678348	0.148997056	-0.546391305	1.79171112	-0.546391305	1.79171112
X3	0.13843923	0.187119297	0.739844753	0.536452161	-0.666670125	0.943548586	-0.666670125	0.943548586
X4	363.1627594	929.7408994	0.390606415	0.733767917	-3637.189459	4363.514978	-3637.189459	4363.514978
X5	0.002147002	0.003629684	0.591511961	0.614130816	-0.013470269	0.017764272	-0.013470269	0.017764272
X6	-0.000157291	0.000118234	-1.330331011	0.314824733	-0.000666012	0.000351431	-0.000666012	0.000351431

The regression model developed is given by equation 4.7:

$$R_a = 25.451 - 1.182 \times 10^{-2}C + 6.227 \times 10^{-1}F + 1.384 \times 10^{-1}D + 363.163 A_e + 2.147 \times 10^{-3}P_f - 1.573 \times 10^{-4}P_r \quad (4.7)$$

Where

R_a = Surface Roughness (nm)

C = Spindle Speed (rpm)

F = Feed (mm/min)

D = Depth of cut (μm)

A_e = Acoustic emission root mean square (V)

P_f = Prominent Frequency (Hz)

P_r = Peak rate (min^{-1})

Table 4.9 shows the predicted surface roughness values and the corresponding absolute errors.

Table 4. 9: Regression Model Prediction Results

Exp. No.	Observed R_a (nm)	Predicted R_a (nm)	Residuals	Absolute Error (%)
1	21	21.45	-0.45	2.14
2	33	31.68	1.32	4.00
3	38	36.74	1.26	3.32
4	17	16.44	0.56	3.29
5	23	26.21	-3.21	13.96
6	26	26.91	-0.91	3.50
7	12	11.25	0.75	6.25
8	18	17.84	0.16	0.89
9	19	18.49	0.51	2.68
MAPE (%)				4.45
Prediction accuracy				95.55

The R square (R^2) value equals 0.97. It means that 97.0% of the variance of Y is explained by x. The adjusted R square value equals 0.88 while the multiple correlation (R) equals 0.985. The high value of the multiple correlation (R) signifies a strong direct relationship between the predicted data (\hat{Y}) and the observed data (Y).

The overall regression model is right tailed, $F(1,6)=10.945$ and the p-value is 0.086. Since p-value $< \alpha$ (0.05); H_0 is rejected. Therefore, the linear regression model given by equation 4.6 provides a better fit than the model without the independent variables. The mean absolute percentage error for the model is 4.45%. This means that the model's prediction accuracy is 95.55%. Figure 4.6

presents series plots of Absolute Error Values for either coolant. It is seen that the absolute errors for water-based experiments are lower than Kerosene based results.



Figure 4. 6: Series Plots of Absolute Error Values

4.4.2.1 Validation of Surface Roughness Prediction Model for Kerosene Coolant Based Results

Table 4.10 is a presentation of validation results for kerosene coolant-based results. During the validation of regression model, cutting and AE signal parameters not used in DOE are input into the model and compared with actual experimental results. For simplicity, the 3 extra data sets in ANFIS training have been utilized for this purpose. The MAPE method has been employed to gauge the regression model accuracy.

Table 4. 10: Validation Results for Kerosene Coolant-based Model

Exp. No.	C (rpm)	F (mm/min)	D (μm)	AE _{rms} (V)	P _t (Hz)	P _r (min^{-1})	Exp. R _a (nm)	Pred. R _a (nm)	Abs. Error %
10	1250	7.5	15	3.089e-2	2003.955	61017	24	23.34	2.75
11	1750	15	5	2.761e-2	1410.656	32340	23	22.77	1.00
12	2500	22.5	25	2.721e-2	1397.881	35129	22	20.73	5.77
MAPE									3.17
Prediction Accuracy									96.83

The MAPE value for validation of water coolant-based model is 3.17%. This means that the prediction accuracy of the model is 96.83%. The high prediction accuracy indicates the validity of the model.

4.5 ANFIS Prediction of Surface Roughness

The input parameters to the ANFIS model are three cutting parameters and three signal parameters represented in Table 4.3 and Table 4.4. For either coolant, L9 orthogonal array has been used. However, for the purpose of improving the accuracy of the ANFIS model, 3 extra data sets have been included for either coolant. It should be noted that the extra data sets were not part of the L9 orthogonal array used in this research but were obtained from interpolation. In this research, the 12 data sets were divided into 6 training data sets and 6 testing data sets. It is crucial to ensure that the selected testing data set is representative of the present total data as well as all future data. This selection was very difficult, particularly for the small data sets used in this research. The approach taken in this research in selecting training data set was to choose the data with the largest range of surface roughness from the highest to the lowest. The other concern was the selection of the proper size of training and testing data sets. Ideally, neural networks perform better with larger training data sets. This is not possible with the small data set available.

Prior to ANFIS modelling, the data is normalized by min-max normalization method. This method performs a linear alteration on the original data. The values are normalized in the range [0, 1]. The computation is given by equation 4.8.

$$Z = \frac{\gamma - \min_a}{\max_a - \min_a} \quad (4.8)$$

Where Z = normalized value

γ = new value in the required range

\min_a = minimum value in the required range

\max_a = maximum value in the required range

4.5.1 ANFIS Modelling of Water Coolant Based Results

Table 4.11 is a presentation of 3 extra data sets introduced for the purposes of increasing the accuracy of the ANFIS model during training. The experiment numbers of the extra data sets are named 10, 11, and 12. Results at each modelling stage are presented. Experimental data was normalized before it was imported into the MATLAB environment from Notepad. Table 4.12 is a presentation of the normalized data.

Table 4. 11: Extra Data Sets for ANFIS Training (Water Coolant Based Results)

Experiment Number	Spindle Speed (rpm)	Feed (mm/min)	Depth of Cut (μm)	$A E_{\text{rms}}$ (V)	Peak Frequency (Hz)	Peak Rate (min^{-1})	R_a (nm)
10	1250	7.5	15	3.089e-2	2003.955	6.102e+04	17.48
11	1750	15	5	2.761e-2	1410.656	3.234e+04	17.14
12	2500	22.5	25	2.721e-2	1397.881	3.513e+04	19.71

Table 4. 12: Normalized ANFIS Data (Water Coolant Based Results)

Experiment Number	Spindle Speed (rpm)	Feed (mm/min)	Depth of Cut (μm)	AE _{rms} (V)	Peak Frequency (Hz)	Peak Rate (min ⁻¹)	R _a (nm)
1	0.00	0.00	0.00	0.95	1.00	8.86E-01	0.28
2	0.00	0.50	0.50	0.60	0.54	4.90E-01	0.56
3	0.00	1.00	1.00	1.00	1.00	1.00E+00	1.00
4	-0.40	0.00	0.50	0.55	0.61	3.44E-01	0.17
5	-0.40	0.50	1.00	0.52	0.61	3.46E-01	0.50
6	-0.40	1.00	0.00	0.49	0.04	3.39E-01	0.56
7	0.00	0.00	1.00	0.48	0.52	2.87E-01	0.00
8	-1.00	0.50	0.00	0.00	0.00	0.00E+00	0.17
9	-1.00	1.00	0.50	0.58	0.61	3.98E-01	0.33
10	0.00	0.00	0.50	0.95	1.00	8.86E-01	0.36
11	-0.40	0.50	0.00	0.62	0.61	3.46E-01	0.34
12	-1.00	1.00	1.00	0.58	0.61	3.98E-01	0.48

Once the imported data was in the MATLAB workspace, it was loaded to the ANFIS graphical user interface. Figure 4.7 shows the screen shot of the data loading stage from the MATLAB workspace to the ANFIS graphical user interface. The following experiment numbers were used during the model training stage: 2,3,9,10,11 and 12.

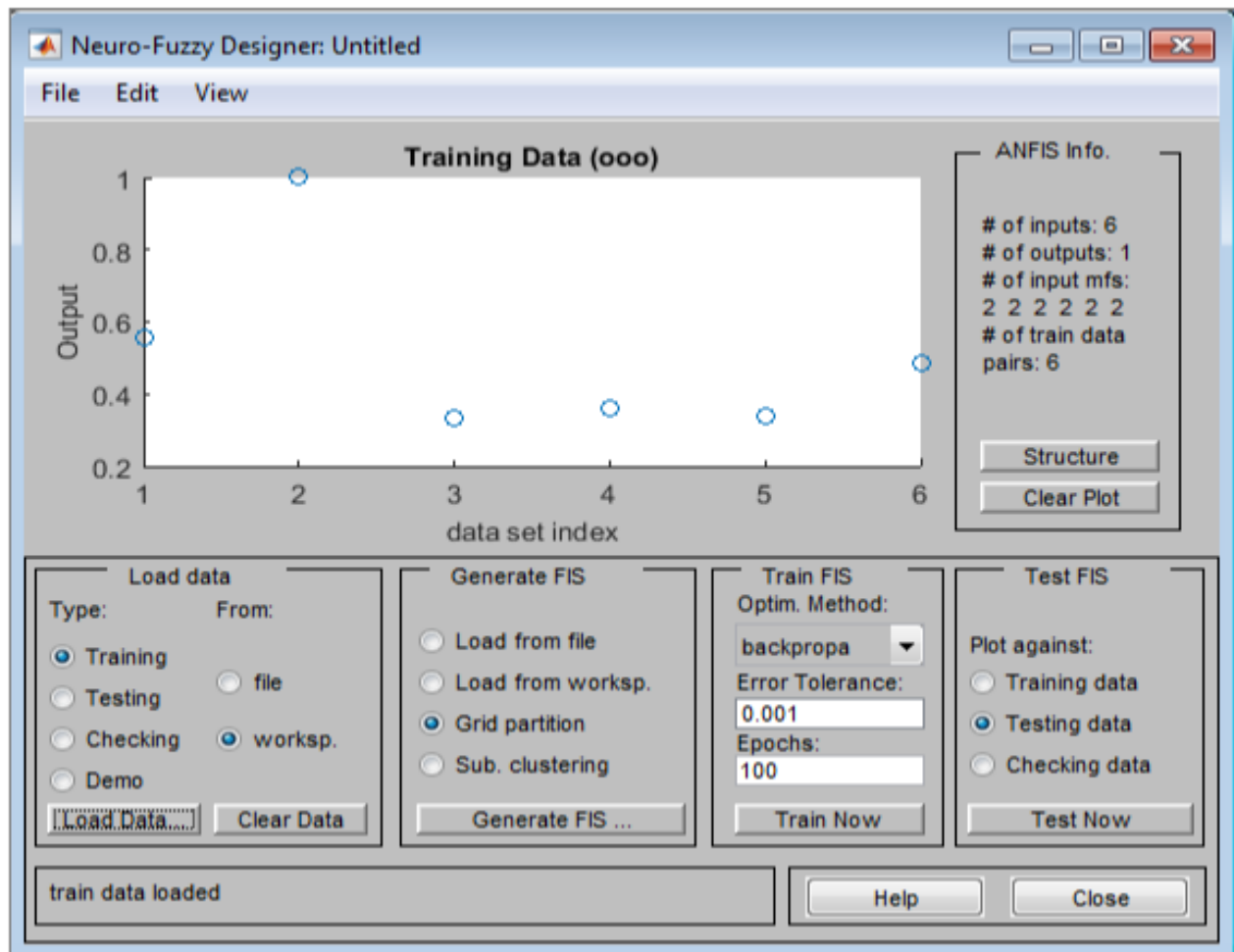


Figure 4. 7: ANFIS Model Training Data Loading Stage

During the FIS generating stage, the dsigmf membership function with the number [2 2 2 2 2 2] was selected as it yielded the least error after trying different membership function shapes. Figure 4.8 shows the Fuzzy Inference System (FIS) generating stage.

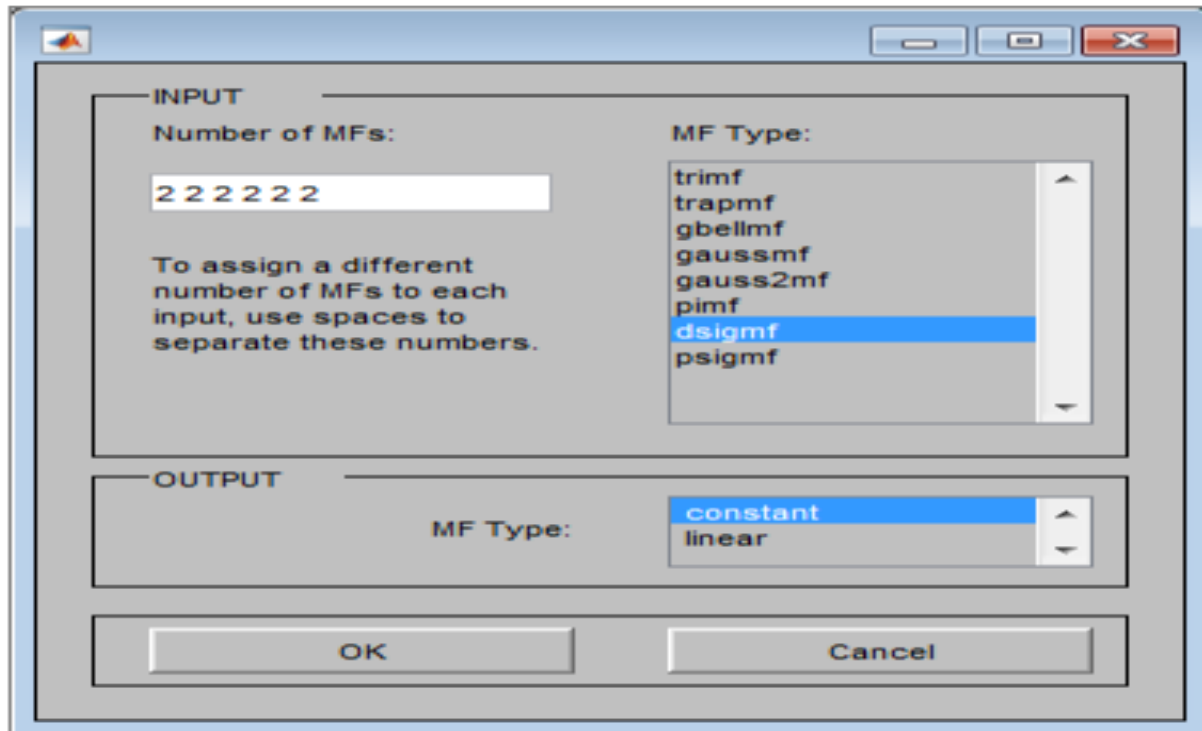


Figure 4. 8: Fuzzy Inference System (FIS) Generating Stage

The FIS training stage screen shot is shown in Figure 4.9. It is observed that epoch 91 error is $3.3006e-05$. The curve shows the error reduction of each epoch for the 100 epochs used in this study. It is observed that the minimum error target was reached at epoch 90, after which there was no further error reduction.

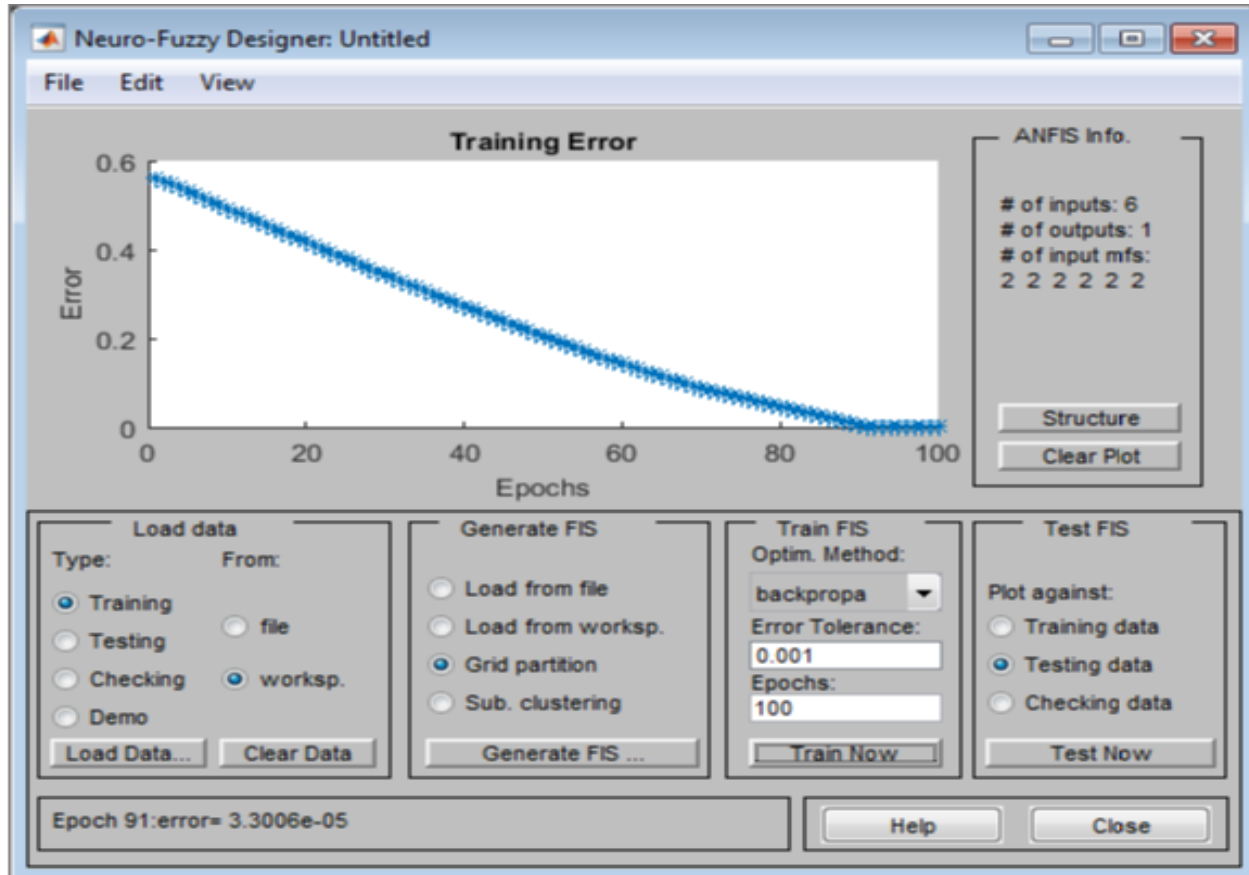


Figure 4. 9: Fuzzy Inference System Training Stage

The FIS test plot against training data is shown in Figure 4.10. The experimental values of surface roughness are shown by the blue dots while predicted values are shown by red dots. The overlapping of plots depicts high prediction accuracy. It is observed from this figure that all predicted outputs for training data are very close to the experimental outputs of training data.

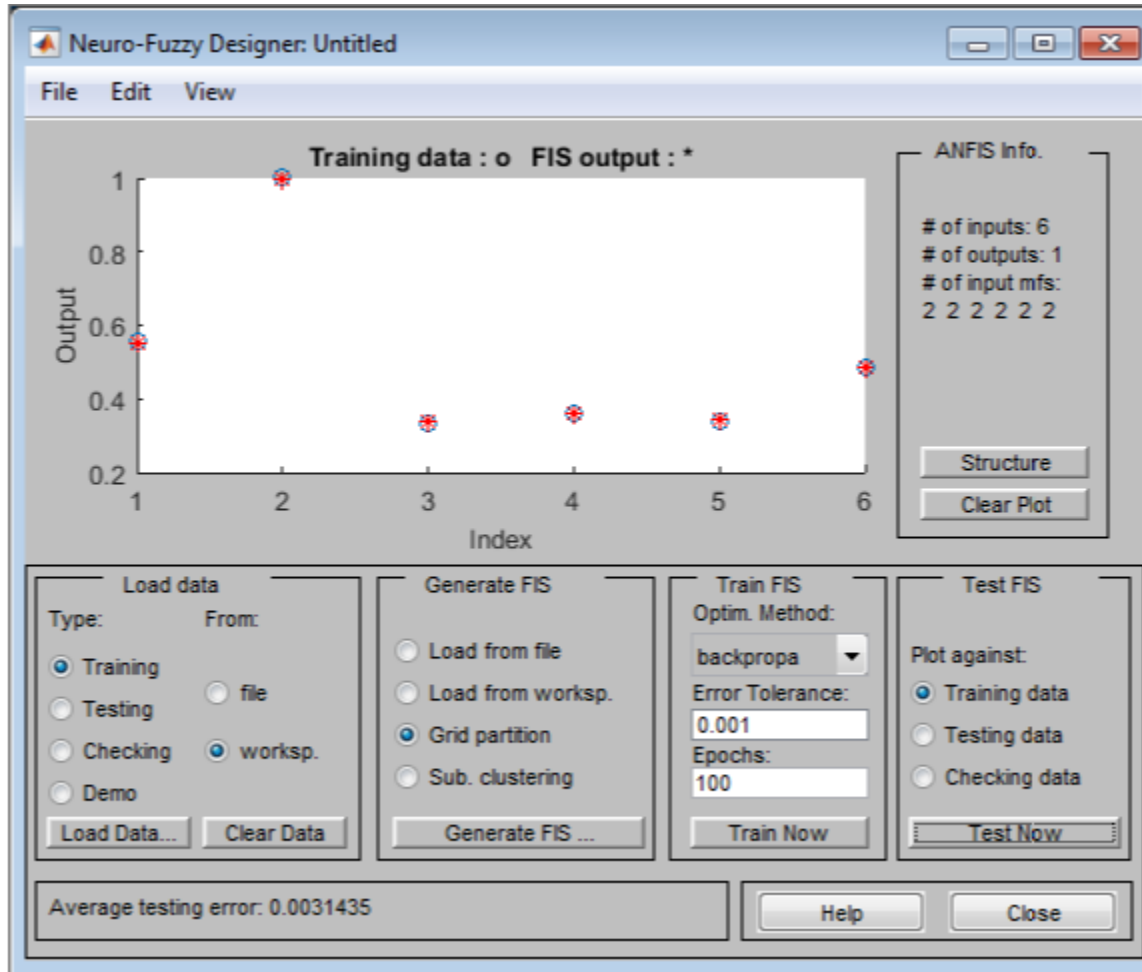


Figure 4. 10: Training Set Stage Results (Water Coolant)

The FIS test plot against testing data is shown in Figure 4.11. This is done to validate the ANFIS model. The experimental values of surface roughness are shown by the blue dots while predicted values are shown by red dots. The slight divergence of the blue dots from the red dots indicates the presence of some marginal error in the ANFIS prediction model.

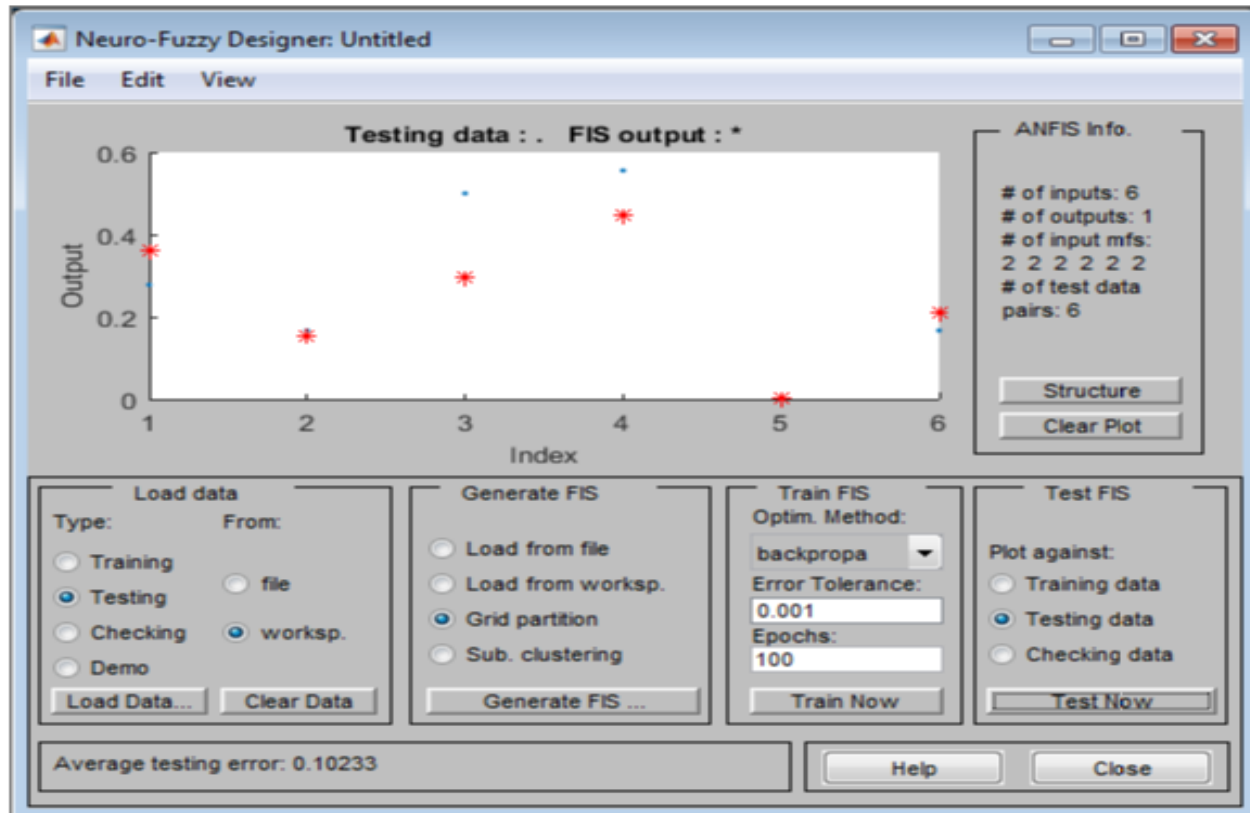


Figure 4. 11: Testing Set Sample Results (Water Coolant)

The surface plot of the predicted results is shown in Figure 4.12. It is evident that the surface occupies the entire area of the decision space. In the 3D ANFIS Surface Viewer, low (better) surface roughness values are represented by the blue color close to the floor. The yellow color represents high surface roughness values. Overall, the 3D surface plots show that the surface roughness values are low in the speed range of -0.5 to -1 and the feed range of 0 to 0.5.

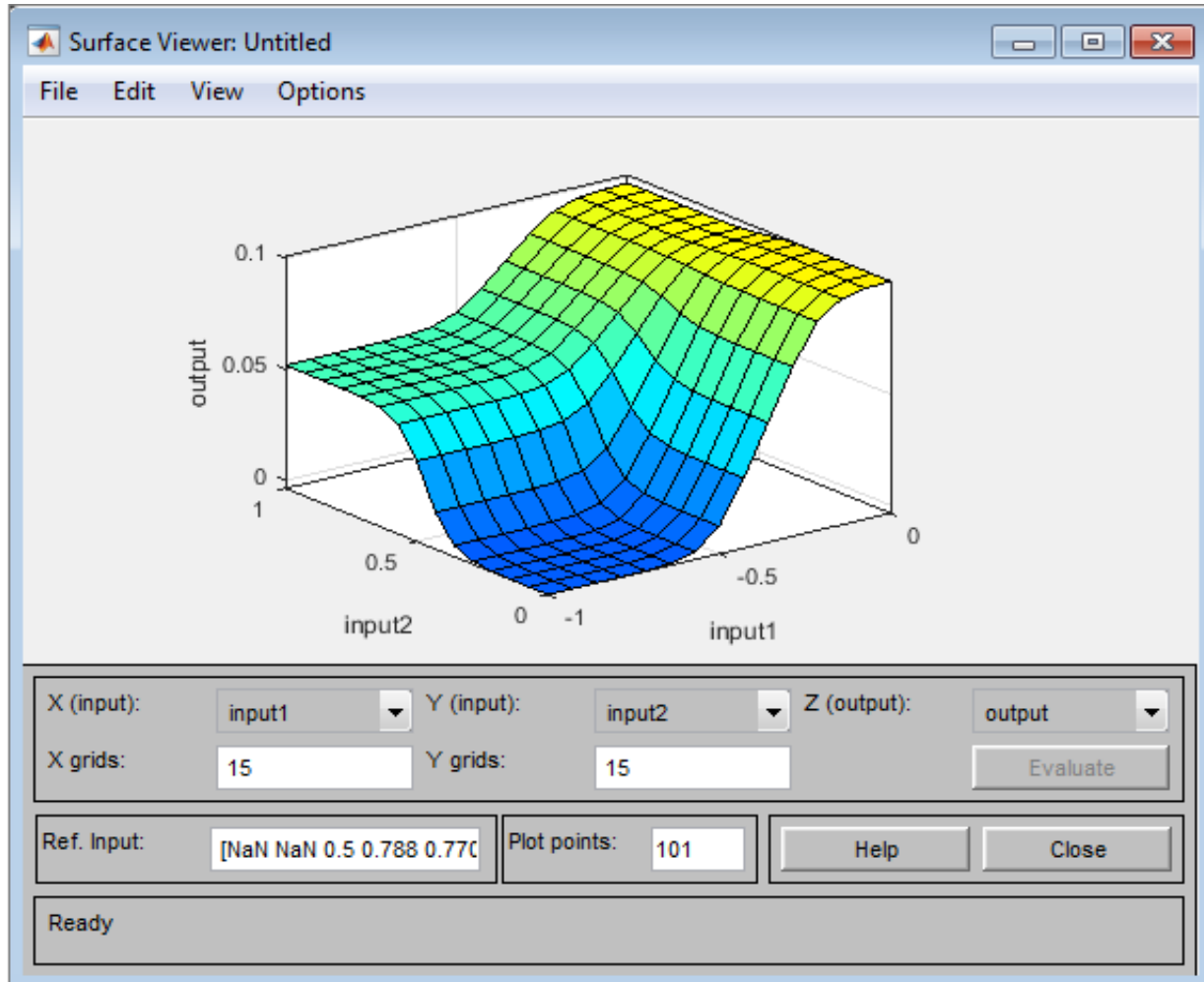


Figure 4. 12: ANFIS Surface Viewer

The rule viewer in Figure 4.13 shows the ANFIS results for the training set using normalized data. It shows that the surface roughness value is 0.0405 nm for the following set of parameters (-0.5; 0.5; 0.5; 0.788; 0.771; 0.673).

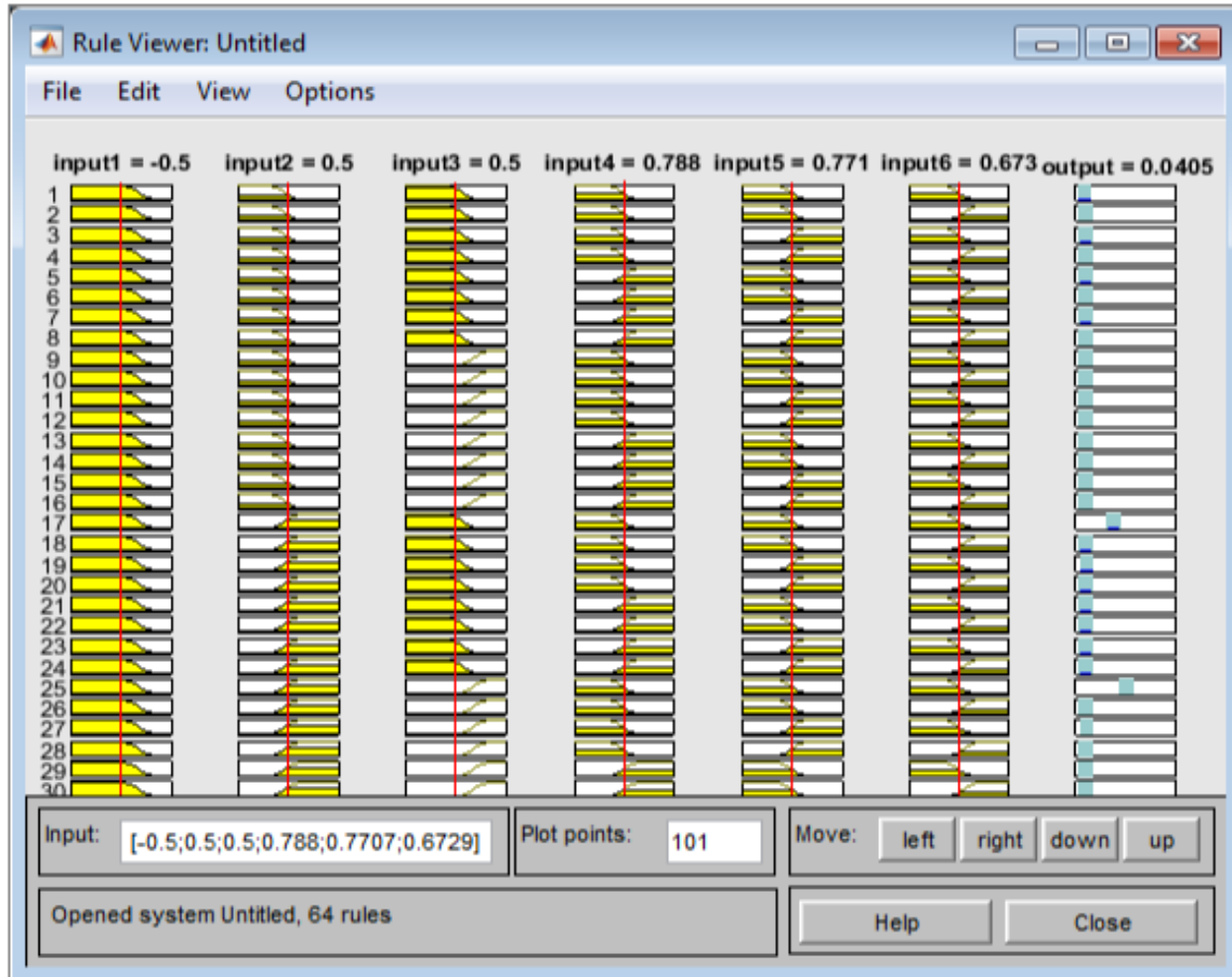


Figure 4. 13: ANFIS Rule Viewer

The ANFIS learning information is shown in Table 4.13.

Table 4. 13: ANFIS Learning Information

Learning Scenario	Value
Number of Nodes	161
Number of linear Parameters	64
Number of Non-Linear Parameters	48
Total Number of Parameters	112
Number of Training Data Pairs	6
Minimal Training RSME	0.000001
Number of Fuzzy Rules	64

The membership function that gave the best results was the dsigmf, hence its use during the prediction stage. The minimum number of membership functions used was two as a way of reducing the complexity of the ANFIS model. The results of the ANFIS model prediction for surface roughness using water as a coolant are represented by Table 4.14. The training stage results are validated by comparison to testing stage results.

Table 4. 14: Comparison of ANFIS results with experimental findings (Water Coolant)

Training Data Set			
Experiment Number	Measured R_a (nm)	Predicted R_a (nm)	Absolute Error (%)
2	0.56	0.55	1.79
3	1.00	1.00	0.00
9	0.33	0.34	3.03
10	0.36	0.36	0.00
11	0.34	0.34	0.00
12	0.48	0.48	0.00
Average Absolute Error (%)			0.80
Prediction Accuracy (%)			99.20

Testing Data Set			
Experiment Number	Measured R_a (nm)	Predicted R_a (nm)	Absolute Error (%)
1	0.28	0.36	28.57
4	0.17	0.15	11.76
5	0.50	0.30	40.00
6	0.56	0.45	19.64
7	0.00	0.00	0.00
8	0.17	0.21	23.53
Average Absolute Error (%)			20.58
Prediction Accuracy			79.42

The low percentage errors in the ANFIS results are very good. The ANFIS model's prediction accuracy for training and testing data is 99.20% and 79.42% respectively. This indicates a high prediction accuracy of ANFIS model in predicting surface roughness of small data sets.

4.5.2 ANFIS Modelling of Kerosene Coolant Based Results

Table 4.15 is a presentation of 3 extra data sets introduced for the purposes of increasing the accuracy of the ANFIS model during training using kerosene coolant-based results. Table 4.16 is a representation of the normalized data obtained using kerosene coolant.

Table 4. 15: Extra Data Sets for ANFIS Training (Kerosene Coolant Based Results)

Experiment Number	Spindle Speed (rpm)	Feed (mm/min)	Depth of Cut (μm)	AE_{rms} (V)	Peak Frequency (Hz)	Peak Rate (min^{-1})	R_a (nm)
10	1250	7.5	15	3.089e-2	2003.955	61017	24
11	1750	15	5	2.761e-2	1410.656	32340	23
12	2500	22.5	25	2.721e-2	1397.881	35129	22

Table 4. 16: Normalized Data (Kerosene Coolant Based Results)

Experiment Number	Spindle Speed (rpm)	Feed (mm/min)	Depth of Cut (μm)	AE_{rms} (V)	Peak Frequency (Hz)	Peak Rate (min^{-1})	R_a (nm)
1	0.00	0.00	0.00	0.32	0.00	0.90	0.35
2	0.00	0.50	0.50	0.00	0.05	0.00	0.81
3	0.00	1.00	1.00	0.11	1.00	0.78	1.00
4	0.40	0.00	0.50	0.04	0.07	0.90	0.19
5	0.40	0.50	1.00	0.05	0.39	0.40	0.42
6	0.40	1.00	0.00	0.13	1.00	1.00	0.54
7	1.00	0.00	1.00	0.05	0.50	0.72	0.00
8	1.00	0.50	0.00	1.00	1.00	0.57	0.23
9	1.00	1.00	0.50	0.12	0.52	0.90	0.27
10	0.00	0.00	0.50	0.95	1.00	0.89	0.22
11	0.40	0.50	0.00	0.62	0.61	0.35	0.67
12	1.00	1.00	1.00	0.58	0.61	0.40	0.61

Once the imported data was in the MATLAB workspace, it was loaded to the ANFIS graphical user interface. Figure 4.14 shows the screen shot of the data loading stage from the MATLAB workspace to the ANFIS graphical user interface. The following experiment numbers were used during the model training stage: 1,2,3,10,11 and 12.

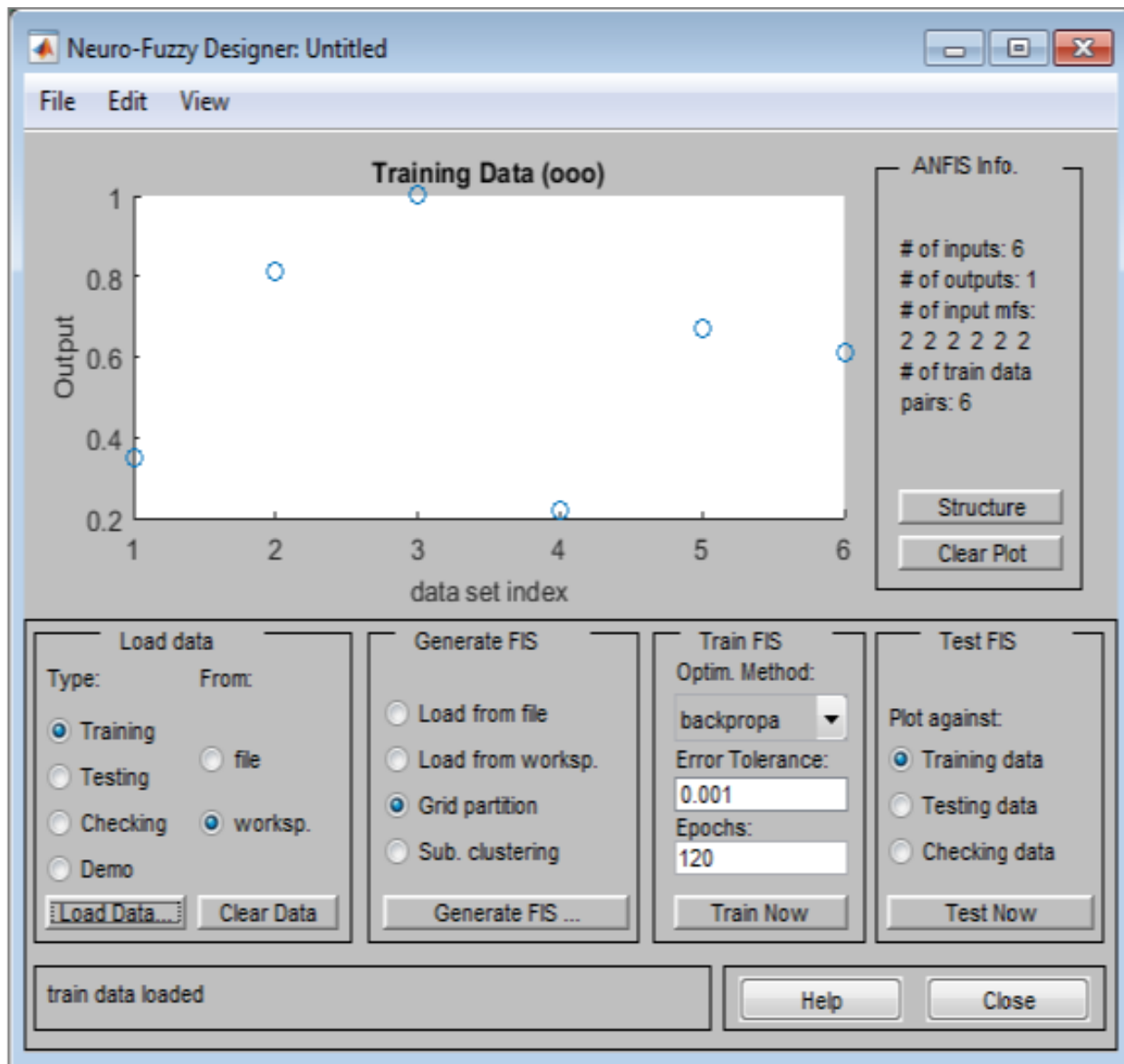


Figure 4. 14: ANFIS Model Data Loading Stage

The FIS generation stage is shown by Figure 4.15. At this stage, a gbellmf is utilized as it has the least errors after trying different membership function shapes. The ANFIS is trained using a tolerance of 0.001 and 120 epochs.

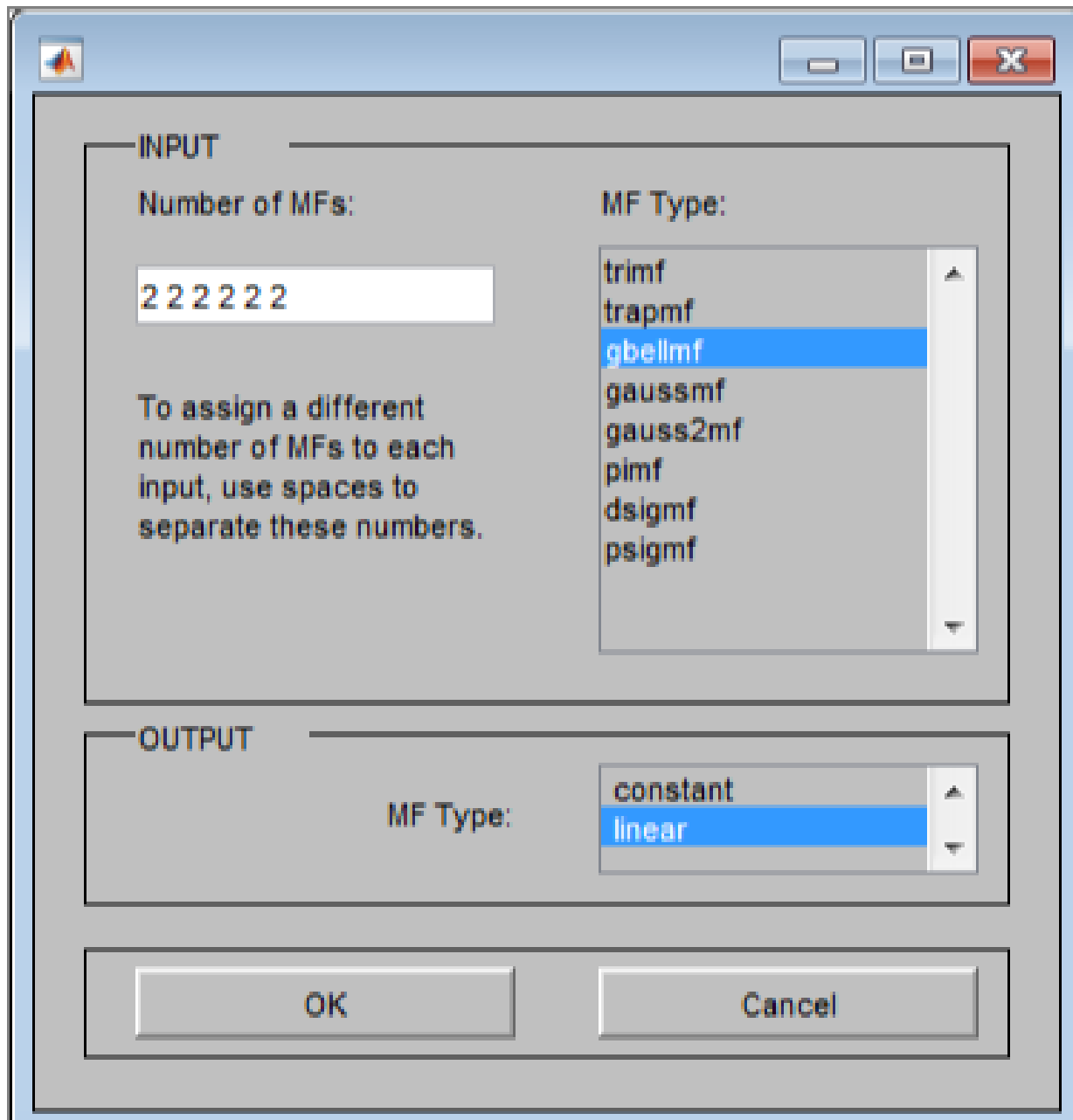


Figure 4. 15: FIS Generation Stage

The FIS training stage screen shot is shown in Figure 4.16. It is observed that epoch 120 error is 0.0062858. The curve shows the error reduction of each epoch for the 120 epochs used in this study. It is observed that the minimum error target was reached at epoch 92, after which there was no further error reduction.

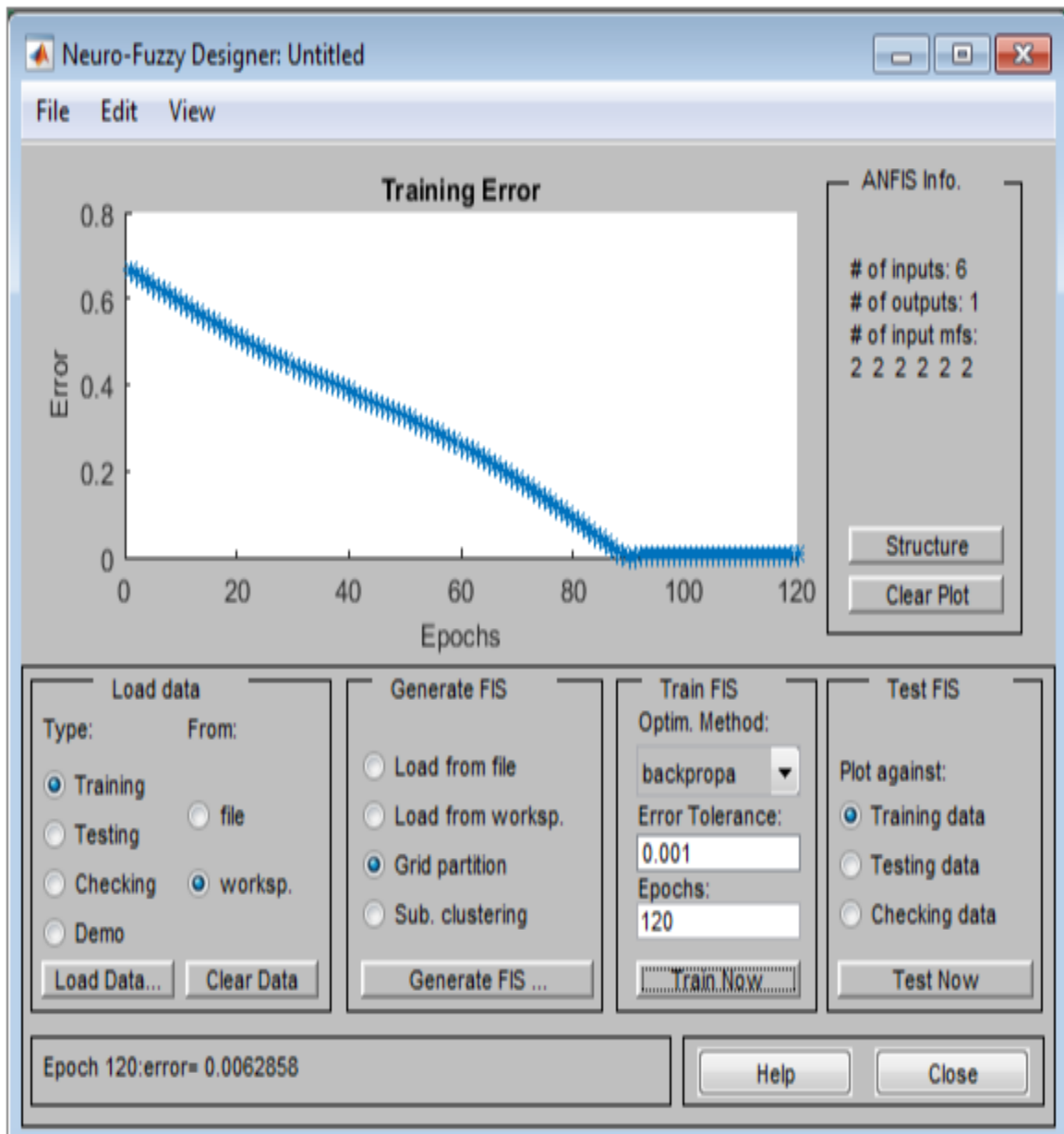


Figure 4. 16: ANFIS Training Stage

The FIS test plot against training data is shown in Figure 4.17. The experimental values of surface roughness are shown by the blue dots while predicted values are shown by red dots. The overlapping of plots depicts high prediction accuracy. It is observed from this figure that all predicted outputs for training data are very close to the experimental outputs of training data.

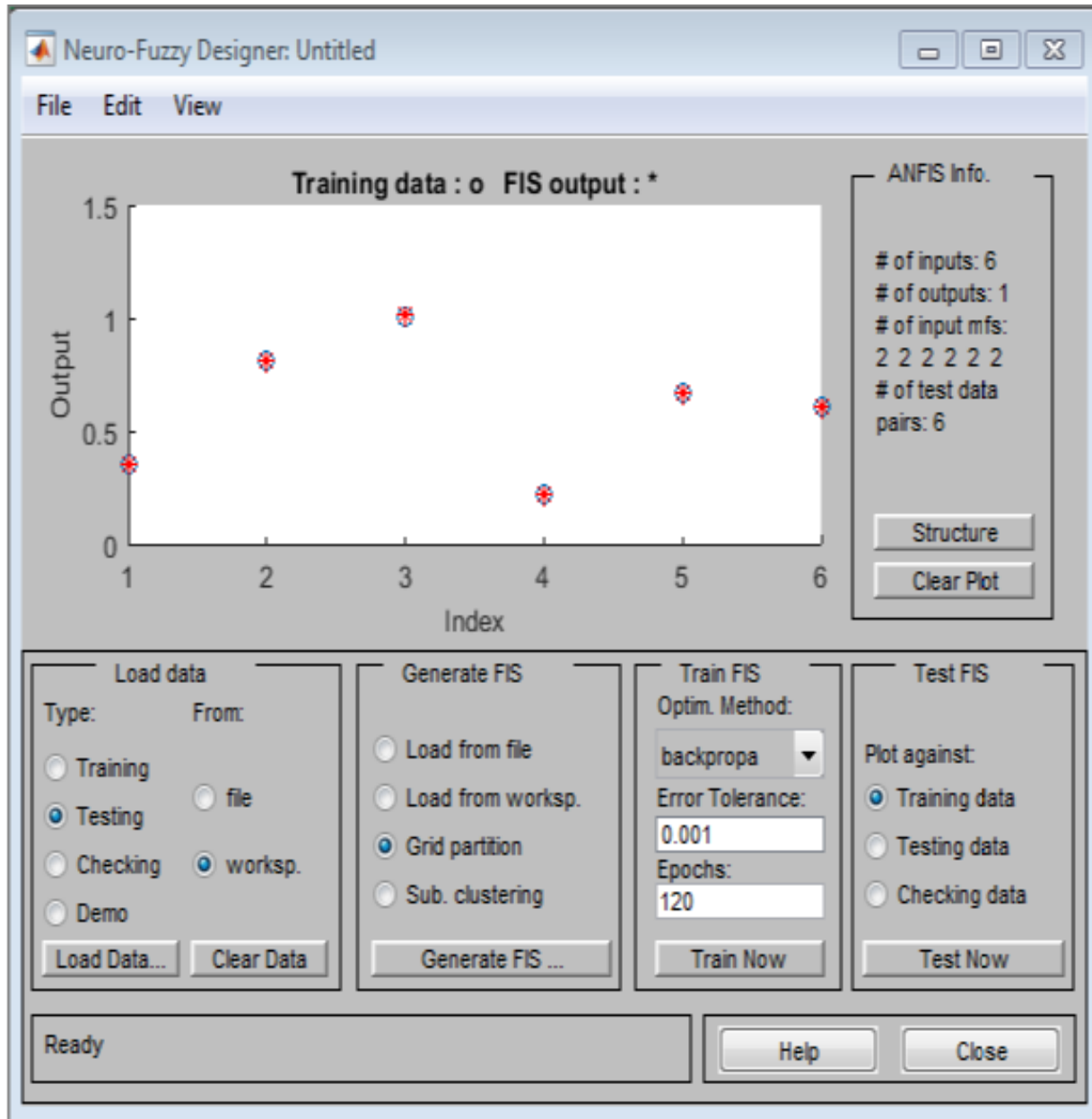


Figure 4. 17: Training Set Stage Results (Kerosene Coolant)

The FIS test plot against testing data is shown in Figure 4.18. This is done to validate the ANFIS model. The experimental values of surface roughness are shown by the blue dots while predicted values are shown by red dots. The slight divergence of the blue dots from the red dots indicates the presence of some marginal error in the ANFIS prediction model.

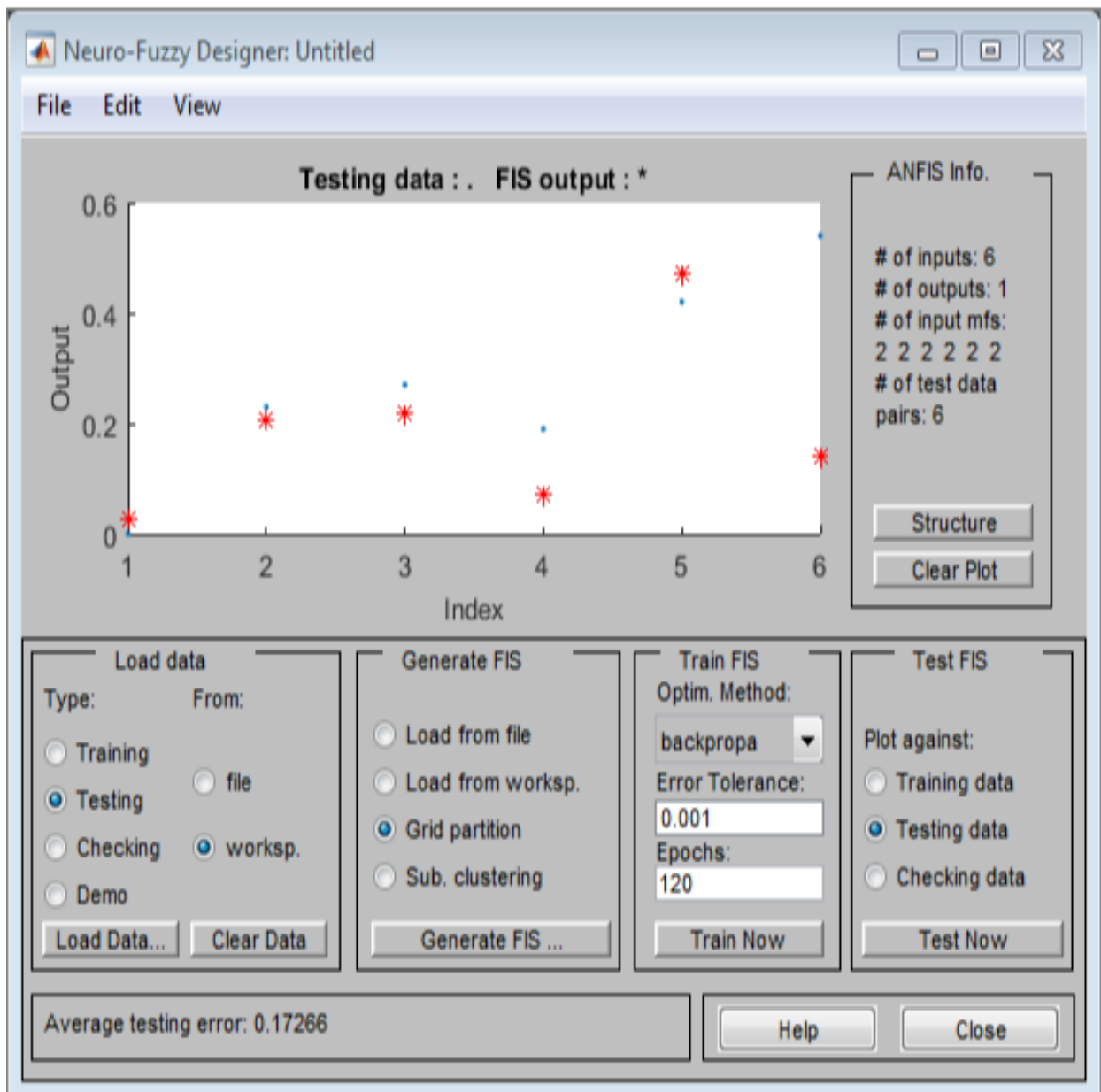


Figure 4. 18: Testing Set Stage Results (Water Coolant)

The rule viewer in Figure 4.19 shows the ANFIS results for the training set using normalized data. It shows that the surface roughness value is 0.177 nm for the following set of parameters (0.5; 0.5; 0.5; 0.475; 0.5; 0.45).

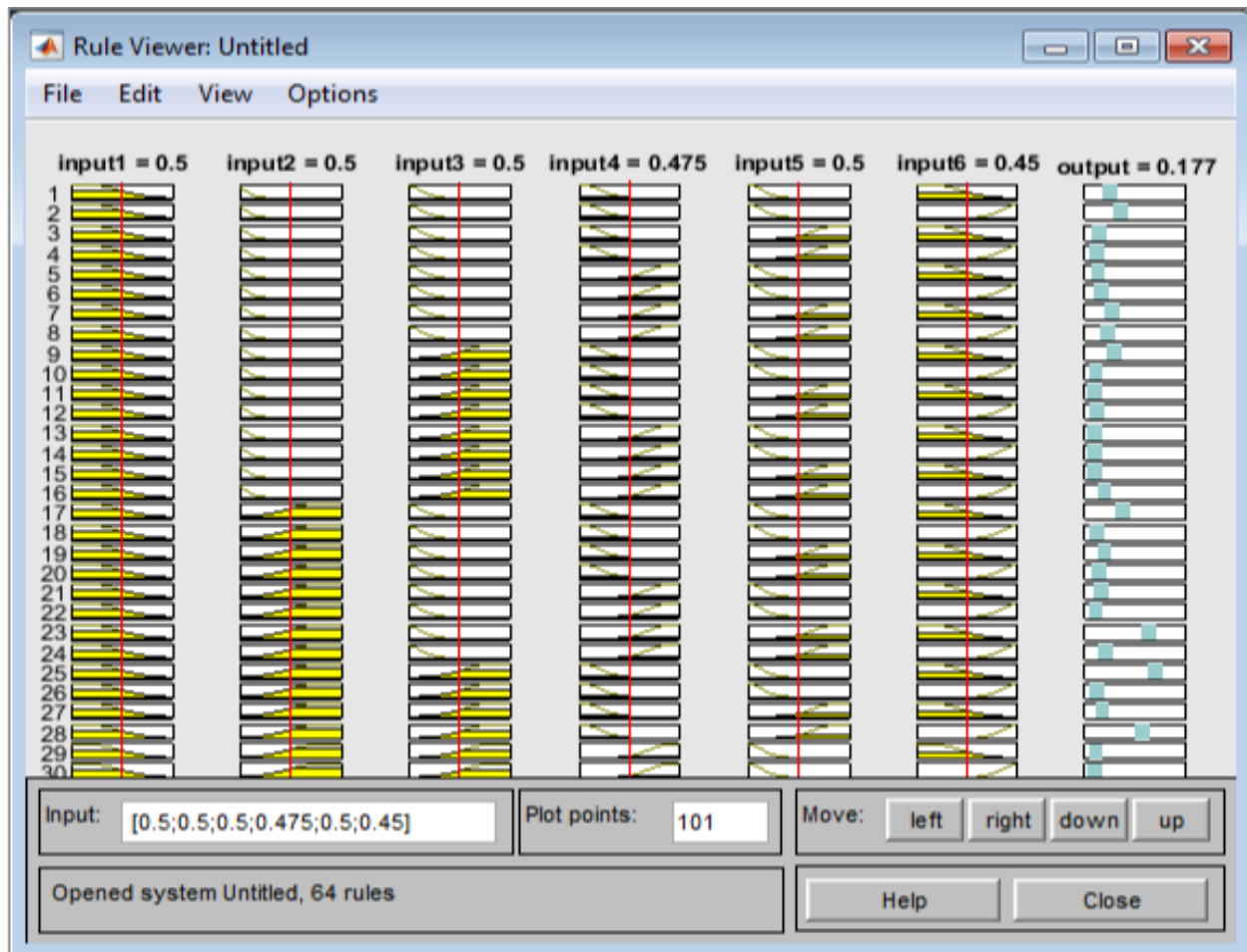


Figure 4. 19: ANFIS Rule Viewer

The surface plot of the predicted results is shown in Figure 4.20. It is evident that the surface occupies the entire area of the decision space. In the 3D ANFIS Surface Viewer, low (better) surface roughness values are represented by the blue color close to the floor. The yellow color represents high surface roughness values. Overall, the 3D surface plots show that the surface roughness values are low in the speed range of 0 to 1 and the feed range of 0 to 0.5.

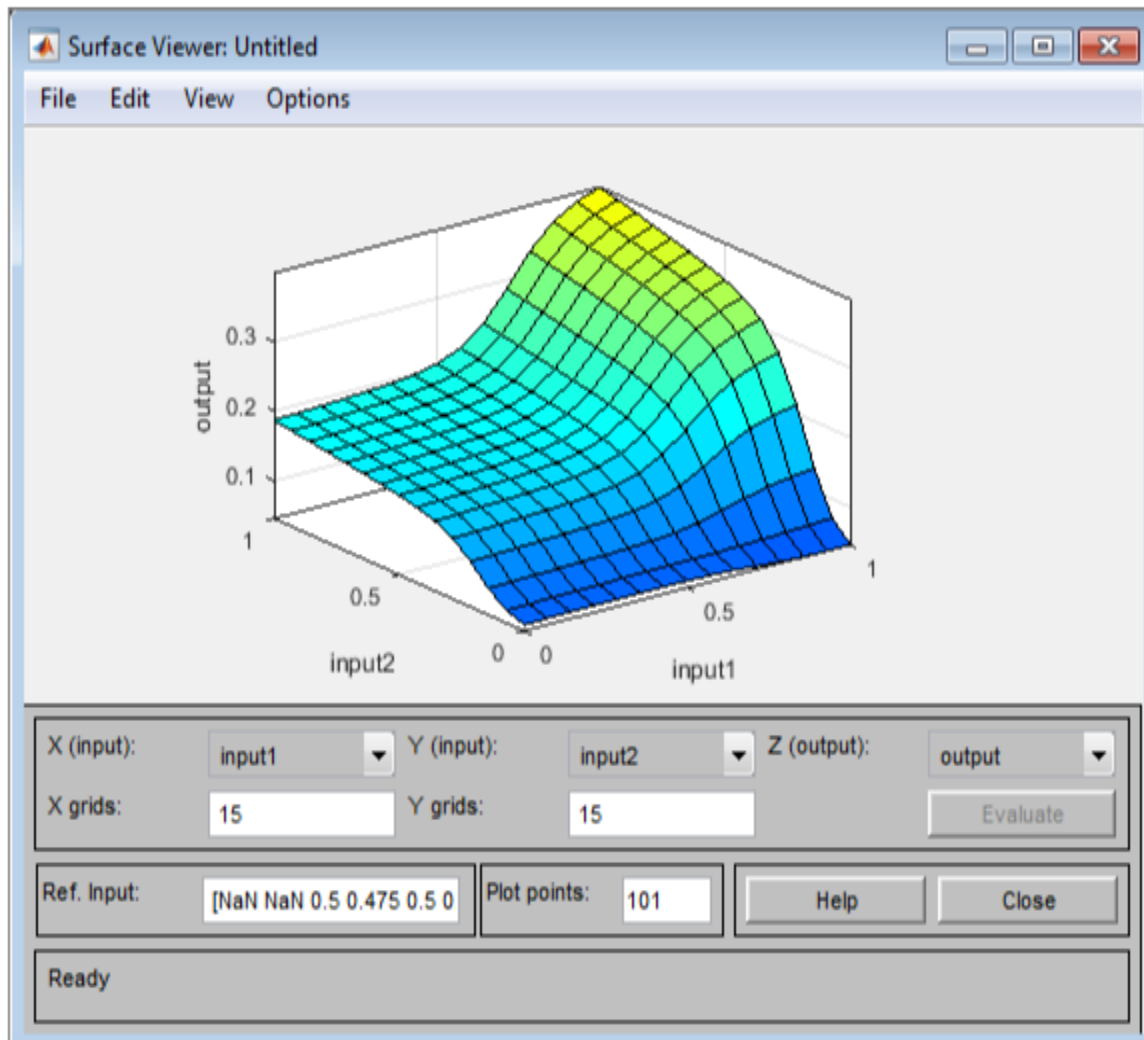


Figure 4. 20: ANFIS Surface Viewer

The results of the ANFIS model prediction for surface roughness using water as a coolant are represented by Table 4.17. The training stage results are validated by comparison to testing stage results.

Table 4. 17: Comparison of ANFIS results with experimental findings (Kerosene Coolant)

Training Data Set			
Experiment Number	Measured R_a (nm)	Predicted R_a (nm)	Absolute Error (%)
1	0.35	0.35	0.00
2	0.81	0.81	0.00
3	1.00	1.01	1.00
10	0.22	0.22	0.00
11	0.67	0.67	0.00
12	0.61	0.61	0.00
Mean Absolute Error (%)			0.17
Prediction Accuracy (%)			99.83

Testing Data Set			
Experiment Number	Measured R_a (nm)	Predicted R_a (nm)	Error (%)
7	0.00	0.03	2.91
8	0.23	0.20	13.04
9	0.27	0.22	18.52
4	0.19	0.07	63.16
5	0.42	0.47	11.90
6	0.54	0.14	74.07
Mean Absolute Error (%)			30.60
Prediction accuracy (%)			69.40

The low percentage errors in the ANFIS results are very good. The training error is 0.17% while the testing error is 30.60%. The values indicate prediction accuracies of 99.83% and 69.40% on training and testing data respectively. These values are as expected, that is, the training error is lower than the testing error. The obtained error values indicate the high accuracy of ANFIS model in predicting surface roughness of small data sets. The slightly higher error value in testing data may be due to the unavailability of data to sufficiently train the ANFIS model.

4.6 Comparison of Regression and ANFIS Models for Water and Kerosene Surface Roughness Results

The Mean Absolute Percentage Error has been used as the performance indicator. It has been computed for both ANFIS and Regression results. The MAPE is calculated by Equation 4.2. Both coolants' modelling results are pictorially represented by Figure 4.22. It is seen that the regression model has a higher accuracy compared to ANFIS model in predicting the surface roughness of single point diamond turned RSA-443.

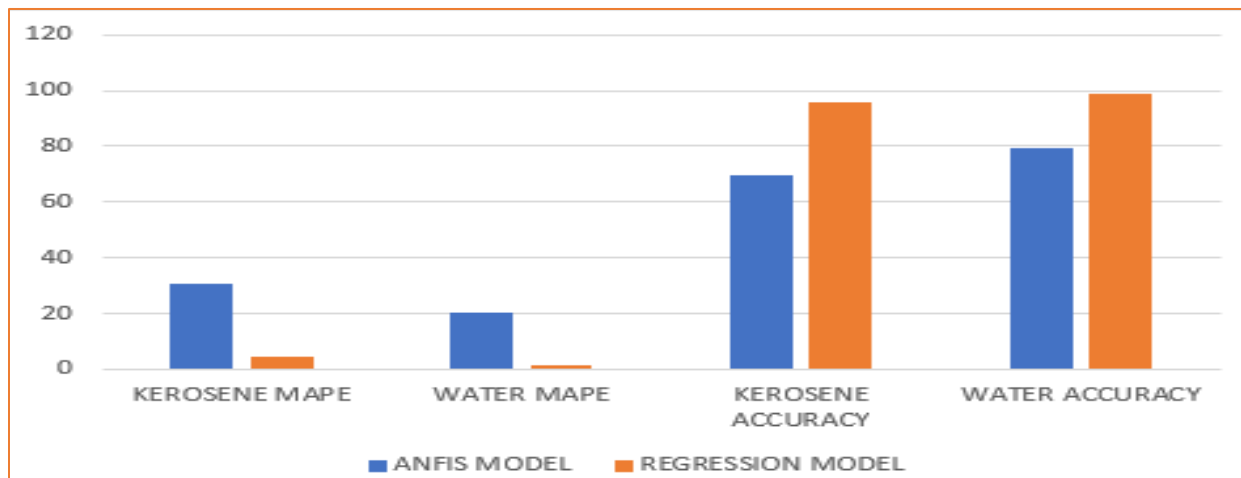


Figure 4. 21: Comparison of Regression and ANFIS Models in Predicting Surface Roughness (Water Coolant)

4.7 Impact of Acoustic Emission Signal Parameters on Prediction Accuracy

The regression model linking the critical machining parameters (cutting speed (C1), feed (C2) and depth of cut (C3) is given by Equation (4.9). Table 18 shows that the use of critical machining parameters alone in the RSM prediction model has a prediction accuracy of 96.35%.

$$R_a = 18.8377 - 0.006351C_1 + 0.5778C_2 + 0.1500C_3 \quad (4.9)$$

Table 4. 18: Surface Roughness Values Based on Critical Machining Parameters

C₁ [rpm]	C₂ [mm/min]	C₃ [μm]	Measured Ra [nm]	Predicted Ra [nm]	Absolute Error (%)
1250	7.5	5	16	15.98	0.13
1250	15.0	15	21	21.82	3.90
1250	22.5	25	29	27.65	4.66
1750	7.5	15	14	14.31	2.21
1750	15.0	25	20	20.14	0.70
1750	22.5	5	21	21.47	2.24
2500	7.5	25	11	11.04	0.36
2500	15.0	5	14	12.38	11.57
2500	22.5	15	17	18.21	7.12
MAPE					3.65
Prediction Accuracy					96.35

Equation 4.10 is a regression model that utilized both critical machining parameters and AE signal parameters in surface roughness prediction. The parameters are C1 (cutting speed), C2 (feed), C3 (depth of cut), X1 (AERms), X2 (prominent frequency) and X3 (peak rate). It is evident from the tabulated results (refer with: Table 4.19) that the use of both critical machining parameters and AE signal parameters has a high prediction accuracy of 97.32%.

$$R_a = 42.393 - 0.006C_1 + 0.523C_2 + 0.179C_3 - 1142.378X_1 - 0.00021X_2 + 0.000199X_3 \quad (4.10)$$

Table 4. 19: Surface Roughness Values Based on Both AE Signal Parameters and Critical Machining Parameters

C ₁ [rpm]	C ₂ [mm/min]	C ₃ [μm]	X ₁ [V]	X ₂ [Hz]	X ₃ [min ⁻¹]	Measured R _a [nm]	Predicted R _a [nm]	Absolute Error (%)
1250	7.5	5	0.031	2003.96	6.10e+04	16	15.91	0.56
1250	15.0	15	0.027	1300.13	4.00e+04	21	22.16	5.52
1250	22.5	25	0.031	2003.96	6.71e+04	29	28.55	1.55
1750	7.5	15	0.027	1407.66	3.23e+04	14	13.65	2.50
1750	15.0	25	0.027	1407.66	3.23e+04	20	19.36	3.20
1750	22.5	5	0.026	527.87	3.20e+04	21	20.96	0.19
2500	7.5	25	0.026	1261.03	2.92e+04	11	11.44	4.00
2500	15.0	5	0.022	469.22	1.40e+04	14	13.48	3.71
2500	22.5	15	0.027	1397.88	3.51e+04	17	17.49	2.88
MAPE								2.68
Prediction Accuracy								97.32

From the study, it can be concluded that the use of AE signal parameters in conjunction with critical machining parameters enhances surface roughness prediction accuracy of a model that solely employs critical machining parameters by 0.97%. The use of a composite model is recommended to enhance prediction accuracy. This result is a confirmation of the reviewed literature which has demonstrated that the effectiveness of soft computing models is dependent on the size of the experimental dataset, and it can be lower compared to that of the regression models for a small-sized dataset. The lower prediction accuracy of ANFIS is due to the small and insufficient data sets available for the ANFIS model training.

4.8 Summary of results

The objectives of this research work were aimed at investigating the accuracy of the ANFIS model in surface roughness prediction during single point diamond turning of RSA-443. Prediction accuracy on training data sets was compared with prediction accuracy on testing data sets for either

coolant (water and kerosene). While both training and testing results were considerably good, the training results for ANFIS model were more accurate than testing results as expected. For water coolant, the training results have a mean absolute error of 0.80%; that is, a prediction accuracy of 99.20%. The mean absolute error for testing results is 20.58%; that is, a prediction accuracy of 79.42%. For kerosene coolant, the training results mean absolute error is 0.17%, that is a prediction accuracy of 99.83%. The mean absolute error for kerosene testing results is 30.60% and a prediction accuracy of 69.40%. The slightly higher values of testing error may be due to the small data sets available for the ANFIS model training.

The Mean Absolute Percentage Error (MAPE) was also used to evaluate ANFIS model relative accuracy to Regression model. For either coolant, it was observed that while both models are accurate, the Regression model is relatively more accurate than the ANFIS model when using small data sets. This result is a confirmation of the reviewed literature which has demonstrated that the effectiveness of soft computing models is dependent on the size of the experimental dataset, and it can be lower compared to that of the regression models for a small-sized dataset. The lower prediction accuracy of ANFIS is due to the small and insufficient data sets available for the ANFIS model training.

CHAPTER FIVE

5.0 CONCLUSION AND RECOMMENDATIONS

5.1 Introduction

The overall aim of this research was to investigate the accuracy of ANFIS model in predicting surface roughness of single point diamond turned RSA443. This chapter presents the conclusion of the investigative research. Suggested recommendations for further study are also highlighted in this chapter.

5.2 Conclusions

In this research, ANFIS and Regression models have been successfully used to predict the surface roughness of single point diamond turned RSA443 using small data sets. A comparison of Regression results and ANFIS results using MAPE suggests that Regression model prediction has produced better results than ANFIS model using small data sets. In this study, the mean absolute percentage error of ANFIS was 19.17% greater than Regression's when using water as a coolant. When using kerosene as a coolant, the mean absolute percentage error of ANFIS was 26.15% greater than Regression's. However, a comparison of ANFIS prediction error in training data sets against testing data sets error reveals that the error is slightly higher in training data sets. This is due to the small data that is not good enough for ANFIS model learning.

Despite the ANFIS model being less accurate than the regression model when using small data sets, its prediction accuracy of above 65% for either coolant is accurate. Due to its capability to be incorporated in online prediction processes, ANFIS can be reliably used to predict the surface roughness of RSA 443 using small data sets.

The result of this study has confirmed what is in the reviewed literature, that is, the effectiveness of soft computing models is dependent on the size of the experimental dataset, and it can be lower compared to that of the regression models for a small-sized dataset. The lower prediction accuracy of ANFIS is due to the small and insufficient data sets available for the ANFIS model training.

5.3 Recommendations

In this research, only Regression model performance has been compared to ANFIS model. Alternative methods such as RSM and GA-ANN can be tried to predict the surface roughness of single point diamond turned RSA443 with the overall goal of reducing production cost and shortening production time. The effectiveness of using only acoustic emission signal parameters, without turning parameters such as spindle speed, feed rate and depth of cut can be investigated. The effect of varying rake angle can be investigated to achieve optimum surface roughness of RSA443. Only three signal parameters have been used in this research, leaving a sea of other parameters that can be included in future studies.

REFERENCES

- [1] U. Natarajan, S. Palani, B. Anandampillai, and M. Chellamalai, "Prediction and comparison of surface roughness in CNC-turning process by machine vision system using ANN-BP and ANFIS and ANN-DEA models," *Int. J. Machining and Machinability of Materials*, vol. 12, 2012.
- [2] S. Palani, U. Natarajan, and M. Chellamalai, "On-line prediction of micro-turning multi-response variables by machine vision system using adaptive neuro-fuzzy inference system (ANFIS)," *Machine Vision and Applications*, vol. 24, pp. 19-32, 2013.
- [3] B. S. Reddy, J. S. Kumar, and K. V. K. Reddy, "Prediction of Surface Roughness in Turning Using Adaptive Neuro-Fuzzy Inference System " *Jordan Journal of Mechanical and Industrial Engineering* vol. 3, pp. 252-259, 2009.
- [4] L. Y. Zhang, Y. H. Jiang, Z. Maa, S. F. Shanc, Y. Z. Jiab, C. Z. Fanc, *et al.*, "Effect of cooling rate on solidified microstructure and mechanical properties of aluminium-A356 alloy," *journal of Materials Processing Technology*, vol. 207 pp. 107–111, 2008.
- [5] A. T. Abbas, M. Alata, A. E. Ragab, M. M. El Rayes, and E. A. El Danaf, "Prediction Model of Cutting Parameters for Turning High Strength Steel Grade-H: Comparative Study of Regression Model versus ANFIS," *Advances in Materials Science and Engineering*, vol. 2017, pp. 1-12, 2017.
- [6] Y.-C. Cheng, W.-Y. Hsu, K. Abou-El-Hossein, O. Olufayo, and T. Otieno, "Investigation of diamond turning: of rapidly solidified aluminum alloys," in *Current Developments in Lens Design and Optical Engineering*, San Diego, California, United States, 2014.
- [7] L. Katgerman and F. Dom, "Rapidly solidified aluminium alloys by meltspinning," *Materials Science and Engineering: A*, vol. 375-377, pp. 1212-1216, 2004.
- [8] B. H. Kear, "Cutting Edge Technology," ed. Washington DC: The National Academy Press, 1984, pp. 86-108.
- [9] O. K. Abubakre, U. P. Mamaki, and R. A. Muriana, "Investigation of the Quenching Properties of Selected Media on 6061 Aluminum Alloy " *Journal of Minerals & Materials Characterization & Engineering*, vol. 8, pp. 303-315, 2009.
- [10] Y. Odani, Y. Takeda, T. Hayashi, and K. Akechi, "Mechanical Properties of rapidly solidified aluminium alloys," *Metal Powder Report*, vol. 45, 1990.
- [11] G. Jeong, J. Park, S. Nam, S. E. Shin, J. Shin, D. Bae, *et al.*, "The Effect Of Grain Size On The Mechanical Properties Of Aluminum," *Archives of Metallurgy and Materials*, vol. 60, 2015.
- [12] E. O. Hall, "The Deformation and Ageing of Mild Steel. III Discussion of Results," *Proceedings of the Physical Society London*, vol. 64, pp. 747-753, 1951.
- [13] O. Uzuna, T. Karaaslan, M. Gogebakan, and M. Keskin, "Hardness and microstructural characteristics of rapidly solidified Al–8–16 wt.%Si alloys," *Journal of Alloys and Compounds*, vol. 376, pp. 149-157, 2004.
- [14] Chegg. *Alloys*. Available: <https://www.chegg.com/homework-help/definitions/alloys-6>
- [15] M. G. Kalhapure and P. M. Dighe, "Impact of Silicon Content on Mechanical Properties of Aluminum Alloys " *International Journal of Science and Research (IJSR)*, vol. 4, 2015.
- [16] V. Kumar, H. Mehdi, and A. Kumar, "Effect of Silicon content on the Mechanical Properties of Aluminum Alloy," *International Research Journal of Engineering and Technology (IRJET)*, vol. 2, pp. 1326-1330, 2015.
- [17] B. Akyüz, "EFFECT OF SILICON CONTENT ON MACHINABILITY OF Al-Si ALLOYS," *Advances in Science and Technology Research Journal*, vol. 10, pp. 51–57, 2016.
- [18] R. W. Cahn, *Physical Metallurgy*, Third ed.: Elsevier Science Publishers B.V., 1983.

- [19] R. G. Brooks, C. Moore, A. G. Leatham, and J. S. Coombs, "The Osprey Process," *Powder Metallurgy*, vol. 20, pp. 100-102, 1977.
- [20] A. R. E. Singer, "Metal matrix composites made by spray forming," *Materials Science and Engineering: A*, vol. 135, pp. 13-17, 1991.
- [21] R. W. Evans, A. G. Leatham, and R. G. Brooks, "The Osprey Preform Process," *Powder Metallurgy*, vol. 28, 1985.
- [22] W. T. Carter, M. G. Benz, J. K. Browning, R. J. Zabalat, B. A. Knudsen, R. M. F. Jones, *et al.*, "Clean Metal Spray Forming " *The Minerals, Metals & Materials Society*, 1997.
- [23] AZoM. (Aug 23, 2001). *Spray Formed Aerospace Alloys*. Available: <https://www.azom.com/article.aspx?ArticleID=740>
- [24] Z. H. Zhang, X. F. Bian, and Y. Wang. (2003, 3/1/2003) Microstructural characterization of rapidly solidified Al90Ce10 alloy. *Philosophical Magazine*. 827.
- [25] J. Grum and R. Sturm, "Laser surface melt-hardening of gray and nodular irons," *Applied Surface Science*, vol. 109, pp. 128–132, 1997.
- [26] S. Nayak, "Laser Induced Surface Modification of Aluminium Alloys," PhD Dissertation, Tennessee Research and Creative Exchange, University of Tennessee, Knoxville, 2004.
- [27] P. Duwez, R. H. Willens, and W. Klement, "Continuous Series of Metastable Solid Solutions in Silver-Copper Alloys," *Journal of Applied Physics*, vol. 31, 1960.
- [28] A. Ahmad, *Handbook of Optomechanical Engineering*, Second ed.: CRC Press Taylor & Francis Group, 2017.
- [29] X. Dong, L. He, and P. Li, "Gradient microstructure and multiple mechanical properties of AlSi9Cu alloy ribbon produced by melt spinning," *Journal of Alloys and Compounds*, vol. 612, pp. 20–25, 2014.
- [30] T. V. Vorbuger and J. Raja, "Surface Finish Metrology Tutorial," U. S. D. o. Commerce, Ed., ed. Gaithersburg, MD: National Institute of Standards and Technology, 1990.
- [31] H. A. El-Hofy, *Fundamental of Machining Processes*: CRC Press, 2014.
- [32] W. Grzesik, "A Revised Model For Predicting Surface Roughness In Turning," *Elsevier*, pp. 143-148, 1996.
- [33] J. Kaczmarek, "Principles of Machining by Cutting, Abrasion and Erosion," *Peter Peregrinus, Stevenage*, 1976.
- [34] G. P. Petropoulos, C. N. Pandazaras, and P. Davim, "Surface Texture Characterization and Evaluation Related to Machining," Department of Mechanical and Industrial Engineering, University of Thessaly, Pedion Areos, 38334 Volos, Greece.
- [35] S. To, W. B. Lee, and C. Y. Chan, "Ultraprecision Diamond Turning of Aluminum Single Crystals," *Journal of Materials Processing Technology*, vol. 63, pp. 157-162, 1997.
- [36] M. Tauhiduzzaman and S. Veldhuis, "Effect of Material Microstructure and Tool Geometry on Surface Generation in Single Point Diamond Turning," *Precision Engineering*, vol. 38, pp. 481-491, 2014.
- [37] C. F. Cheung, S. To, and W. B. Lee, "Anisotropy of surface roughness in diamond turning of brittle single crystals," *Materials and Manufacturing Processes*, vol. 17, pp. 251-267, 2002.
- [38] M. Kong, "A study of materials swelling and its characterization on nano-surface generation in ultra-precision machining," M.Phil, Department of Industrial and Systems Engineering, The Hong Kong Polytechnic University, Hong Kong, 2007.
- [39] C. F. Cheung and W. B. Lee, "Study of Factors Affecting the Surface Quality in Ultra-Precision Diamond Turning," *Materials and Manufacturing Processes*, vol. 15, pp. 481-502, 2000.
- [40] M. C. Kong, W. B. Lee, C. F. Cheung, and S. To, "A study of materials swelling and recovery in single-point diamond turning of ductile materials," *Material Process Technology*, vol. 180, pp. 210–215, 2006.

- [41] S. To, C. F. Cheung, and W. B. Lee, "Influence of material swelling on surface roughness in diamond turning of single crystals," *Materials Science and Technology*, vol. 17, pp. 102-108, 2001.
- [42] J. Kumar, V. S. N. BE, K. D. Chattopadhyay, R. V. Sarepaka, and R. Sinha, "Thermal Effects in Single Point Diamond Turning: Analysis, modeling and experimental study," *Measurement*, vol. 102, pp. 96-105, 2017.
- [43] F. KAHRAMAN and A. SAGBAS, "AN INVESTIGATION OF THE EFFECT OF HEAT TREATMENT ON SURFACE ROUGHNESS IN MACHINING BY USING STATISTICAL ANALYSIS," *Iranian Journal of Science & Technology, Transaction B: Engineering*, vol. 34, 2010.
- [44] M. P. Kumar, K. Amarnath, and M. SunilKumar, "A Review on Heat Generation in Metal Cutting," *International Journal of Engineering and Management Research*, vol. 5, pp. 193-197, 2015.
- [45] N. Tounsi and A. Otho, "Identification of machine-tool-workpiece system dynamics.," *Interanational Journal of Machine Tools and Manufacturing*, vol. 40, pp. 1367-1384, 2000.
- [46] I. Marinescu, C. Ispas, and D. Boboc, *Handbook of machine tool analysis*. New York: Marcel Dekker, 2002.
- [47] W. A. Kline, R. E. Devor, and I. A. Shareef, "The prediction of surface accuracy in end milling," *Journal of Engineering for Industry*, vol. 104, pp. 272-278, 1982.
- [48] S. C. Eze, C. O. Izelu, B. U. Oreko, and B. A. Edward, "Experimental Study of Induced Vibration and Work Surface Roughness in the Turning of 41Cr4 Alloy Steel using Response Surface Methodology," *International Journal of Innovative Research in Science, Engineering and Technology* vol. 2, pp. 7677-7684, 2013.
- [49] J. Lipski, G. Litak, R. Rusinek, K. Szabelski, A. Teter, J. Warmindski, *et al.*, "Surface Quality of a Work Material Influence on Vibrations in a Cutting Process," *Journal of Sound and Vibration*, 2001.
- [50] X. B. BLOG. (August 12, 2011). *Free and Forced Vibrations in One Degree of Freedom System*. Available: <http://www.xyobalancer.com/xyo-balancer-blog/free-and-forced-vibrations-in-one-degree-of-freedom-system>
- [51] X. Han, H. Ouyang, M. Wang, N. Hassan, and Y. Mao, "Self-excited vibration of workpieces in a turning process," *Journal of Mechanical Engineering Science*, vol. 226, pp. 1958-1970, 2012.
- [52] A. K. M. N. Amin, A. U. Patwari, M. S. Sharulhazrin¹, and I. Hafizuddin¹, "Investigation of Effect of Chatter Amplitude on Surface Roughness during End Milling of Medium Carbon Steel " *Proceedings of the 2010 International Conference on Industrial Engineering and Operations Management 2010*.
- [53] S.-J. Kim, H. U. Lee, and D.-W. Cho, "Prediction of chatter in NC machining based on a dynamic cutting force model for ball end milling," *International Journal of Machine Tools & Manufacture*, vol. 47, pp. 1827-1838, 2007.
- [54] O. Imhade and O. Ugochukwu, "Effects of Cutting Parameters on Surface Roughness during End Milling of Aluminium under Minimum Quantity Lubrication (MQL) " *International Journal of Science and Research (IJSR)*, vol. 4, 2015.
- [55] A. B. Abdullah, L. Y. Chia, and Z. Samad, "The Effect of Feed Rate and Cutting Speed to Surface Roughness," *Asian Journal of Scientific Research*, vol. 3, pp. 278-287, 2010.
- [56] M. A. İNCE and İ. ASİLTÜRK, "Effects of Cutting Tool Parameters on Surface Roughness," *International Refereed Journal of Engineering and Science (IRJES)*, vol. 4, pp. 15-22, 2015.
- [57] Z. Taha, H.-k. Lelana, H. Aoyama, R. A. R. Ghazilla, J. Gonzales, N. Sakundarini, *et al.*, "Insert geometry effects on surface roughness in turning process of AISI D2 steel," *Journal of Zhejiang University-SCIENCE A*, vol. 11, pp. 966-971, 2010.
- [58] H. Gökkaya and M. Nalbant, "The effects of cutting tool geometry and processing parameters on the surface roughness of AISI 1030 steel," *Materials & Design*, vol. 28, pp. 717-721, 2007.
- [59] M. Dogra, V. S. Sharma, and J. Dureja, "Effect of tool geometry variation on finish turning – A Review," *Journal of Engineering Science and Technology*, vol. 4, pp. 1-13, 2011.

- [60] M. Debapriya. *Cutting Tool: Meaning, Types and Angles | Metal Working*. Available: <http://www.yourarticlelibrary.com/metallurgy/cutting-tool-meaning-types-and-angles-metal-working/96029>
- [61] W. P. Koster and M. Field, "Effects of machining variables on the surface and structural integrity of titanium," *Proceedings of the North American Manufacturing Research Conference, SME*, vol. 2, pp. 67–87, 1973.
- [62] V. Vanjari, A. Salve, and S. chinchankar, "Prediction of Effect of Cutting Parameter on Fatigue Life of AISI 52100 Steel " *Materials Today: Proceedings* vol. 5, pp. 922–928, 2018.
- [63] P. S. Maiya and D. E. Busch, "Effect of surface roughness on low-cycle fatigue behaviour of type 304 stainless steel," *Metallurgical Transactions*, vol. 6A, pp. 1761-1774, 1975.
- [64] N. A. Alang, N. A. Razak, and A. K. Miskam, "Effect of Surface Roughness on Fatigue Life of Notched Carbon Steel " *International Journal of Engineering & Technology IJET-IJENS*, vol. 11, 2011.
- [65] V. Kanyanta, S. Ozbayraktar, and K. Maweja, "Effect of manufacturing parameters on polycrystalline diamond compact cutting tool stress-state," *International Journal of Refractory Metals and Hard Materials*, vol. 45, pp. 147-152, 2014.
- [66] T. Nakasuji, S. Kodera, S. Hara, H. Matsunaga, N. Ikawa, and S. Shimada, "Diamond turning of brittle materials for optical components," *CIRP Annals Manufacturing Technology*, vol. 39, pp. 89-92, 1990.
- [67] W. H. Cubberly and R. Bakerjian, *TOOL AND MANUFACTURING ENGINEERS HANDBOOK* Michigan, United States of America: McGraw-Hill Book Co, 1989.
- [68] K. A. Mahajan, M. Sadaiah, and S. H. Gawande, "Experimental investigations of surface roughness on OFHC copper by diamond turning machine.," *International Journal of Engineering Science and Technology*, vol. 2, pp. 5215–5220, 2010.
- [69] G. G. BLOG. (December 3rd, 2012). *Diamond vs. Carbide Tooling Cost Comparison*. Available: www.guhdo.com/blog/diamond-tooling-cost-comparison/
- [70] D. C. Friedrich. (2008). *Diamond as a Tool Material*. Available: <http://pages.mtu.edu/~microweb/index.html>
- [71] T. Materia. (November, 2001). *Classification of Carbon and Low-Alloy Steels*. Available: www.totalmateria.com/articles/Art62.htm
- [72] C. Industries. *High Speed Steels For Cutting Tools*. Available: www.crucible.com/eselector/prodbyapp/highspeed/highspeedappintro.html#Anchor
- [73] (2018). *HIGH SPEED STEEL TOOL DATA*. Available: <http://www.icscuttingtools.com/Tooldata.htm>
- [74] SME. *Cutting Tool Materials* Available: www.sme.org/WorkArea/DownloadAsset.aspx?id=73722
- [75] R. B. d. Silva, á. R. Machado, E. O. Ezugwu, J. Bonney, and W. F. Sales, "Tool life and wear mechanisms in high speed machining of Ti6Al4V alloy with PCD tools under various coolant pressures," *Journal of Materials Processing Technology*, vol. 213, pp. 1459- 1464, 2013.
- [76] J. R. Davis, *ASM Specialty Handbook: Tool Materials*: ASM International, 1995.
- [77] A. M. Abdul-Rani, A. A. B. C. Sidid, and A. H. A. Adzis, "Study on the Effect of Diamond Grain Size on Wear of Polycrystalline Diamond Compact Cutter," *IOP Conference Series: Materials Science and Engineering*, vol. 328, 2018.
- [78] A. G. Beattie, *Acoustic Emission Non-Destructive Testing of Structures using Source Location Techniques*. Albuquerque, New Mexico: Sandia National Laboratories, 2013.
- [79] S. Abhishek, "The Study of Active and Passive Transducers," *INTERNATIONAL JOURNAL OF INNOVATIVE RESEARCH IN ELECTRICAL, ELECTRONICS, INSTRUMENTATION AND CONTROL ENGINEERING*, vol. 3, 2015.

- [80] H. Vallen. (September 2002). *AE Testing Fundamentals, Equipment, Applications*. Available: www.ndt.net/article/v07n09/05/05.htm
- [81] J. Holterman and P. Groen, *An Introduction to Piezoelectric Materials and Applications*. Apeldoorn, The Netherlands: Stichting Applied Piezo, 2013.
- [82] B. P.-O. INC. *PIEZOELECTRIC COMPONENTS*. Available: <https://www.bostonpiezooptics.com/the-ultrasonic-transducer>
- [83] M.-H. Zhao, Z.-L. Wang, and S. X. Mao, "Piezoelectric Characterization of Individual Zinc Oxide Nanobelt Probed by Piezoresponse Force Microscope," *Chemistry of Materials*, vol. 4, pp. 587–590, 2004.
- [84] A. G. Beattie, "Acoustic Emission Couplants I: the ASTM Survey.," *Journal of Acoustic Emission*, vol. 2, 1983.
- [85] A. G. Beattie, J. A. Barron, R. S. Algers, and C. C. Feng., "Acoustic Emission Couplants II: Coupling Efficiencies of Assorted Materials.," *Journal of Acoustic Emission*, vol. 2, 1983.
- [86] Intertechnology. *Kistler Piezotron Coupler Type 5127B*. Available: http://www.loadcells-torque-sensors.com/Kistler/ACC_Model_5127B.htm
- [87] Kistler. (2009). *Piezotron Coupler*. Available: www.kistler.com/?type=669&fid=80436&model=document
- [88] Noliac. *THERMAL PROPERTIES OF PIEZOCERAMIC MATERIAL*. Available: <http://www.noliac.com/tutorials/piezo-basics/thermal-properties-of-piezoceramic-material/>
- [89] *Vibration sensor wiring and cabling*. Available: https://wilcoxon.com/wp-content/uploads/2016/07/TN22_Vibration-Sensor-Wiring-and-Cabling-1.pdf
- [90] J. J. Carr. (1998) ELECTROMAGNETIC INTERFERENCE (EMI). *NUTS & VOLTS MAGAZINE*.
- [91] D. A. Bell, *Handbook of Electronic Engineering*. Chemical Rubber Co. Cleveland OH: L.E.C. Hughes and F.W. Holland, 1967.
- [92] S. O. Gaponenko and A. E. Kondratiev, "Device for Calibration of Piezoelectric Sensors," *International Conference on Industrial Engineering, ICIE*, vol. 206, pp. 146–150, 2017.
- [93] Kistler. (2007). *Acoustic Emission Sensor*. Available: https://intertechnology.com/Kistler/pdfs/Accelerometer_Model_8152B.pdf
- [94] T. E. o. E. Britannica. (December 13, 2017). *International Bureau of Weights and Measures*. Available: <https://www.britannica.com/topic/International-Bureau-of-Weights-and-Measures>
- [95] C. U. Grosse and M. Ohtsu, *Acoustic Emission Testing*. Berlin Heidelberg: Springer-Verlag, 2008.
- [96] N. R. Center. *Theory - Acoustic Waves*.
- [97] B. A. Behrens, S. Hubner, and K. Wolki, "Acoustic emission—A promising and challenging technique for process monitoring in sheet metal forming," *Journal of Manufacturing Processes*, vol. 29, pp. 281-288, 2017.
- [98] K. Iwata and T. Moriwaki, "An application of acoustic emission measurement to in-process sensing of tool wear," *Annals of the CIRP*, vol. 26, pp. 21-26, 1977.
- [99] S. Gholizadeh, Z. Leman, and B. T. H. T. Baharudin, "A review of the application of acoustic emission technique in engineering," *Structural Engineering & Mechanics*, vol. 54, pp. 1075-1095, 2015.
- [100] H. Vallen, "AE Testing Fundamentals, Equipment, Applicationsm NDTnet, 7.," 2002.
- [101] M. R. Kaphle. (2012). *Analysis of acoustic emission data for accurate damage assessment for structural health monitoring applications*. Available: http://eprints.qut.edu.au/53201/1/Manindra_Kaphle_Thesis.pdf.
- [102] S. Bhardwaj, S. Tewari, and S. Jain, "Study on Future of Artificial Intelligence in Neural Network System," *International Journal of Scientific & Engineering Research*, vol. 4, pp. 597-601, 2013.
- [103] tutorialspoint. (2018). *Artificial Intelligence - Overview*. Available: https://www.tutorialspoint.com/artificial_intelligence/artificial_intelligence_overview.htm

- [104] S. Agatonovic-Kustrin and R. Beresford, "Basic concepts of artificial neural network (ANN) modeling and its application in pharmaceutical research," *Journal of Pharmaceutical and Biomedical Analysis*, vol. 22, pp. 717-727, 1999.
- [105] I. Asiltürk and M. Çunkas, "Modeling and prediction of surface roughness in turning operations using artificial neural network and multiple regression method," *Expert Systems with Applications*, vol. 38, pp. 5826–5832, 2011.
- [106] M. Dong and N. Wang, "Adaptive network-based fuzzy inference system with leave-one-out cross-validation approach for prediction of surface roughness," *Applied Mathematical Modelling* vol. 35, pp. 1024–1035, 2011.
- [107] P. Munoz-Escalon and P. G. Maropoulos, "Artificial Neural Networks for Surface Roughness Prediction when Face Milling Al 7075-T7351," *Journal of Materials Engineering and Performance*, vol. 19, pp. 185-193, 2009.
- [108] Y. Jiao, S. Lei, Z. J. Pei, and E. S. Lee, "Fuzzy Adaptive Networks in Machining Process Modeling: Surface Roughness Prediction for Turning Operations," *International Journal of Machine Tools & Manufacture*, vol. 44, pp. 1643–1651, 2004.
- [109] D. P. Pallavi and J. Patel, "A Comprehensive Review On Fuzzy Logic System," *International Journal Of Engineering And Computer Science* vol. 3, pp. 9160-9165, 2014.
- [110] Z. Jin and B. K. Bose, "Evaluation of membership functions for fuzzy logic controlled induction motor drive," vol. 1, pp. 229-234, 2002.
- [111] L. A. Zadeh, "Fuzzy Sets," *Inform Control*, vol. 8, pp. 338–353., 1965.
- [112] L. A. Zadeh, "Is there a need for fuzzy logic?," *Journal of Information Sciences*, vol. 178, pp. 2751-2779, 2008.
- [113] H. Jalalifar, S. Mojedifar, and A. A. Sahebi, "Prediction of rock mass rating using fuzzy logic and multi-variable RMR regression model," *International Journal of Mining science and Technology*, vol. 24, pp. 237-244, 2014.
- [114] N. Peric, "Fuzzy logic and fuzzy set theory based edge detection algorithm," *Serbian Journal of Electrical Engineering*, vol. 12, pp. 109-116, 2015.
- [115] C. Venugopal, S. P. Devi, and K. S. Rao, "Predicting ERP User Satisfaction—an Adaptive Neuro Fuzzy Inference System (ANFIS) Approach," *Intelligent Information Management*, vol. 2, 2010.
- [116] T. J. Ross, *Fuzzy logic with Engineering Applications*, Third ed.: John Wiley & Sons, Ltd, 2011.
- [117] R. Saneifard, "Some properties of neural networks in designing fuzzy systems," *Neural Computing and Applications*, vol. 21, pp. 215-220, 2011.
- [118] S. S. Ahmad and S. P. Simonovic, "A METHODOLOGY FOR SPATIAL FUZZY RELIABILITY ANALYSIS," *Applied GIS*, vol. 3, pp. 1-42 2007.
- [119] J. M. Mendel, "Fuzzy logic Systems for Engineering: A Tutorial," *Proceedings of the Institution of Electrical and Electronic Engineers*, vol. 84, 1995.
- [120] T. A. Runkler, "Selection of Appropriate Defuzzification Methods Using Application Specific Properties," *IEEE TRANSACTIONS ON FUZZY SYSTEMS*, vol. 5, 1997.
- [121] D. Z. SALETIC, D. M. VELASEVIC, and N. E. MASTORAKIS. (2002, Analysis of Basic Defuzzification Techniques. Available: <https://www.researchgate.net/publication/264874571>
- [122] A. Kaur and A. Kaur, "Comparison of Mamdani-Type and Sugeno-Type Fuzzy Inference Systems for Air Conditioning System," *International Journal of Soft Computing and Engineering (IJSCE)*, vol. 2, pp. 323-325, 2012.
- [123] A. Hamam and N. D. Georganas, " A comparison of Mamdani and Sugeno fuzzy inference systems forevaluating the quality of experience of haptic-audiovisualapplications.," *IEEE International Workshop on Haptic Audio Visual Environments and their Applications*, pp. 18-19, 2008.
- [124] X. He and S. Xu, *Artificial Neural Networks*. Berlin: Springer, 2009.
- [125] M. A. Arbib, *Brains, Machines, and Mathematics*, Second ed. New York: Springer-Verlag, 1987.

- [126] C. L. Koo, M. J. Liew, M. S. Mohamad, and A. H. Salleh, "A review for detecting gene-gene interactions using machine learning methods in genetic epidemiology," *Biomed Res Int*, vol. 2013, p. 432375, 2013.
- [127] M. H. Sazli, "A brief review of feed-forward neural networks," *Communications, Faculty Of Science, University of Ankara*, pp. 11-17, 2006.
- [128] J. K. Basu, D. Bhattacharyya, and T.-h. Kim, "Use of Artificial Neural Network in Pattern Recognition " *International Journal of Software Engineering and I International Journal of Software Engineering and Its Applications ts Applications*, vol. 4, 2010.
- [129] J. M. Zurada, *Introduction to Artificial Neural Systems* New York: West Publishing Company, 1990.
- [130] M. Technosoft. (May 21, 2018). *Artificial Neural Networks*. Available: <https://msatechnosoft.in/blog/tech-blogs/artificial-neural-network-types-feed-forward-feedback-structure-perceptron-machine-learning-applications>
- [131] D. O. Hebb, *The Organization of Behaviour*. New York: Wiley, 1949.
- [132] F. Roseblatt, *Principles of Neurodynamics*. New York: Spartan Books, 1959.
- [133] J. L. McClelland and D. E. Rumelhart, *Parallel Distributed Processing: Explorations in the Microstructure of Cognition* vol. 1. Cambridge: MIT Press, 1988.
- [134] J. S. R. Jang, "ANFIS: adaptive network-based fuzzy inference systems," *IEEE Trans Sys Man Cybern*, vol. 23, pp. 665-685, 1993.
- [135] E. Czogala and J. Leski, *Fuzzy and Neuro-Fuzzy Intelligent Systems*. New York, 2000.
- [136] S. J. Hossain, "NEUROFUZZY BASED SURFACE ROUGHNESS MODELLING FOR BALL END MILLING OPERATION," MASTER OF SCIENCE IN INDUSTRIAL & PRODUCTION ENGINEERING, DEPARTMENT OF INDUSTRIAL & PRODUCTION ENGINEERING, BANGLADESH UNIVERSITY OF ENGINEERING & TECHNOLOGY, Dhaka, 2012.
- [137] E. Power, "Adaptive Neuro Fuzzy Inference System (ANFIS) For Fault Classification in the Transmission Lines," *Online Journal on Electronics and Electrical Engineering*, pp. 164-169, nd.
- [138] S. Roy, "Design of adaptive neuro-fuzzy inference system for predicting surface roughness in turning operation," *Journal of Scientific & Industrial Research*, vol. 64, pp. 653-659, 2005.
- [139] G. Onwuka, K. Abou-El-Hosseini, and Z. Mkoko, "International Conference on Recent Trends in Physics 2016 (ICRTP2016)," *Journal of Physics: Conference Series*, vol. 755, p. 011001, 2016.

APPENDIX A: KISTLER 8152B DATA

Table A- 1: Kistler 8152B Data

Technical Data					
Type	Unit	8152B111/121	8152B11/12sp	8152B211/221	8152B21/22sp
Sensitivity	dBref 1V/(m/s)	57	57	48	48
Frequency Range ± 10 dB	kHz	50 ... 400	50 ... 400	100 ... 900	100 ... 900
Ground Isolation	M Ω	>1	>1	>1	>1
Environmental:					
Shock Limit (0.5ms pulse)	gpk	2000	2000	2000	2000
Temperature Range Operating	$^{\circ}$ F	-40 ... 140	-40 ... 140	-40 ... 140	-40 ... 140
Output:					
Bias nom.	VDC	2.2	2.2	2.5	2.5
Impedance	Ω	<10	<10	<10	<10
Voltage full scale	V	± 2	± 2	± 2	± 2
Current	mA	2	2	4	4
Source:					
Voltage (Coupler)	VDC	5 ... 36	5 ... 36	5 ... 36	5 ... 36
Constant Current	mA	3 ... 6	3 ... 6	3 ... 6	3 ... 6
Construction:					
Sensing Element	type	ceramic	ceramic	ceramic	ceramic
Housing/Base	material	stainless steel	stainless steel	stainless steel	stainless steel
Sealing-housing/connector	type	hermetic	hermetic	hermetic	hermetic
Viton Cable Bend Radius, max.	in	0.6	0.6	0.6	0.6
Weight (without cable)	grams	29	29	29	29
Mounting Torque	lbf-in	80 \pm 10	80 \pm 10	80 \pm 10	80 \pm 10

1 g = 9.80665 m/s², 1 inch = 25.4 mm, 1 gram = 0.03527 oz, 1 lbf-in = 0.1129 Nm

APPENDIX B: ASM HANDBOOK, VOLUME 16: MACHINING, p761-804

Table B- 1: Machining Parameters

Operation	Tool	Speed, m/min (sfm)	Feed	Depth, mm (in.)	Coolant
Turning	Tungsten carbide, with J polish (SPG 422 insert)	30-150 (100-500)	0.13-0.51 mm/rev (0.005-0.02 in./rev)	0.13-5.1 (0.005-0.20)	Soluble oil (20:1)
	Diamond (SPG 422 insert)	310-910 (1000-3000)	0.08-0.38 mm/rev (0.003-0.015 in./rev)	0.13-3.8 (0.005-0.15)	Soluble oil (20:1)
Milling	Tungsten carbide, C-2 or C-3, 5-10° rake, 7-15° shear	99-175 (325-575)	0.10-0.30 mm/tooth (0.004-0.012 in./tooth)	0.13-5.1 (0.005-0.20)	Soluble oil (15:1) or dry
	Diamond, 5-10° rake, 7-15° shear	400-790 (1300-2600)	0.10-0.20 mm/tooth (0.004-0.008 in./tooth)	0.20-1.0 (0.008-0.040)	Soluble oil (15:1) or dry
Drilling	High-speed steel, high helix	20 (70)	381 mm/min (15 in./min)	6 × diam	Soluble oil (20:1), 19 L/min (5 gal./min) at 170 kPa (25 psi)
	Tungsten carbide tipped, coolant fed	90 (300)	508 mm/min (20 in./min)	6 × diam	Soluble oil (20:1), 34 L/min (9 gal./min) at 3.4 MPa (500 psi)
Tapping	Form taps, with four lobes	20 (70)	By pitch	6 × diam	Soluble oil (20:1), 19 L/min (5 gal./min) at 170 kPa (25 psi)
Broaching	Tungsten carbide, 0° shear, 5° rake	45 (150)	229 mm/min (9 in./min)	0.13 (0.005)	Soluble oil (20:1) or dry

Source: Ref 2

APPENDIX C: PEAK RATE ALGORITHM

```
% Program to determine PPM of signal

% Count the dominant peaks in the signal
% Peaks are defined as point greater than their neighbours and greater than
% 1.
Peak_count=0;
for k=2 : length (VarName1)-1
    if (VarName1(k) > VarName1(k-1) & VarName1(k) > VarName1(k+1) & VarName1(k)>1)
        %disp('I have found a peak');
        % k
        Peak_count=Peak_count+1;
    end
end

% Divide the peaks counted by signal duration (minutes).
fs=100;
N=length(VarName1);
duration_in_seconds=N/fs;
duration_in_minutes=duration_in_seconds/60;
PPM=Peak_count/duration_in_minutes;
```

Figure C- 1: MATLAB Algorithm for Peak Rate Determination

APPENDIX D: INPUTS MEMBERSHIP FUNCTIONS

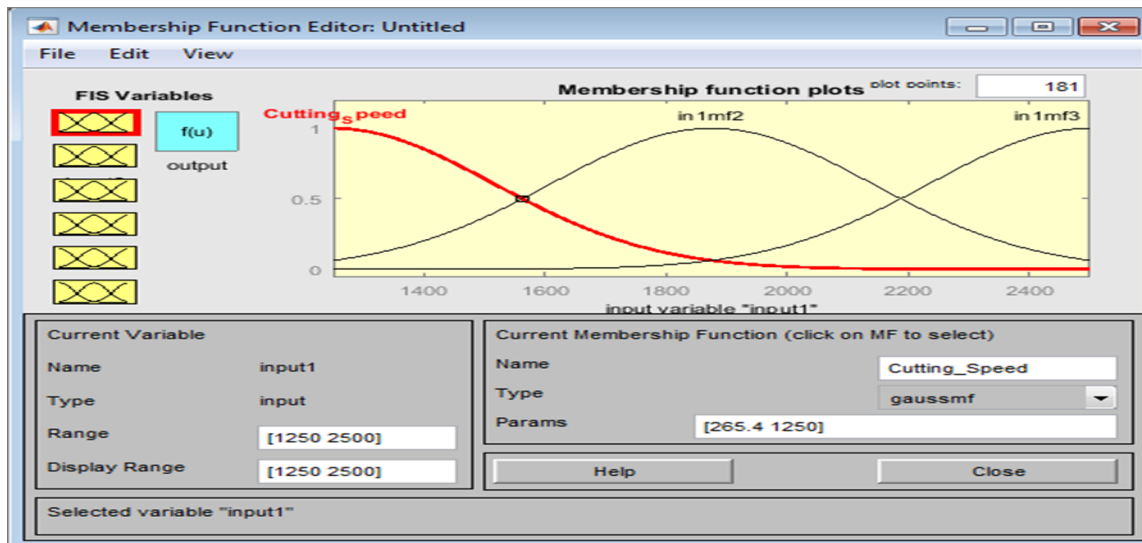


Figure D- 1: Initial membership function plot for the input variable ‘cutting speed’

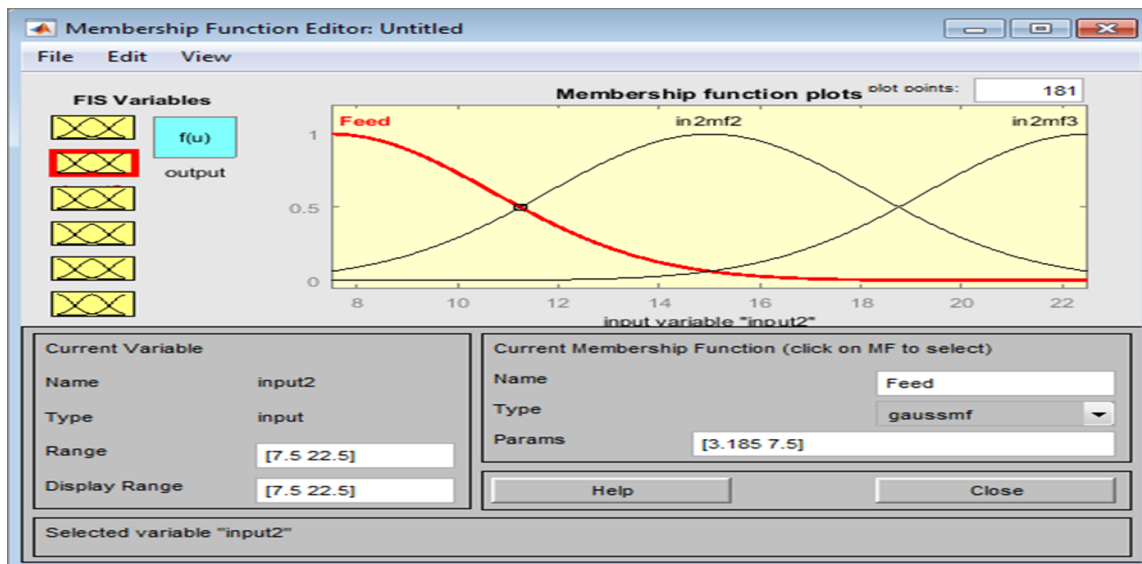


Figure D- 2: Initial membership function plot for the input variable ‘Feed’

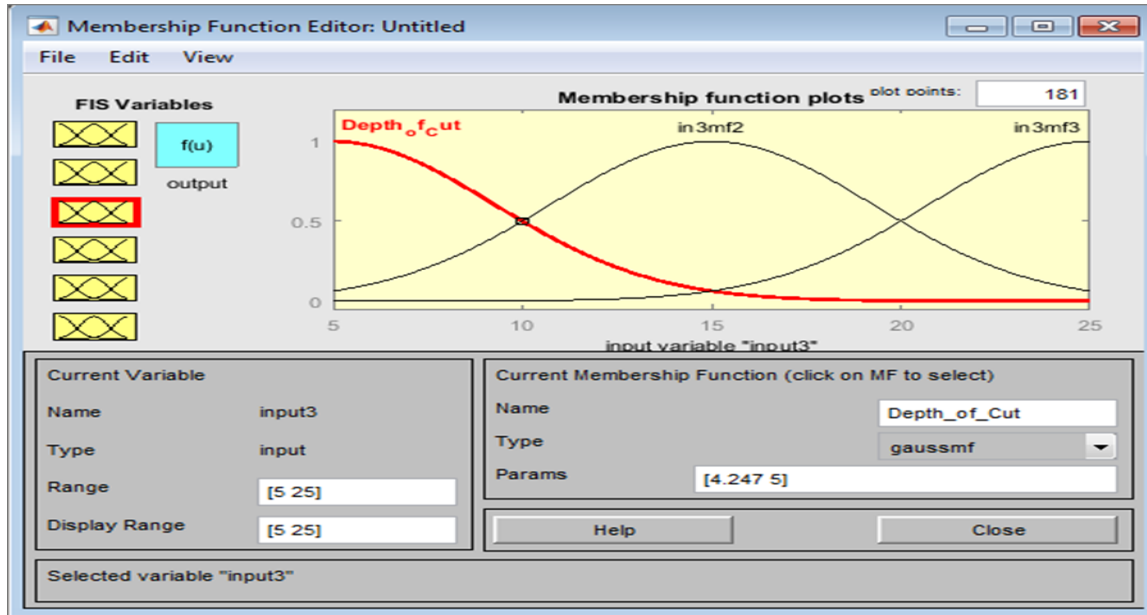


Figure D- 3: Initial membership function plot for the input variable ‘Depth of Cut’

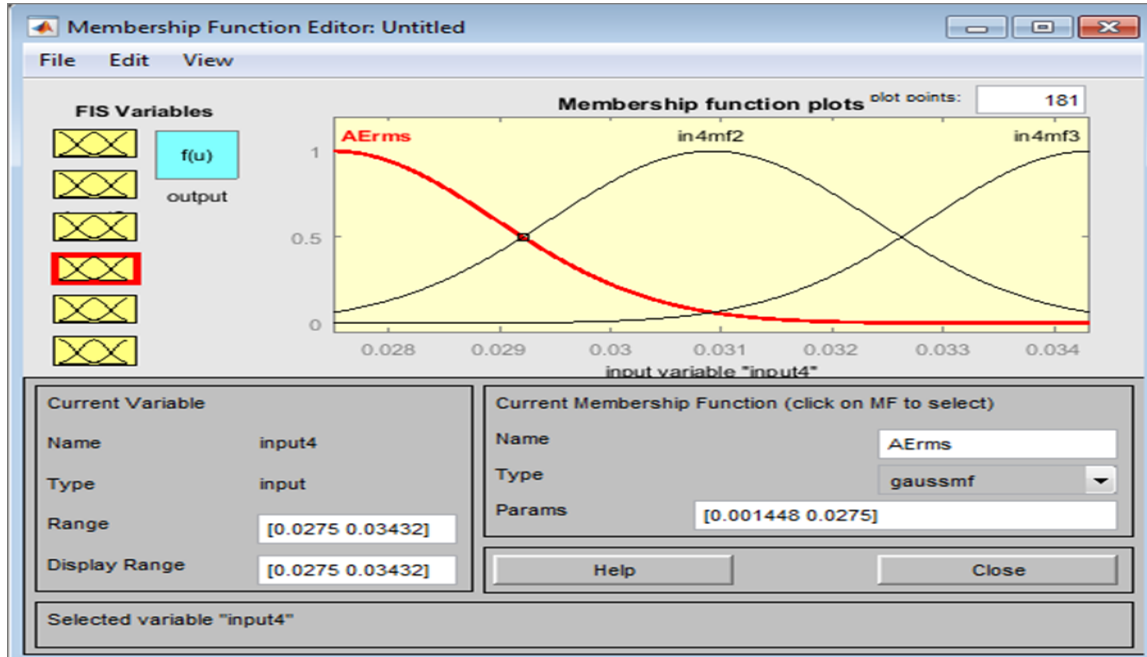


Figure D- 4: Initial membership function plot for the input variable ‘AE_{rms}’

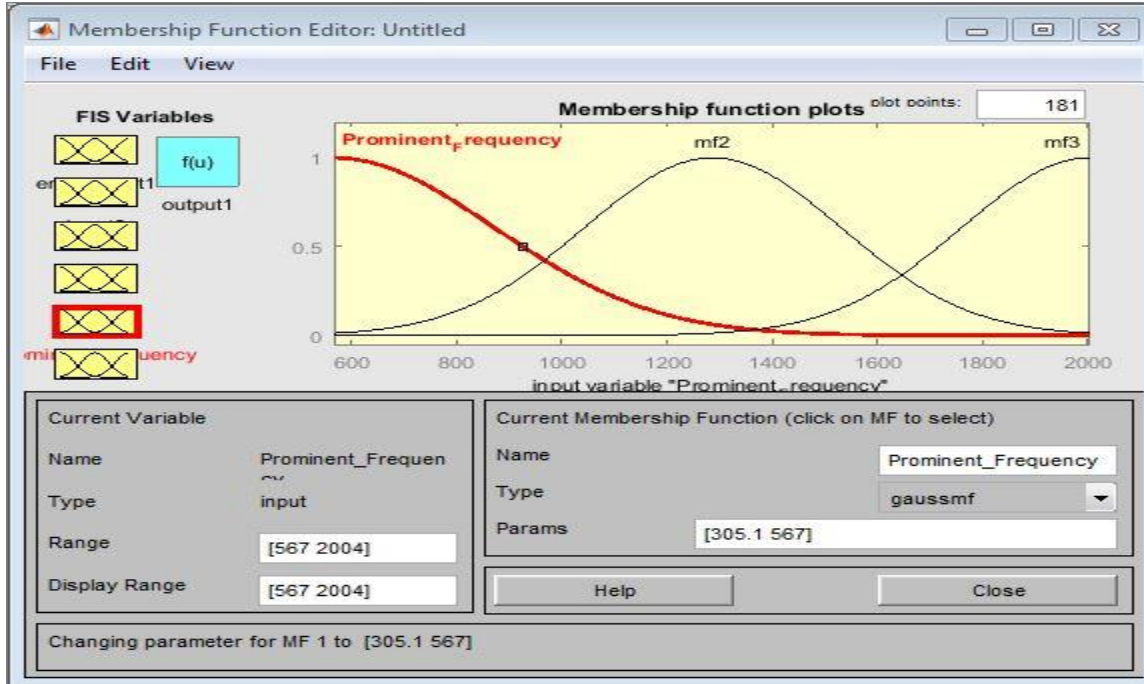


Figure D- 5: Initial membership function plot for the input variable ‘Prominent Frequency’

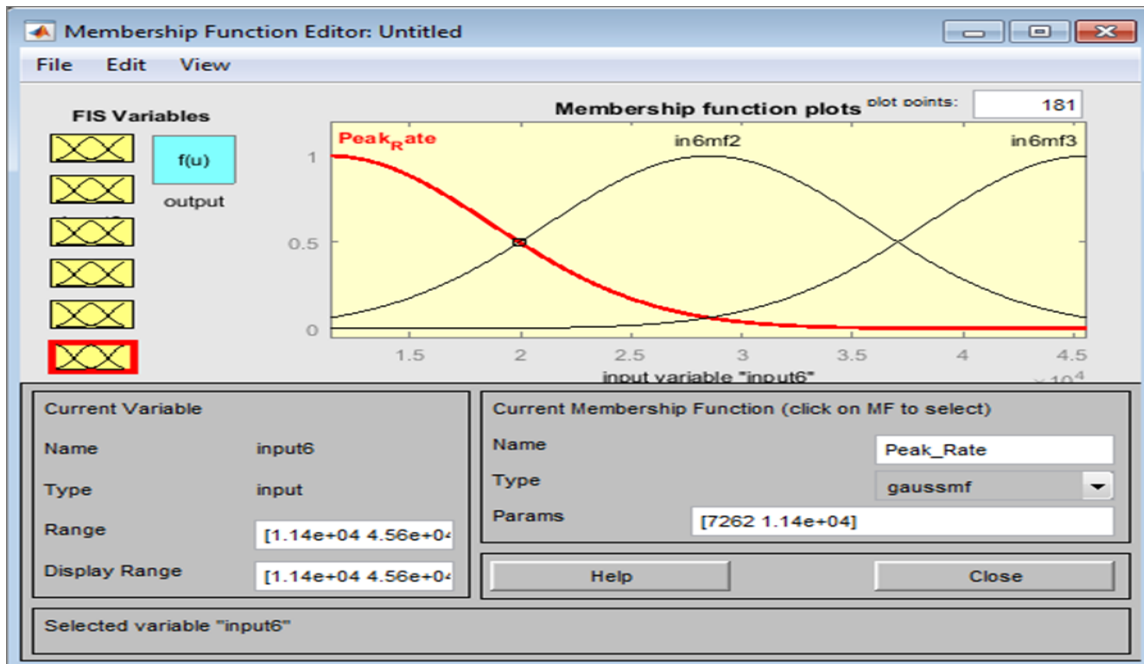


Figure D- 6: Initial membership function plot for the input variable ‘Peak Rate’

APPENDIX E: TURNITIN | EPHORUS RESULTS FOR THESIS

Turnitin | Ephorus: Results for Thesis zviko.pdf - (1%) Σ Inbox x

Turnitin Ephorus Services <noreply@turnitin.com>

to me ▾

Dear Mlambo Powell,

Turnitin | Ephorus checked the document Thesis zviko.pdf.

Document: Thesis zviko.pdf

Result: 1%

You will find the reports attached. You can also login into Turnitin | Ephorus for an [extended report](#).

Notification settings ([change settings](#))

You do receive an e-mail when a student hands in a document

You do not receive an e-mail when Turnitin | Ephorus detected similarities in the text.

You do not receive an overview of all new reports per period

This e-mail has been generated automatically.

If you have any questions, please contact our support department via ephorussupport@turnitin.com.